University of Stavanger

Faculty of Science and Technology

MASTER'S THESIS

Study program/Specialization: Petroleum Geosciences Engineering	2018, Spring Semester Open
Writer: Tayyaba Kausar	(Writer's signature)
Faculty supervisor: Wiktor Waldemar Weibull External supervisor(s): Lothar Schulte (Schlumberger)	
Title of thesis: Simultaneous AVO inversion and seismic lithology cube estimation by using PP and PS angle stack seismic data of the Oseberg Field, North Sea	
Credits (ECTS): 30	
Keywords: Oseberg Field Oseberg Fault Block Zoeppritz' equation and approximations 2D forward modelling AVO inversion PDFs and Seismic lithology cube Reservoir mapping	Pages: 113 +enclosure: <enclosures> Stavanger, 15th June 2018

Simultaneous AVO inversion and seismic lithology cube estimation by using PP and PS angle stack seismic data of the Oseberg Field, North Sea

by

Tayyaba Kausar

Msc Thesis

Presented to the Faculty of Science and Technology

The University of Stavanger

The University of Stavanger

June 2018

Dedication

To my parents and siblings for their continuous support, love and prayers throughout the project.

Acknowledgements

This thesis submission is the part of the requirements for the Master of Science degree in Petroleum Geosciences Engineering. The work has been carried out at University of Stavanger, Norway.

The author would like to acknowledge the Schlumberger for the use of their software PETREL. The author is grateful to Lothar Schulte and Surender Manral for their assistance and mentorship. Many thanks to Statoil for generously allowing to use their data for research. A lot of thanks to Wiktor Waldemar Weibull for supervising the project on behalf of the university of the Stavanger.

Abstract

Simultaneous AVO inversion and seismic lithology cube estimation by using PP and PS angle stack seismic data of the Oseberg Field, North Sea

Tayyaba Kausar, The University of Stavanger, 2018

Supervisors: Wiktor Waldemar Weibull, Lothar Schulte

Converted seismic wave data is not yet commonly used in oil industry. In an offshore environment Ocean Bottom Cables (OBCs) are needed to register the converted S-waves in addition to the P-waves which makes the acquisition of converted seismic waves very expensive. Nevertheless, converted seismic waves may provide additional information to the P-wave seismic which may justify the extra costs in acquisition, processing and interpretation.

This thesis focuses on the joint PP & PS AVO inversion on the Oseberg Field, North Sea. A 2D seismic model is created to analyze the behavior and reliability of AVO inversion by using different sets of P and S angle stack data, different wavelets and multiple algorithms. Based on this result a joint PP & PS AVO inversion is applied to the Oseberg Field data. The result (P-, S- impedance and density) is critically compared with the well log data. In addition, synthetic seismic sections are derived from the inversion results and compared with the angle stacks.

The next step consists of analyzing the well logs in order to find log sets including rock moduli derived from the well logs to discriminate between the different lithological units. This leads to differentiate between hydrocarbon sand, carbonate and shale. Based on these results the seismic inversion attributes are converted to a seismic

lithology cube limited by the top and the base of the reservoir. That cube allows to map the hydrocarbon sand of the reservoir.

Table of Contents

List of Tables

List of Figures

1. INTRODUCTION

The North Sea is a mature hydrocarbon basin and belongs to one of the most prolific hydrocarbon provinces in the world. The search for accumulation of oil and gas in the central and northern North Sea is continuing and large accumulations are still being found in recently licensed areas. The probability of finding new substantial oil and gas reserves is still high, however the used techniques are getting more refined as the unexplored structure area size is becoming smaller, while their complexity is increasing (Cooper & Barnard, 1984).

There are several cases in petroleum industry where compressional waves alone from a standard survey do not adequately image a reservoir or describe its properties. A typical example is accumulated gas in the overburden which can disrupt the transmission of P-waves and obscure underlying targets from imaging based on compressional seismic. However, the combination of shear and compressional waves has the potential to reveal more about the subsurface compared to P-wave surveys alone because the S-wave is not sensitive to the pore content. Also, by using the knowledge of P- and S-wave impedance of a formation that can be derived from AVO inversion, one can predict the lithology more readily rather than using P-wave impedance alone. It is well-known that AVO inversion of P-angle stacks delivers both, P- and S-impedance. However, it will be shown in this thesis that AVO inversion of S-wave data delivers a more reliable S-impedance compared to P-seismic AVO inversion. Multicomponent receivers are needed to record the reflected energy of converted waves. This task is already known to be a challenge on land. As S-waves cannot propagate through water, it is an expensive challenge to register them at sea bottom (Caldwell et al., 1999). In fact, this is a major reason that recording of shear waves in the North Sea is narrow.

Already decades ago, academic institutions have initiated seafloor recording with ocean-bottom seismometer for earthquake and other analysis. Later, Western-Geco developed a four-component device to record converted waves which was first used commercially in 1996. These four multicomponent receivers are very reliable in today's marine seismic surveys. This new technique system is known as ocean bottom cables (OBCs) (Barkved et al., 2004).

In 1996 the Nessie 4C seafloor cable system was used for the first time to acquire 2D surveys in the North Sea for imaging reservoirs covered by overlying gas. The combined use of P- and S-waves has improved the development of the Lomond Field operated by BP in the UK sector of North Sea. Similarly, converted waves seismic data enhanced the reservoir properties of Alba Field, operated by ChevronTexaco in the UK sector of North Sea (Barkved et al., 2004; Caldwell et al., 1999). The OBC technique was also used for the Oseberg Field, Norwegian North Sea, to acquire converted wave data in addition to the P-wave seismic. The data from Oseberg Sør Block 30/9-J, is used in this project to find out the diversity and uniqueness of shear waves in inversion and how does it contribute to the estimation of the reservoir properties.

1.1 OBJECTIVES

The opportunities created by the acquisition of the converted waves in exploration seismology as discussed earlier are the motivation and reason behind this thesis. In this project both compressional and shear wave data is used to investigate the reservoir properties of the study area. The foremost goal of this project is to map the reservoir zone of the Oseberg Sør Field, by using both compressional and shear wave seismic data from Block 30/9 J. This main goal includes the following objectives.

1) The first objective is to investigate the reliability of different inversion algorithms to deliver the best P-, S-impedance and density cube. For this,

conventional (Post-stack, PP AVO inversion) and unconventional (PP & PS AVO joint inversion) inversions will be studied using synthetic data.

2) The most reliable inversion algorithm achieved from synthetic data study, will be applied to the Oseberg Field data. This ultimately will deliver best P-, S-impedance and density cube.
3) The third objective is to predict the seismic lithology cube by using inversion attributes and facies logs.
4) The final objective is to map the reservoir zone of the study area. The lithology cube will be the basis for this mapping.

1.2 DESCRIPTION OF THE STUDY AREA

The Oseberg hydrocarbon field area is located on the eastern flank of the Viking Graben about 61-62° N, in the northern part of the North Sea. To the east, it is bounded by the Horda Platform and the Øygarden Fault Complex (ØFC) (Figure 4). It is located about 140 km NW of the city of Bergen at the southwestern coast of Norway (Figure 1) (Farvardini, 2017; Johnsen, Rutledal, & Nilsen, 1995).

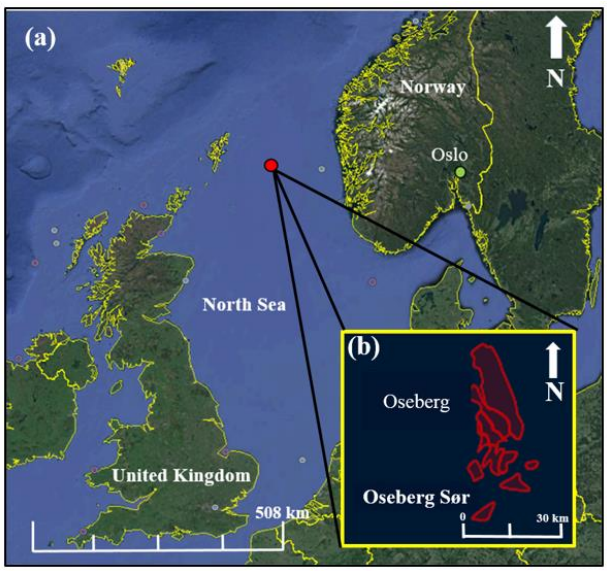

Figure 1: (a) Location of Oseberg Field. (b) Close up image of the Oseberg field. Modified from Google Earth.

The field is about 26 km long and 6 km wide, and the water depth is about 105m. (Johnsen et al., 1995). On the Norwegian Continental Shelf, this field mostly covers blocks 30/6 and 30/9 and part of the blocks 30/5, 30/8 and 30/12. According to literature and NPD map views, the Oseberg Field is subdivided into three fields; Oseberg Main, Oseberg Sør and Oseberg Øst (Figure 2 & 3) (Farvardini, 2017). The research area for this project is Oseberg Sør. The reservoir rocks of this field typically belong to the Brent Group, which deposited from Early to Mid-Jurassic. The thickness of the Brent Group varies from 45 to 190m. (Johnsen et al., 1995).

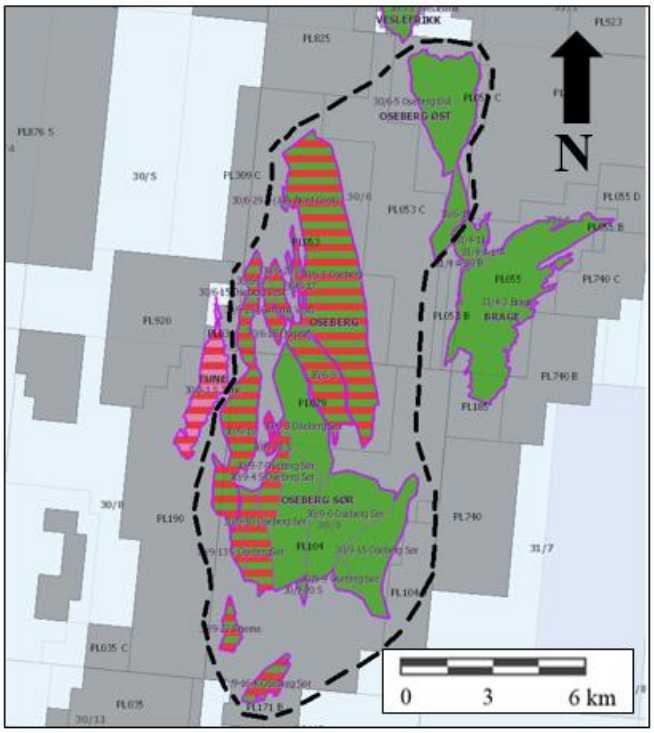

Figure 2: Outline of the Oseberg field. The black dotted line separates the Oseberg field from neighboring fields. Green: oil; red: gas. Modified from Directorate (2018)Norwegian Petroleum Directory.

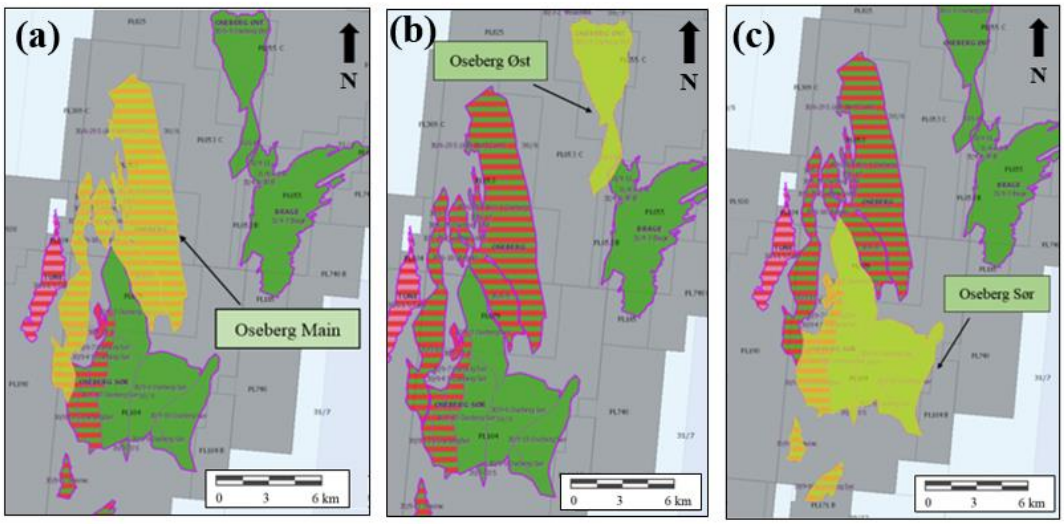

Figure 3: Subdivision of the Oseberg Field, (a) Oseberg Main, (b) Oseberg Sør, (c) Oseberg Øst. Modified after (Directorate, 2018; Industry, 2018), Norwegian Petroleum Directorate.

2. REGIONAL GEOLOGY

2.1 TECTONIC EVOLUTION/ STRUCTURAL OUTLINES

2.1.1. The North Sea

The North Sea as a part of north-west European continental shelf, has a long and complex geological history. The northern North Sea sedimentary basin is bounded by faults, north trending zone of extended crust and it is restricted by mainland of the western Norway to the east and the Shetland Platform to the west (Figure 4). It is about 170 to 200km wide. Older structural elements (i.e. Variscan Orogeny) and Upper Jurassic/ Lower Cretaceous rifting systems both control the elementary tectonic framework of the North Sea. (R.B Faerseth, 1996; R. B. Faerseth & Ravnås, 1998; Glennie, 2009; Halland et al., 2011).

Variscan orogeny took place after, both Precambrian and Caledonian Orogeny. Variscan Orogeny was the result of the collision between Gondwana and Laurasia in Late Visean of the Early Carboniferous times. Regionally during Late Carboniferous times, the central and southern parts of the North Sea were forming a foreland basinal setting. This basinal setting was in front of the northward moving Variscan fold and the thrust belt system. According to Glennie and Underhill (1998), the North Sea basin development related to post-Variscan times can be divide into six major events, namely:

1) Permo-Triassic post-orogenic rifting
2) Late Triassic-Jurassic opening of the western Tethys
3) Middle Jurassic salt doming of the North Sea
4) Development of the triple junction North Sea rift system
5) Creation of the Atlantic Ocean
6) Cretaceous-Early Tertiary closure of the Tethys Ocean and creation of the Alpine fold chain. (Farvardini, 2017; Glennie, 2009; Roberts, Price, & Olsen, 1990).

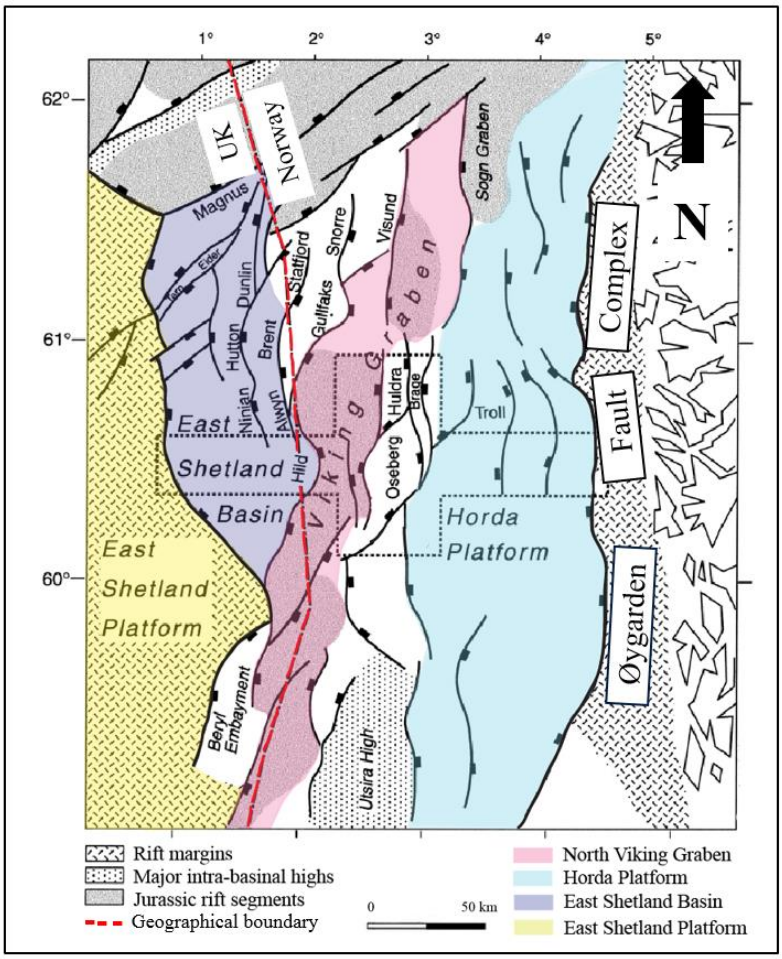

Figure 4: Main structural elements of the northern North Sea, Viking Graben and its surroundings. The Oseberg Area (dotted black lines) is on the eastern side of the Horda Platform and in the central Viking graben. Modified after R. B. Faerseth and Ravnås (1998).

2.1.2. Structural evolution of the Oseberg Fault Block along Oseberg Area

The Oseberg Fault-Block is located on the eastern flank of the Viking Graben (Figure 4 & 5). It is about 16km wide in its center at present day, and it narrows to the south and north. It is tilting towards east and consists of a series of smaller fault blocks. The Oseberg Fault Block represents a structural/topographic high at pre-Tertiary levels. Today this high is bounded by the Brage and the Oseberg faults of Jurassic origin (Figure 5) (R. B. Faerseth & Ravnås, 1998; Ter Voorde, Ravnås, Faerseth, & Cloetingh, 1997).

In the Oseberg area, Permo-Triassic and Jurassic extensional episodes resulted in different configurations. It effects on both, regarding position and dip of block-bounding faults, as well as the direction of tilt of fault blocks and associated half-grabens. Triassic to Jurassic sedimentation in the Oseberg area was associated with variable structural configuration (Figure 5) (R. B. Faerseth & Ravnås, 1998; Knudsen, Liljedahl, Midbøe, & Søderstrøm, 1997):

- During the Permo-Triassic extension, the area was bounded to east by the Brage east fault and signified the mid-part of a wider and westerly tilted fault block. (Figure 5 & 6).
- The Late Triassic to Early Jurassic period is characterized by an overall gradual expansion of the Statfjord and the Dunlin Group to the west which represents a flexure or monoclinal area (Figure 7a & b).
- In the Bajocian (Mid Jurassic), the Brage Fault separated the Oseberg Fault from the Horda Platform. A terrace was created by the Oseberg Fault-Block, which was defined by the Oseberg and Brage faults (Figure 7c&d).
- During the Early Bathonian (Mid Jurassic), a wider Oseberg mega fault was created (Oseberg area). It happened when the eastern boundary of the early Viking Graben, migrated to a fault zone towards west, from the Oseberg Fault zone. (Figure 7e). Consequently, the new, Middle-Late Jurassic Viking Graben became narrower than its former basin.
- During the Kimmeridgian (Late Jurassic), the N-S trending part of the Brage fault became less active, and the Oseberg area was now the western part of the wider Horda Platform (Figure 7f)

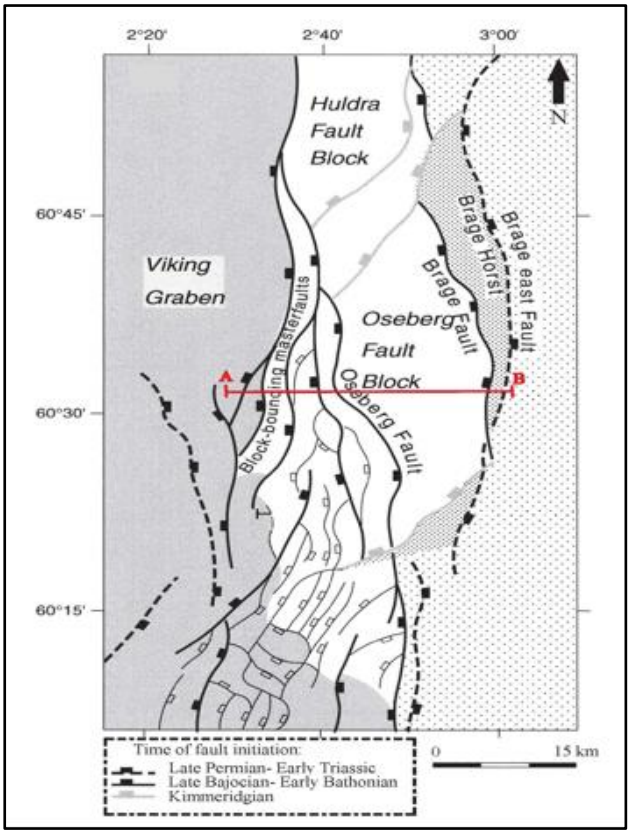

Figure 5: Structures along the eastern flank of the central Viking Graben, structural high is bounded by the Oseberg and the Brage faults. Time of initiation of major faults are indicated. The red cross section line is explained in figure 6. Modified after R. B. Faerseth and Ravnås (1998).

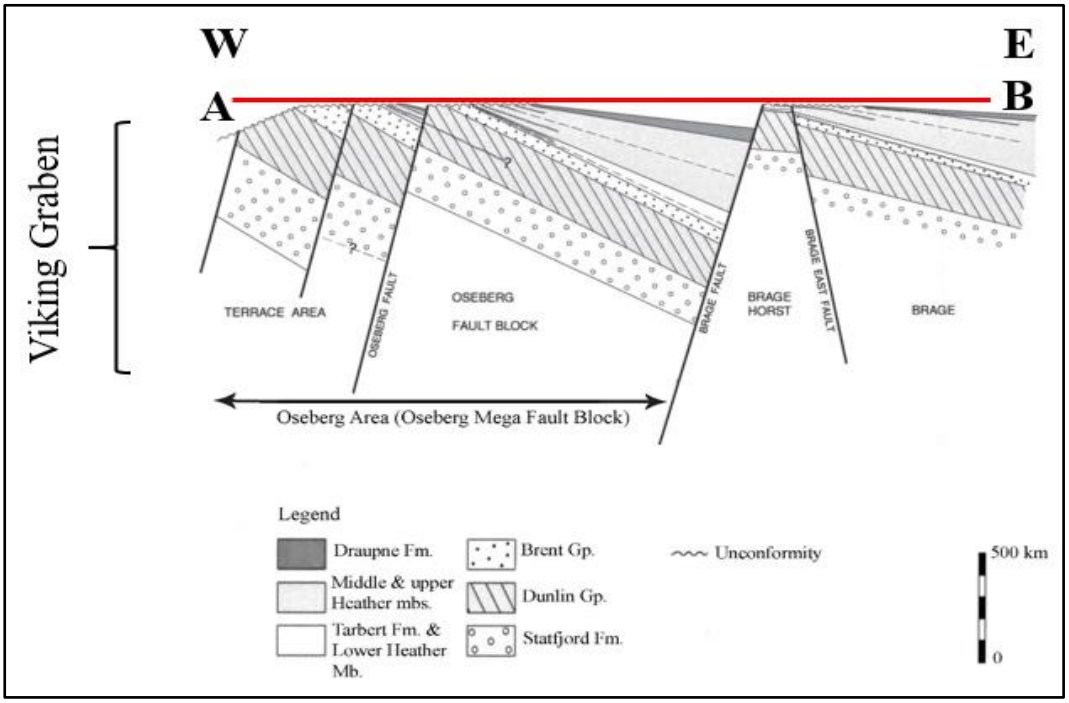

Figure 6: Cross section along E-W central Viking Graben, showing Early to Late Jurassic strata on the Oseberg Fault Block in Norwegian Block 30/6, Just above the study area Block 30/9. Modified after R. B. Faerseth and Ravnås (1998).

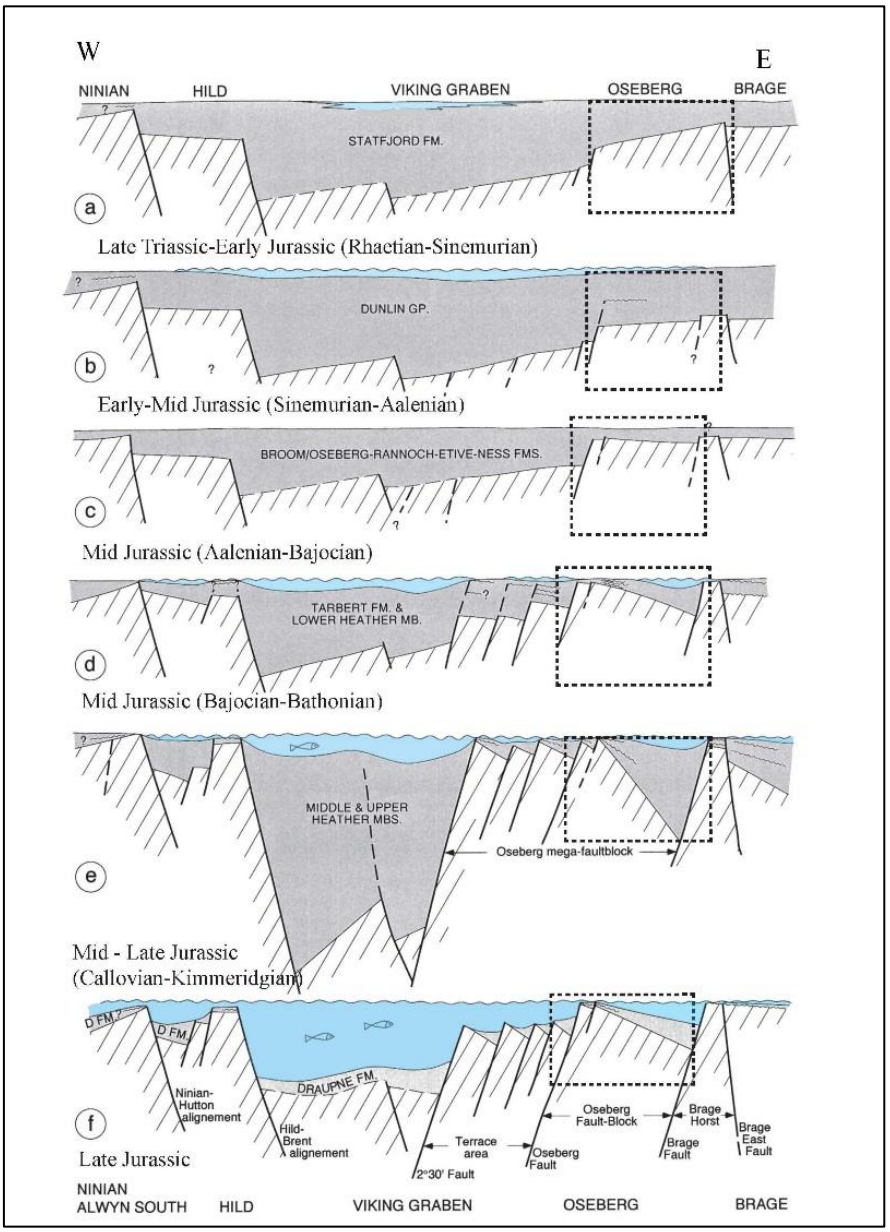

Figure 7: Schematic E-W cross section along the central Viking Graben, showing the evolution of the Oseberg Fault Block along with the Oseberg Area (dotted black box). It also shows the adjacent terraces and fault blocks to the Oseberg Fault Block from Late Triassic to Jurassic. Modified after R. B. Faerseth and Ravnås (1998)

2.2. STRATIGRAPHIC SIGNATURE AND DEPOSITIONAL ENVIRONMENT

The Oseberg Field comprises of deltaic sediments from Late Toarcian to Middle Bathonian age (Lower to Mid Jurassic) which undergo influence of global sea level fluctuation (Figure 8) (Graue et al., 1987). The reservoir rocks belong to the Brent Group, which comprises of five lithostratigraphic units. From top to bottom these units are; Tarbert, Ness, Etive and Rannoch formations which represent the advance and retreat of the Brent delta and Oseberg Formation which represents the localized fan delta prograding from east to west. (Johnsen et al., 1995)

The Draupne Formation is regarded as main source rock. The formation surrounds the Oseberg Field in a large access of volume. It has the high potential of producing hydrocarbon at various levels of maturity (Spencer et al., 1987).

The thickness of most common reservoir, the Brent Group is controlled by tectonic structures. Towards the down- flank the thickness is controlled by easterly tilting fault bocks. These fault blocks are called Alpha, Alpha North and Gamma. (Spencer et al., 1987)

Oseberg Formation: The Oseberg formation consists of moderate to poorly sorted, coarse grained, occasionally layered sandstone above the Dunlin shales. The Oseberg Formation deposition took place in a series of discrete lobes, probably triggered by the tectonic movements along the basin margin and corresponds to the eastern upland. Within the Oseberg Field, at least two of such lobes can be seen, partly overlapping each other, reflecting early progradation from east to west (Johnsen et al., 1995).

Rannoch and Etive formations: The deposition of the Oseberg Formation ceased during the transgression of late Aalenian to early Bajocian. This transgression series created a shallow sea that provided a space for northward progradation of delta front-shoreline deposits of the Brent delta. These early Brent delta sediments comprise the Rannoch and Etive formations in the Oseberg Field. The Rannoch Formation is about

4-5 m thick, while the Etive Formation is 1-12 m thick in the northern parts of the field (Johnsen et al., 1995).

Ness Formation: The total thickness of the Ness Formation of the Oseberg field varies from 20 to 102 m. The stratigraphy is a complex sequence of interbedded sandstone, siltstone, shales and coals, which represents a delta-plain paleo-environment. The sandstone varies in origin and represents fluvial channels, crevasse splays, levees and bay fills (Johnsen et al., 1995; Spencer et al., 1987).

Tarbert Formation: The formation is more thickly developed down-flank while in the central and up-flank parts of the Alpha structure are eroded by the Callovian and Base Cretaceous unconformities. The formation is thought to be a transgressive sandstone.

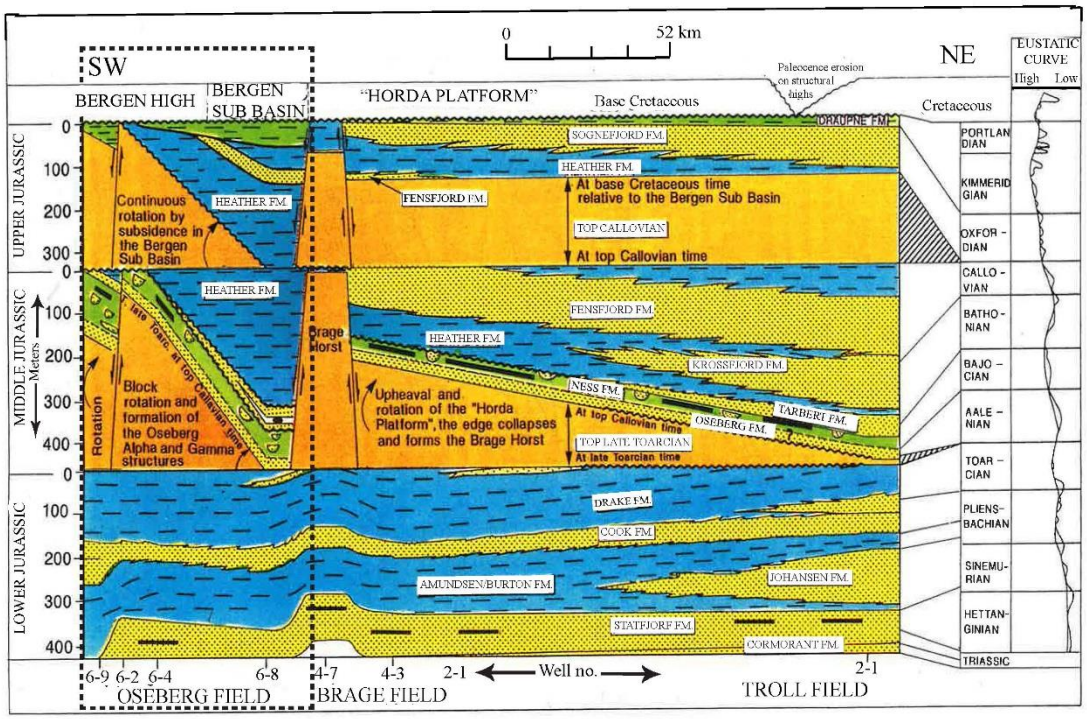

Figure 8: Generalized SW-NE tectonostratigraphic cross-section, including curves of global sea level fluctuations, the Oseberg Area is highlighted in the dotted black box. Modified Haq, Hardenbol, and Vail (1987); (Johnsen et al., 1995).

2.3 HYDROCARBON RESERVES

The gas-cap of the Oseberg Field is a moderately wet gas with a gas-oil ratio of about 3200 Sm^3/Sm^3. The properties of oil vary with depth. With increasing depth, the heavy components in oil increases, while the methane gas content and saturation pressure decrease. Extremely high productivity has been observed in the hydrocarbon bearing zones of the Etive Formation. Ideal productivity indices of 415-1950 Sm^3/day/bar for the oil zone, and 360,000-780,000 Sm^3/day/bar for the gas zone, have been derived from well test data interpretations. In the Field Development Plan the recoverable oil reserves for the Oseberg Field were estimated to be 153×10^6 Sm^3, about 43% of original oil in place. In addition, approximately 7×10^6 Sm^3 of condensate can be recovered from the gas production (Spencer et al., 1987)

3. DATABASE

In this section the available and used dataset is discussed. The data set comprises of seismic and well log data. Important details about dataset are given in following sections.

3.1 SEISMIC AND WELL LOG DATA

The seismic 3D cube provided for this project, covers the Block 30/9 Oseberg Sør J. The data was delivered by Statoil, project number ST14206D14 (Figure 9). The details of seismic data are comprised in Table 1. Along with the seismic CMP gathers, available for PP and PS, the data also contains PSDM velocities (V_P and V_S). The PP angle stacks have three sets of angles; near, mid and far, ranging from 0-15º, 15-30º and 30-45º. The PS angle stacks (0-15º, 15-30º and 30-45º) were derived by Wiktor Waldemar Weibull (UiS) from the PS CMP gathers given in PP time.

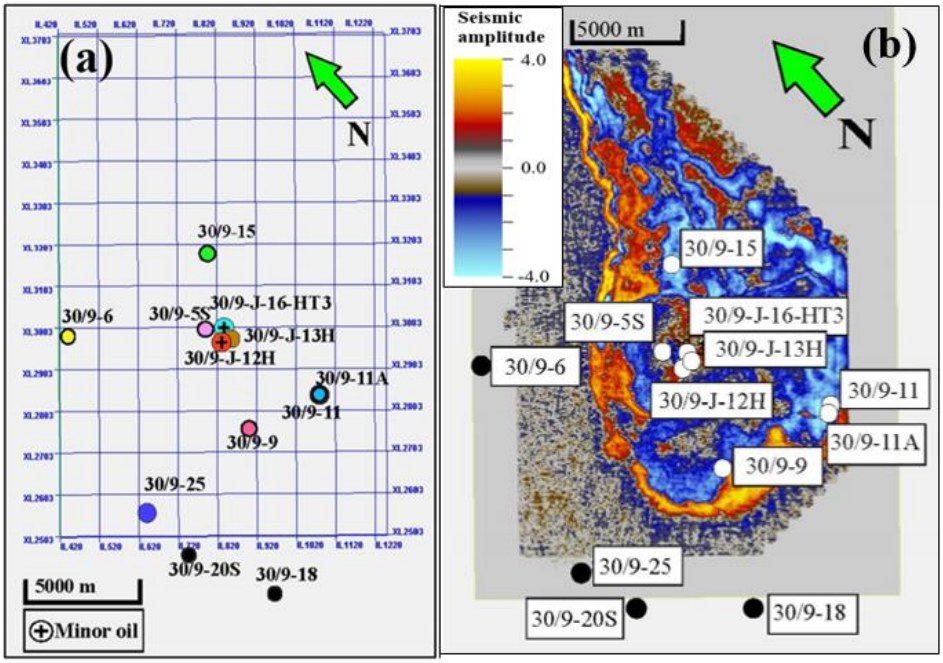

Figure 9: (a) A 2D map view of 3D seismic cube, showing the Xl-cross line (2503-3703), IL- inline (420-1220). (b) Time slice at reservoir depth ca -2100ms, highlighting the locations of all wells. High impedance (red color), low impedance (blue color).

The frequency range of PP seismic data is approximately from 8 to 55Hz while for PS it is up to 45Hz (Figure 10). The sample interval is 4ms. The SEG polarity system was used for PP seismic data while the European polarity system was used for PS seismic sections. The reason for the different polarity is explained in chapter 5 and 6. The SEG has a typical polarity in which a red peak means a “hard” or “positive” kick which corresponds to an increase in acoustic impedance with time/depth. However, the European polarity is opposite of it, in which a blue peak means a “hard” or “positive” kick, is increase in an acoustic impedance with time/depth.

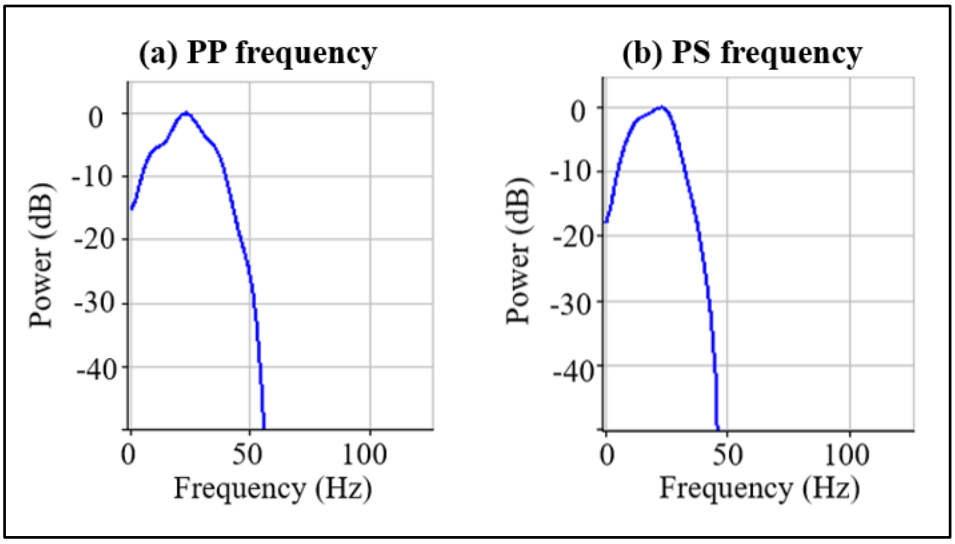

Figure 10: Frequency spectrum of both seismic sections. (a) Displays the frequency range of PP seismic section, which is more than 50Hz. (b) Shows the frequency range for PS seismic section, which is less than 50Hz.

Table 1: Seismic dataset details

Seismic Gathers	Full Stacks	Angle Stacks
PP in PP time	√	√
PS in PP time	√	√
PP in depth	√	√
PS in depth	—	—

The well data comprises of 12 wells, two of them are outside the given seismic cube. The wells with the available logs, are summarized in Table 2. Three exploration wells, 30/9-11, 30/9-9, 30/9-5S, and one development well, 30/9-J-13H was used for the evaluation. The well log data has electrical logging and lithological mud logging data. The four study wells are shown in Figure 11, with reservoir zone between the Shetland Group and the Drake Formation. As the well log data lacks in important logs (Table 2), the gas water contact (GWC) and gas oil contact (GOC) is marked in one well 30/9-J-13H by interpreting the density (RHOB), porosity (NPHIE) and water saturation (SWE) logs (Figure 11). One thing is also important to note, only well 30/9-J 13H has both measured and calculated shear sonic log, whilst other wells just have calculated shear sonic log.

Table 2: All wells are shown with the important logs which are used for study. The logs are GR: Gamma ray, SWE: effective water saturation, AI: acoustic impedance, SI: shear impedance, RHOB: density and NPHIE: neutron porosity.

Wells	GR	SWE	AI	SI	RHOB	NPHIE
30/9-5S	—	—	√	√	√	—
30/9-11A	—	—	√	√	√	—
30/9-15	—	—	√	√	√	—
30/9-11	—	—	√	√	√	—
30/9-9	—	—	√	√	√	—
30/9-J-13H	√	√	√	√	√	√
30/9-J-16HT3	—	—	√	√	√	—
30/9-J-12H	—	—	√	√	√	—
30/9-25	—	—	√	√	√	—
30/9-6	—	—	√	√	√	—
30/9-18	—	—	√	√	√	—

30/9-20S	—	—	√	√	√	—

3.2 SEISMIC CHARACTERISTICS

A composite seismic section is elaborated in Figure 12 to clarify the seismic characteristics of the reservoir zone (area of interest) relative to the study wells. This composite seismic section is created by using different cross and in-lines, which are passing through four study wells. The wells are shown along with the acoustic/P-impedance log. The Shetland Group is showing the high impedance (red color on seismic section and pink on acoustic impedance log), as most of the upper part of Shetland Group is consist of carbonates. Also, the high acoustic impedance can be observed from logs in Figure 11, where it is marked by the top Shetland Group.

3.3 SOFTWARE

The software used for this project is *PETREL*. The tools used for this study are mainly, seismic well tie, interpretation tool, point editing, well correlation, log conditioning, 2D forward modeling, simultaneous inversion, rock physics tool, litho-cube analysis and prediction, QI cross plot and RockDoc QI plug-in.

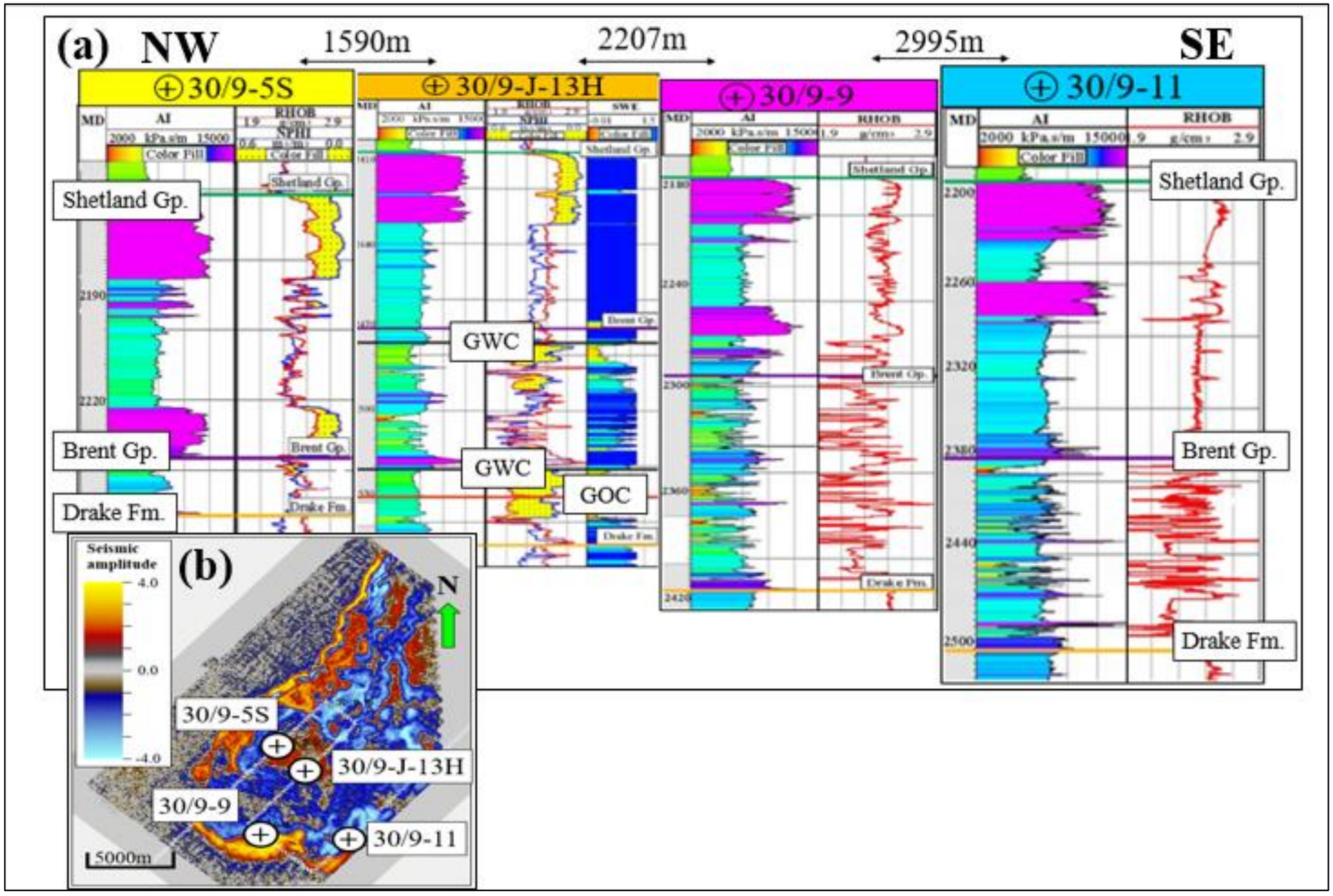

Figure 11: (a) SE-NW cross section of wells, along acoustic impedance (AI), density (RHOB) and water saturation (SWE) logs. The tops of the Shetland and the Brent Group and the Drake Formations are marked. Gas-water contact (GWC) and gas-oil contact (GOC) are marked in well 30/9-J13H.(b) The location of wells is shown on a times-slice, at reservoir depth approximately -2100ms.

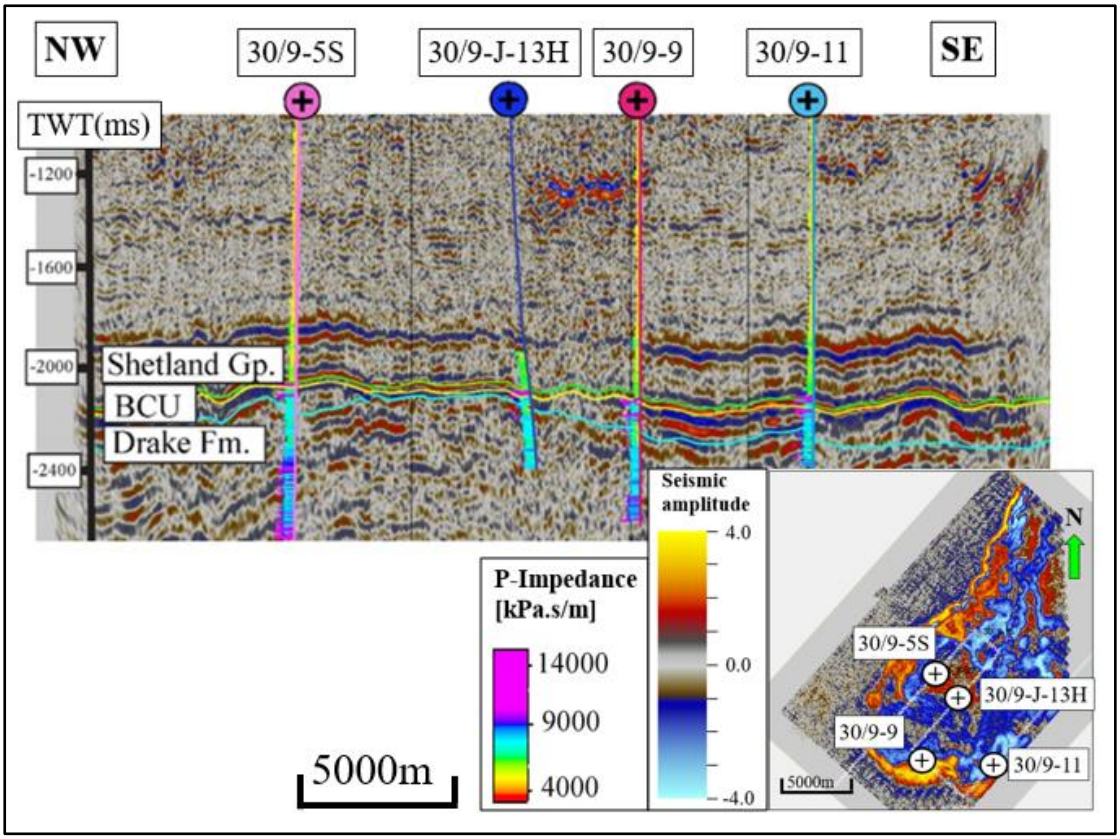

Figure 12: A SE-NW composite cross-section, along with study wells. Acoustic impedance log (P-impedance) is shown which is compared to high amplitudes on seismic section. The inset figure shows the location of wells on a time slice at reservoir depth.

4. THEORETICAL BACKGROUND

In this section, the importance of converted waves is debated. With special emphasis to quantitative interpretation. In addition, the use of AVO data and analysis to predict the lithology and fluid distribution is discussed.

4.1 COMPRESSIONAL WAVES (P-WAVES) SURVEY AND PROBLEMS

In the past 75 years, the petroleum industry has been applying seismic technology, since then the compressional waves (P-waves) always played an important and dominant role over shear/converted waves (S/ PS waves). P-waves are used in exploration surveys for good reasons, i.e. P-waves arrive first, usually have high signal to noise ratio (S/N), their particle motion is nearly rectilinear, they can propagate in marine environment and can be produced by variety of sources. Since the beginning of the exploration history, compressional wave seismic survey has been evolved from two- to three dimensional (2D to 3D). Recently a new technique, a fourth dimension with 4D time-lapse has been introduced. Till now compressional waves have achieved adequate results, and countless reservoirs have been discovered and characterized (Barkved et al., 2004; Caldwell et al., 1999; Stewart, Gaiser, Brown, & Lawton, 1999).

Compressional waves are still considered as a powerful technique for exploration, however they cannot solve every reservoir problem. In many cases, though the P-waves can identify the target, however fail to delineate its extension. This problem is more common where the stratigraphic traps are present, in these traps the reservoirs pinch out and laterally replaced by other lithology. Even if the compressional waves are able to detect the lateral or time-lapse change in reservoir properties, still it would be unable to distinguish different rock properties such as lithology, change in fluid content or formation pressure (Barkved et al., 2004; Caldwell et al., 1999).

Compressional wave surveys show the bright spots and other amplitude anomalies, however these anomalies and bright spots can be mistaken for a hard-tight

rock instead of hydrocarbon accumulation, unless additional information is provided. Also, the behavior of P-waves can be less sensitive towards fractures in reservoir. Sometimes, reservoirs or overlying strata have a texture which impose azimuthal variation of velocities or other types of anisotropy that can have an effect on P-wave seismic survey (Caldwell et al., 1999).

In addition to these problems, compressional surveys sometimes also have difficulties with imaging the rock strata. If there is just a small amount of gas accumulated in layers of the overburden, it can create so-called gas chimneys above leaking gas accumulations, this may have a negative impact on imagining the subsurface and the reservoir. Some reservoirs do not have a strong impedance in comparison to overlying burden, so they do not reflect P-waves that strongly to produce an interpretable reflection. In some reservoirs, where the overburden is itself a high impedance stratum such as a volcanic rock or salt, the underlying reservoir is difficult to image. In this case a small amount of energy returns to surface after transmitting twice through the high impedance rock, and thus cannot deliver full information (Barkved et al., 2004; Caldwell et al., 1999).

4.2 CONVERTED WAVES (PS-WAVES)

Converted waves (PS-waves) provide very useful additional information and are increasingly being used in the petroleum industry to complement the information coming from the compressional waves. Numerous authors (e.g.(Kristiansen, 2000)) have suggested or shown a number of applications of converted wave seismic survey data, which include (Stewart, Gaiser, Brown, & Lawton, 2003):

- PS data provide other complete independent properties such as velocity, multiples, tuning etc.
- PS data may show a significant change in impedance contrast as compared to P-waves data (Figure 13)

- Provides interpretable images through gas chimneys, mud volcanoes, shale diapirs and beneath salt and basalt (Figure 14)
- Contribution in lithology discrimination and fluid content by using V_P/V_S ratio (e.g. sand/shale and hydrocarbon sand/ brine sand
- It may improve structural imaging
- Helps to characterize the fractures in reservoir, better than compressional waves
- Improves conventional AVO analysis and AVO inversion for density and velocity
- Monitoring reservoir changes (time lapse or 4D)

The addition of converted waves, may deliver more information, producing better and reliable results in exploration industry.

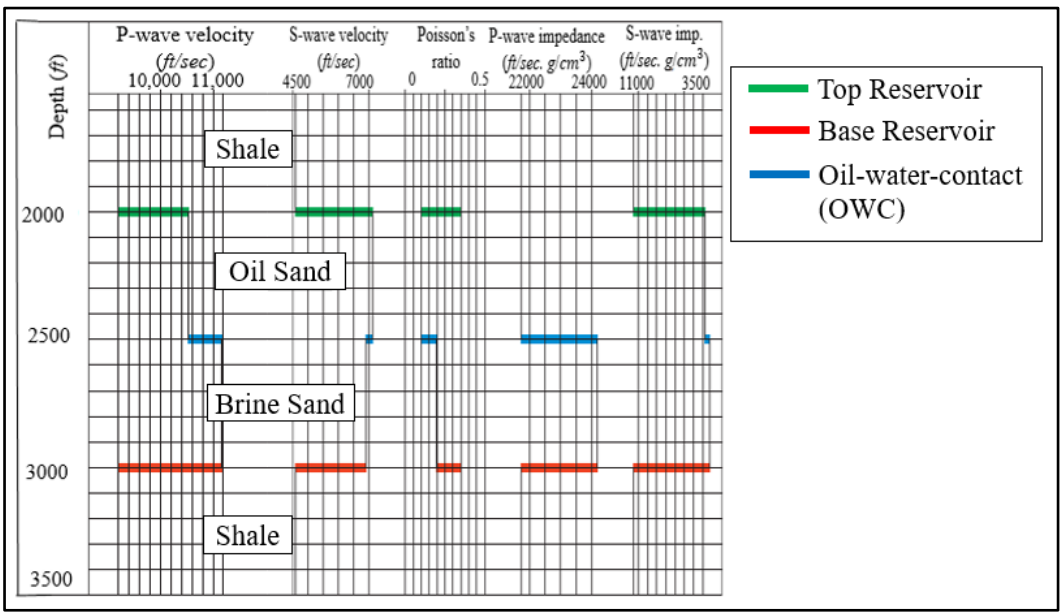

Figure 13: Digram showing the P and S impedance behaviour. In track 1, the P-wave velocity is increasing at the top of thereservoir (green). The lack of P-impedance contrast across the interface results in weaker/no P-wave reflection. On the other hand, the S-wave velocity has a large contrast (track 2), giving rise to a large shear impedance as it is not effected by the hydrocrabon fluid in the reservoir. Poisson's ratio (track 3) is a funtion of V_P/V_S, and sometimes predicts the rock and fluid properties. Modified after Caldwell et al. (1999)

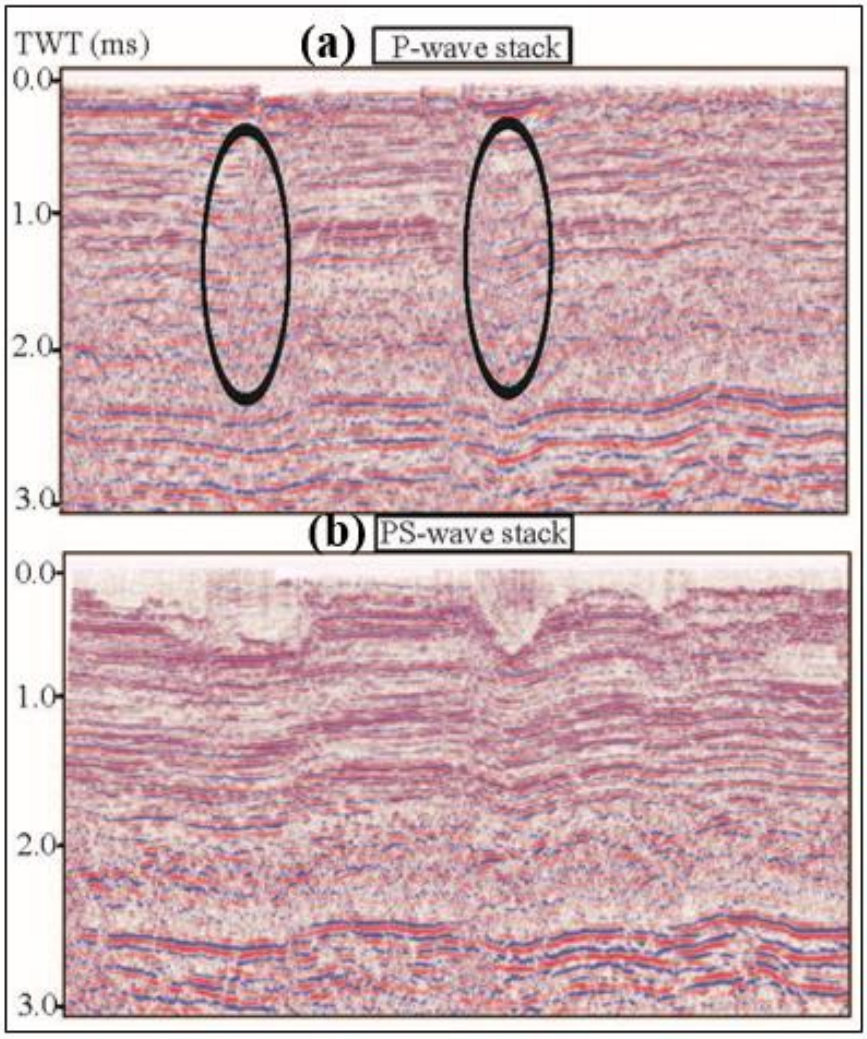

Figure 14: Comparison between P- and PS- waves, 2D section over North Sea shallow gas chimneys. (a) The marked area by circles of the P-wave seismic section shows reverberations and high frequency attenuation because of gas chimneys lies beneath the subsurface. (b) However, the PS-wave section shows the good imagining under the gas clouds, where P-wave section is inadequate. Modified after Stewart et al. (2003)

4.2.1 Seismic energy portioning and conversion

When a seismic P-wave arrives at an interface, separating two media of different elastic properties, it gives rise to reflected, transmitted and in case of non-normal incidence, converted waves. The nature of the two media determines the densities, elastic constants and thus velocities. The waves whose modes change at an interface

(reflected or transmitted S-waves) are called converted waves (PS- or C waves) (Figure 15).

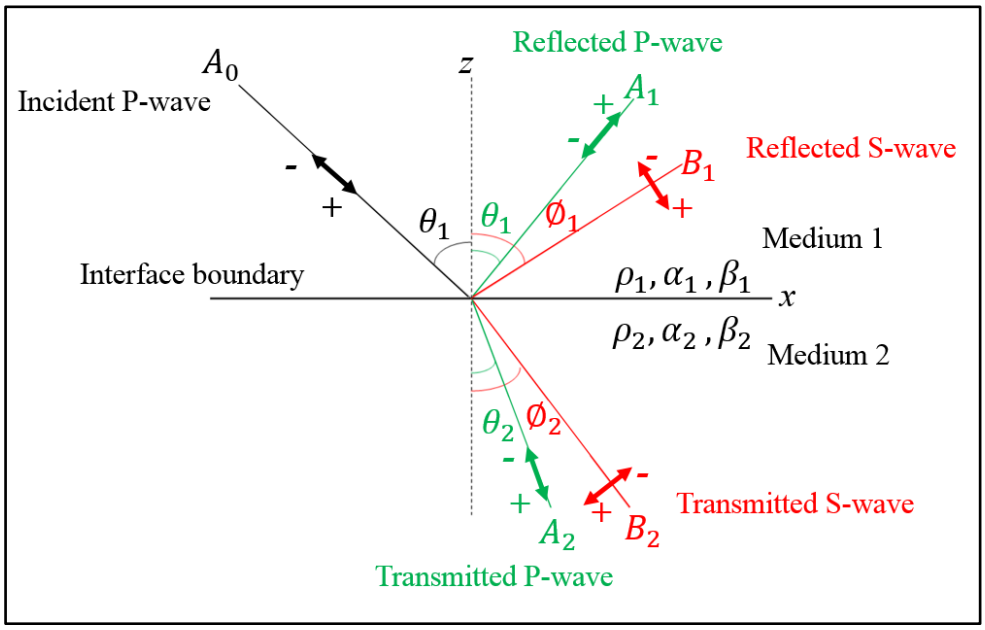

Figure 15: Schematic diagram of wave energy portioning. A P-wave propagates through a medium 1 of density (ρ_1), P-wave velocity (α_1), S-wave velocity (β_1). The medium 2 has a density (ρ_2), P-wave velocity (α_2) and S-wave velocity (β_2). The angle θ_1 and θ_2 are the reflected and transmitted angle for P-wave, while ϕ_1 and ϕ_2 are the reflected and transmitted angles for S-wave respectively. A_1 and A_2 are the amplitudes for P-wave velocity, while B_1 and B_2 are amplitudes for S-wave for reflected and transmitted energy respectively. Negative and positive signs show the direction of displacement of amplitudes. Modified after Sheriff and Geldart (1995).

The relationship between incident, reflected and transmitted waves at the reflector is described by Snell's law. This law can also be used for converted waves:

$$\frac{sin\theta_1}{\alpha_1} = \frac{sin\emptyset_1}{\beta_1} = \frac{sin\theta_2}{\alpha_2} = \frac{sin\emptyset_2}{\beta_2} = p \qquad \textit{(Eq. 1)}$$

While;

θ_1 , θ_2 = Reflected and transmitted angles of P-wave respectively

$\emptyset_1, \emptyset_2$ = Reflected and transmitted angles of S-wave respectively

α_1 and β_1= P- and S-wave velocities in medium 1

α_2 and β_2 = P- and S-wave velocities in medium 2

p = Ray path (Component of slowness of each ray in Figure 15 parallel to interface)

When a P-wave reflects from an interface, its angle of incidence is equal to the angle of reflection. However, for a converted PS wave, the angle of reflection (S-wave angle) is not equal to incidence P-wave angle (Figure 16). This asymmetry is explained by Snell's law; $sin\theta/\alpha = sin\emptyset/\beta$, with $\beta<\alpha$ and consequently $\emptyset<\theta$. Thus S-wave reflects under a smaller angle than P-wave (Barkved et al., 2004; Sheriff & Geldart, 1995; Stewart et al., 1999).

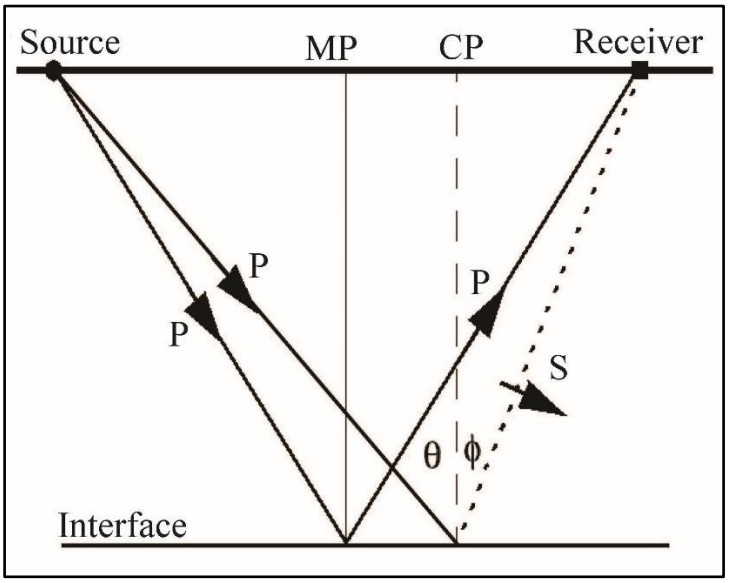

Figure 16: A schematic diagram explaining the conversion point (CP) of a converted wave (PS-wave). The P-wave has a reflection point which is a mid-point, and the incident angle is equal to reflected angle. However, in case of a converted wave, the incident angle (P-wave) is not equal to reflected angle (PS-wave). Modified after Stewart et al. (1999).

4.2.2 Amplitudes and reflection coefficients

The strength of the reflection from an interface depends on the properties of that medium or layer where it takes place, such as velocity and density. The reflection coefficient is a fundamental part of all kinds of amplitude analysis such as AVO, inversion and different kind of attribute mapping. A reflection/transmission coefficient for a normal incident plane wave is a ratio between reflected/transmitted amplitude and incidence amplitude. Boundary conditions allow to calculate how wave energy is divided between reflected and transmitted waves. The reflection and transmission coefficients are shown in following equations:

$$R_{PP} = \frac{A_r}{A_0} = \frac{Z_2 - Z_1}{Z_2 + Z_1} \qquad \textit{(Eq. 2)}$$

$$T_{PP} = \frac{A_t}{A_0} = 1 - R_c = \frac{2Z_1}{Z_1 + Z_2} \qquad \textit{(Eq. 3)}$$

While:

R_{PP}= Reflection coefficient

T_{PP} = Transmission coefficient

A_r = Reflection amplitude

A_t = Transmission amplitude

A_0 = Incident amplitude

Z_1= Acoustic impedance in medium 1= $\rho_1 V_1$

Z_2= Acoustic impedance in medium 2 = $\rho_2 V_2$

The above equations explained that the reflection amplitude varies with change in acoustic impedance. If the acoustic impedance contrast is weak between two media, then the normal incidence coefficient is approximately given by:

$$R = \frac{1}{2}\frac{\Delta Z}{Z} \approx \frac{1}{2}\left(\frac{\Delta \alpha}{\alpha} + \frac{\Delta \rho}{\rho}\right)$$

(Eq. 4)

While;

Z is the average acoustic impedance between medium 1 and 2

$\Delta Z = Z_2 - Z_1$

$\alpha = \alpha_2 + \alpha_1$

$\Delta \alpha = \alpha_2 - \alpha_1$

$\rho = \rho_2 + \rho_1$

$\Delta \rho = \rho_2 - \rho_1$

Whereas α is the P-wave velocity and ρ is the density of the either medium.

4.3 ZOEPPRITZ EQUATIONS

The approaches which are most understood, in terms of derivation of amplitudes, are Knot and Zoeppritz equations. Knot calculated these equations by using potential functions while Zoeppritz used displacements. The mathematical derivation of these amplitudes is more complicated than normal incidence, however the principles are same. Zoeppritz calculated the amplitudes of reflected and transmitted waves at a plane interface for an incident P-wave. (Knot, 1899; Sheriff & Geldart, 1995; Telford, Telford, Geldart, & Sheriff, 1990; Zoeppritz, 1919).

Zoeppritz solution is constructed on a set of four equations (Eq. 5). These four equations are based on reflected and transmitted components of P- and S-waves (Converted waves) in both media and the angles of each with respect to normal (Ganssle, 2012). The Zoeppritz equations which describe the relation of reflection and transmission energy from a plane interface in elastic media (Waters, 1987) are:

$$\begin{bmatrix} sin\theta_1 & cos\emptyset_1 & -sin\theta_2 & cos\emptyset_2 \\ -cos\theta_1 & sin\emptyset_1 & -cos\theta_2 & -sin\emptyset_2 \\ sin2\theta_1 & \frac{\alpha_1}{\beta_1}cos2\emptyset_1 & \frac{\rho_2\beta_2^2\alpha_1}{\rho_1\beta_1^1\alpha_2}sin2\theta_2 & -\frac{\rho_2\beta_2\alpha_1}{\rho_1\beta_1^2}cos2\emptyset_2 \\ cos2\emptyset_1 & -\frac{\beta_1}{\alpha_1}sin2\emptyset_1 & -\frac{\rho_2\alpha_2}{\rho_1\alpha_1}cos2\emptyset_2 & -\frac{\rho_2\beta_2}{\rho_1\alpha_1}sin2\emptyset_2 \end{bmatrix} \begin{bmatrix} A \\ B \\ C \\ D \end{bmatrix} = \begin{bmatrix} -sin\theta_1 \\ -cos\theta_1 \\ sin2\theta_1 \\ -cos2\emptyset_1 \end{bmatrix}$$

(Eq. 5)

While, α and β are the P and S-waves velocities, θ and ϕ are the angles of reflection and transmission respectively and ρ defines the density. Whereas the subscripts 1 and 2 refer to the medium 1 and 2.

4.4 LINEAR APPROXIMATIONS TO ZOEPPRITZ EQUATIONS

Zoeppritz equations give the reflection and transmission coefficients for a plane incident P-wave, as a function of incidence angle. These equations as described in previous section, depend on six different parameters; P- and S-wave velocities and density, three on each side of a reflecting interface. However, Zoeppritz equations are highly non-linear, which makes them complex to use for practical purpose and it consumes a lot of CPU time in mathematical computation. Thus a number of linear approximations were purposed by various authors [e.g. Bortfeld (1985); Chapman (1976); Aki and Richards (1980); Shuey (1985); Hilterman (1989); Smith and Gidlow (1987); and Fatti et al (1994)] to simplify these equations and to decrease the computation time (Ganssle, 2012; Ilesanmi, 2013; Shuey, 1985). In this section some of the important approximations which are mostly used in this project, are discussed briefly.

4.4.1 Bortfeld's approximation

Bortfeld (1961) derived his approximation by using Poisson's Ratio. He separated the reflection and transmission coefficients into three terms; normal incident, a fluid factor and a rigidity factor term (Ganssle, 2012; Verwest, 2004).

$$R_{PP}(\theta_1) = \frac{AI_2 - AI_1}{AI_2 + AI_1} - 2p^2\left[(\beta_2^2 - \beta_1^2) + \beta^2\frac{\rho_2 - \rho_1}{\rho_1}\right]$$

(Eq. 6)

Where $p = {sin\theta_1}/{\alpha_1}$ is ray parameter, *AI* is Acoustic impedance and β is S-wave velocity. The subscripts 1 and 2 indicates the respective layer or medium. The subscript *PP* refers to this solution as a reflection coefficient of an incident P-wave, as reflected a P-wave.

4.4.2 Aki and Richard's approximation

Aki and Richards (1980) formulated their approximation as a function of relative contrast, for the PP reflection coefficient. They introduced the coefficients of PS waves converting from P waves. They used three rock properties to separate the terms; P-wave, S-wave and density (Aki & Richards, 2002; Ganssle, 2012).

$$R_{PP}(\theta_1) = \frac{1}{2}(1 - 4\beta^2p^2)\frac{\Delta\rho}{\rho} + \frac{1}{2cos^2\theta}\frac{\Delta\alpha}{\alpha} - 4\beta^2p^2\frac{\Delta\beta}{\beta}$$

(Eq. 7)

$$R_{PS}(\theta_1) = \frac{-\alpha tan\emptyset}{2\beta}\left[\left(1 - \frac{2\beta^2}{\alpha^2}sin^2\theta + \frac{2\beta}{\alpha}cos\theta cos\emptyset\right)\frac{\Delta\rho}{\rho} - \left(\frac{4\beta^2}{\alpha^2}sin^2\theta - \frac{4\beta}{\alpha}cos\theta cos\emptyset\right)\frac{\Delta\beta}{\beta}\right]$$

(Eq. 8)

Where again; α, β and ρ are the average P-wave velocity, S-wave velocity and density respectively. While $\Delta\alpha/\alpha$, $\Delta\beta/\beta$ and $\Delta\rho/\rho$ are the contrasts of these properties between two layers. θ_1 is the angle of incidence for incident wave. The subscripts denote the respective layer. Ray parameter p and θ contain the angle information, which is eliminated by using following equation.

$$sin^2\theta = \alpha^2p^2$$

(Eq. 9)

In Figure 17, a comparison is shown between Zoeppritz reflection coefficient of the non-linear equations and its linear approximation of Bortfeld and Aki & Richards. The approximations deviate from the Zoeppritz equations at large angle of incidence.

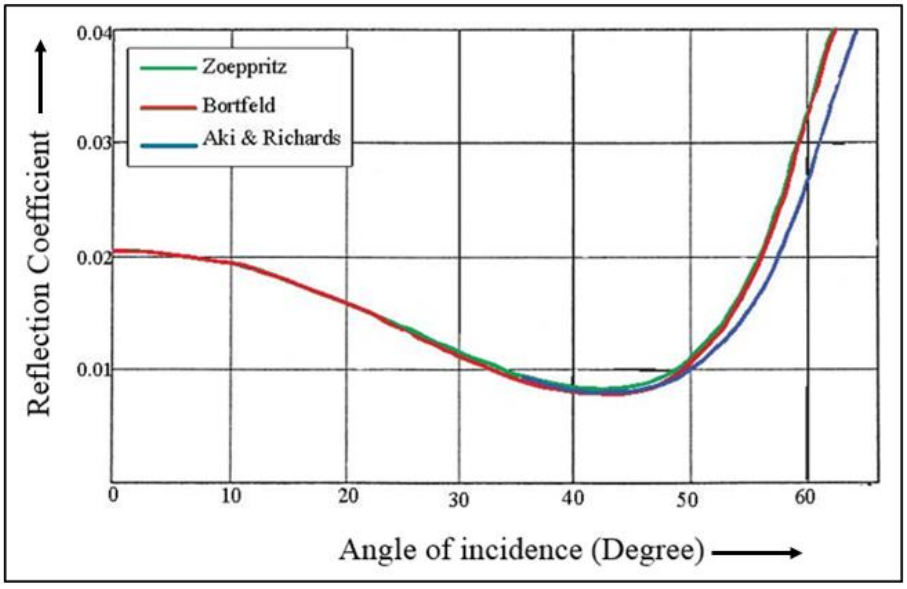

Figure 17: Comparison between Zoeppritz reflection coefficient with its linear approximations presented by Aki & Richards (1980) and Bortfeld (1961). Model follows the values; $Model = \frac{\alpha_1=3000,\ \beta_1=1414,\ \rho_1=2.40}{\alpha_2=3100,\ \beta_2=1500,\ \rho_2=2.42}$ *. Modified after SEG*

4.4.3 Shuey's approximation

The Shuey (1985) equation consists of three terms called intercept, gradient and curvature. These terms are loosely related to near, mid and far offsets/angles respectively. The three term Shuey approximation can be described as:

$$R_{PP}(\theta_1) = R_0 + \left[A_0 R_0 + \frac{\Delta\sigma}{(1-\sigma)^2}\right] sin^2\theta + \frac{1}{2}\frac{\Delta V_P}{V_P}(tan^2\theta - sin^2\theta) \qquad \textit{(Eq. 10)}$$

Where, the parameters are already described in previously discussed equations, and σ is the Poisson's ration. The first term gives the reflection coefficient at normal incident (*θ=0*). The second term plays an important role at intermediate angles and introduces

the shear wave velocity effect by using the Poisson's ratio, while the third term becomes significant at angles which are approaching towards critical angles. (Shuey, 1985)

4.4.4 Fatti's approximation

Fatti et al. (1994) purposed their approximation as a function of acoustic impedance (Z_P), shear impedance (Z_S) and density (ρ) to define the reflectivity (Booth, Emir, & Diez, 2015):

$$R_{PP}(\theta_1) = \frac{1}{2}(1 + tan^2\theta)\frac{\Delta Z_P}{Z_P} - 4k^2 sin^2\theta \frac{\Delta Z_S}{Z_S} - \left(\frac{1}{2}tan^2\theta - 2k^2 sin^2\theta\right)\frac{\Delta\rho}{\rho} \quad \textit{(Eq. 11)}$$

Where $k=\beta/\alpha$ is the S-wave velocity to P-wave velocity ratio. For angles below ca 35°, the last term of Fatti's approximation is close to zero, and for this angle range Fatti purposed a two-term approximation:

$$R_{PP}(\theta_1) = \frac{1}{2}(1 + tan^2\theta)\frac{\Delta Z_P}{Z_P} - 4k^2 sin^2\theta \frac{\Delta Z_S}{Z_S} \quad \textit{(Eq. 12)}$$

4.5 SEISMIC INVERSION

The basic idea of seismic inversion is to estimate the properties across earth layers from the amplitudes of reflected waves coming from the interfaces between them. The properties of the earth layers could be physical or geological, and thus the seismic inversion is quantitative interpretation of seismic measurement. This is helpful to characterize the reservoir properties. In general, the inversion procedure is non-linear, however in practice it is linearized, and the final non-linear solution is obtained by applying iterative linearized solutions (Barclay et al., 2008; Wang, 2016).

4.5.1 Forward modelling and seismic inversion

The most common practice in inversion involves two steps; forward modelling and back propagation. Forward modelling includes a model, based on layers with

estimated formation properties such as depth, thickness, velocities and densities derived from well logs. The simplest model which calculates the acoustic impedance, involves the P-wave velocity and the bulk density. An acoustic impedance does not contain any information about elastic or S-wave velocity. However, the model which delivers the elastic or shear impedance includes the S-wave velocity and bulk density of the rock layers. The model is then used as an input to the Zoeppritz equations or any of its approximations to create an angle dependent reflectivity model. The angle dependent reflectivity model is then convolved with a seismic wavelet to create a modelled seismic trace called synthetic seismic trace (Figure 18(a)) (Barclay et al., 2008; Wang, 2016).

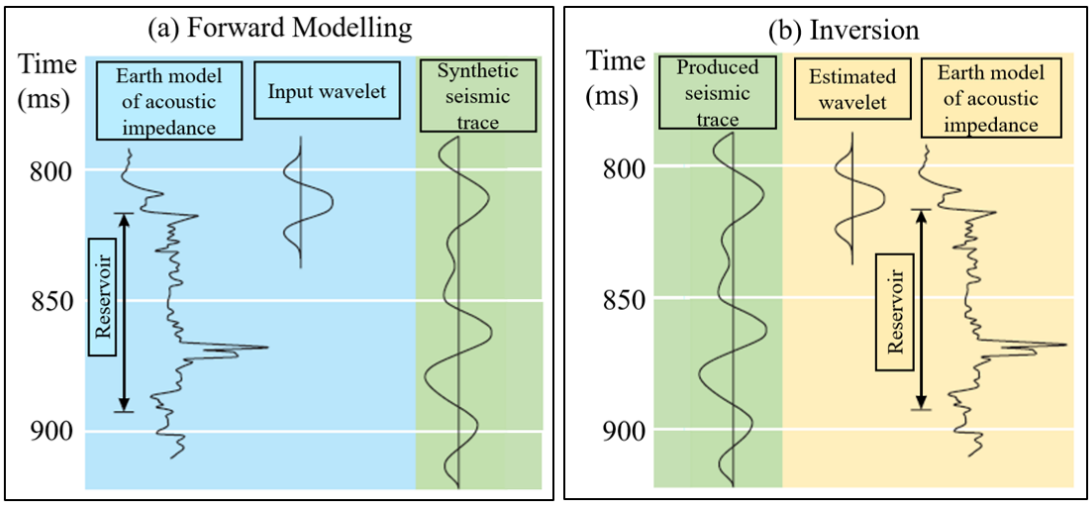

Figure 18: A schematic diagram explaining the forward modelling and inversion. (a) Shows how a synthetic trace is created by convolving the reflectivity model and wavelet. (b) Describes that an acoustic model is created by convolving seismic trace and a wavelet, which is inversion. Modified after Barclay et al. (2008).

Inversion uses the observed seismic traces and provides and earth layer model for subsurface. To achieve a best fit model, most inversions iterate the forward modelling and back propagation, to minimize the difference between synthetic and seismic data (Figure 18(b)) (Barclay et al., 2008).

Figure 18 also explains the inversion and forward modelling in terms of convolution and reflectivity. A simple example of seismic inversion using only the normal incidence reflection is explained below:

Acoustic impedance is described as:

$$AI_{(i)} = V_{P\,(i)} * \rho_{(i)} \qquad \textit{(Eq. 13)}$$

While, V_P and ρ are the P-wave velocity and density of a layer, respectively. Now the seismic reflection coefficients or reflectivity is described as:

$$R_{(i)} = \frac{AI_{(i+1)} - AI_{(i)}}{AI_{(i+1)} + AI_{(i)}} \qquad \textit{(Eq. 14)}$$

While R represents the reflectivity. It is a common assumption that the seismic trace is a reflectivity, convolved with a seismic wavelet and added some noise as described in following equation:

$$S_{(t)} = R_{(t)} * W_{(t)} + N_{(t)} \qquad \textit{(Eq. 15)}$$

While, S is a seismic trace; R is seismic reflectivity; W is a wavelet and N is additional noise.

Going from the seismic traces to the acoustic impedance of the rock layers, is the objective of seismic inversion. One can say that, the seismic inversion involves the deconvolution, as the seismic response is replaced by a blocky signature corresponds to seismic impedance layering. The input for seismic inversion is mostly comprises of time migrated seismic data (pre- or post-stack), a wavelet and an initial earth model (velocity and density). Seismic inversion allows to estimate parameters which are useful in the reservoir characterization, under favorable circumstances it increases the data resolution (Veeken & Da Silva, 2004).

4.6 POST-STACK SEISMIC INVERSION

Post-stack seismic inversion is a processing technique whose aim is to deliver the acoustic impedance information from seismic stacked sections. In principal the process is straightforward, it involves the convolution of normal incidence ($\theta=0$) reflection coefficient and a seismic wavelet. Post-stack inversion can be classified into three methods; 1) Recursive methods; 2) Sparse-spike methods; 3) Model-based methods (Brian Russell & Hampson, 1991). However, only the basic concept of post-stack inversion will be discussed here.

The general concept of post-stack seismic inversion is illustrated in Figure 19. The inputs to the inversion consists of simply stacked seismic data and a geological constraint model. The seismic stacked data should be zero-offset. The initial impedance model is a low frequency model, to include the missing low frequencies in inversion (discussed in next section). The inputs are combined in a way to deliver the inversion results.

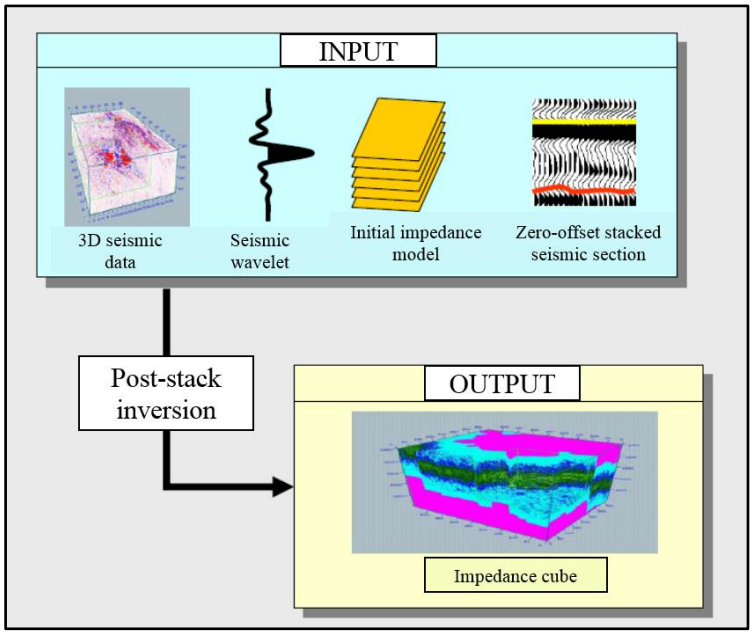

Figure 19: A schematic diagram explaining the post-stack inversion. The input for the post-stack inversion is a zero-offset seismic section from a 3D seismic cube, a wavelet, an optional impedance model. Modified after Veeken and Da Silva (2004).

4.6.1 Importance of low frequencies in inversion

The seismic data is band-limited, it fails to capture the highest and lowest frequencies. The lack of high frequencies has an impact on seismic resolution as wavelength λ which defines the resolution by well-known relationship $\lambda/4$ is given by $\lambda = {}^{v}/_{f}$ with v being the velocity of seismic wave. The low frequencies of the seismic have a major impact on the accuracy of impedance values. This fact is illustrated in Figure 20, which shows a simple impedance layer model that is filtered for three different frequency ranges; 10-80Hz, 10-500Hz, and 0-80Hz. When a wavelet of the frequency range 10-80Hz is used to invert the seismic data, the approximate thickness of layers is accurately imaged, however the absolute values of impedance and the interface shape are incorrect. When the wavelet with high frequency up to 500Hz is used, it resolves the thin beds but still the model is not accurate in terms of impedance cube. Only in case, when seismic includes the low frequencies down to zero Hz (0-80 Hz)(offset), the impedance model is correctly reflecting the true impedance distribution (Latimer, Davidson, & Riel, 2000).

In practice, most of the marine seismic data have a frequency range which starts from 5-8Hz. Thus, to include the low frequency information for the inversion via low frequency model (LFM), one can use log data, pre-stack depth or time migration velocities (Latimer et al., 2000; Ten Kroode et al., 2013). For this project, the low frequency models are created by using log data guided by seismic horizons (discussed in later sections).

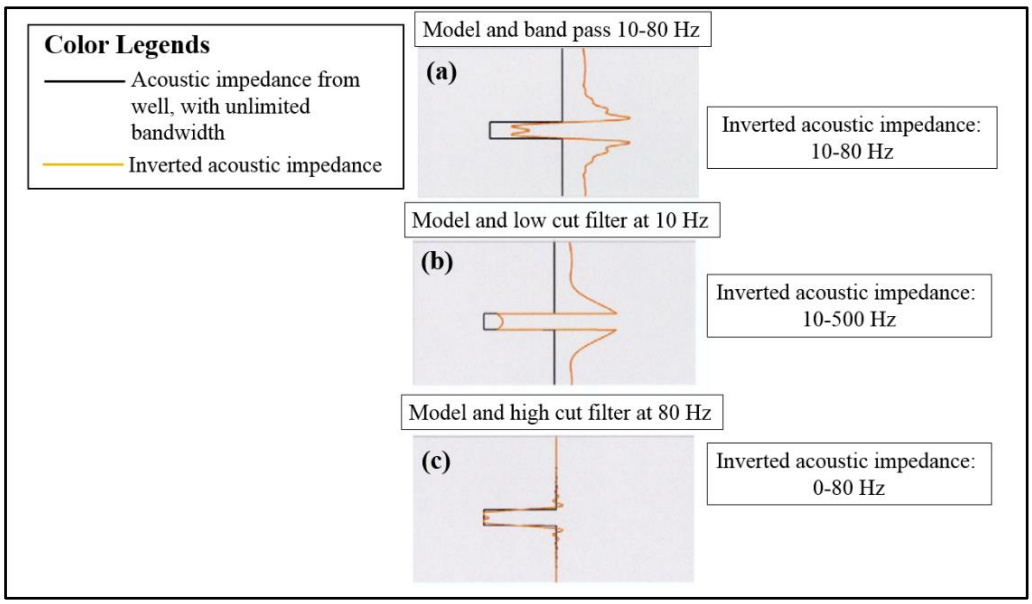

Figure 20: An impedance model explaining the importance of low frequencies in seismic inversion. (a) An inverted acoustic impedance using wavelet of 10-80 Hz, (b) An acoustic impedance created using wavelet of 10-500 (typically high frequencies) and (c) includes the low frequencies from 0-80 Hz. The model (c) gives a more reliable impedance comparison to acoustic impedance from well log. Modified after Latimer et al. (2000).

4.7. DISCUSSION OF AMPLITUDE VERSUS OFFSET (AVO) AND AMPLITUDE VERSUS ANGLE (AVA)

The Zoeppritz equations and its linear approximations discussed in sections 4.3 and 4.4, describe the dependency of the reflectivity with the angle of incidence at which the seismic wave strikes at an interface. However, the seismic data is recorded as a function of offset. Even if offset and angle are approximately similar, they have a nonlinear relationship that is dependent on the seismic velocity and the depth to the reflector. Therefore, a transformation of offset to angle is needed, before processing and analyzing the data using methods, which require seismic angles gathers instead of offsets gathers. An offset gather, and its correspondent angle gather are shown in Figure 21. A schematic ray path geometry is shown at the top of each gather. The incident angle decreases with depth for a constant offset trace, however the angle remains constant with depth for a constant angle trace. To transform the constant offset to

constant angle, a relationship between X (offset) and θ (incident angle) can be used, which derives the following equation (B Russell & Hampson, 2004):

$$X = Vt_0 tan\theta$$

(Eq. 16)

Thus Eq.16 is only valid for constant velocity, single mode and equal source and receiver datum, in which case it allows to map the amplitudes on an offset gather to amplitudes on an angle gather.

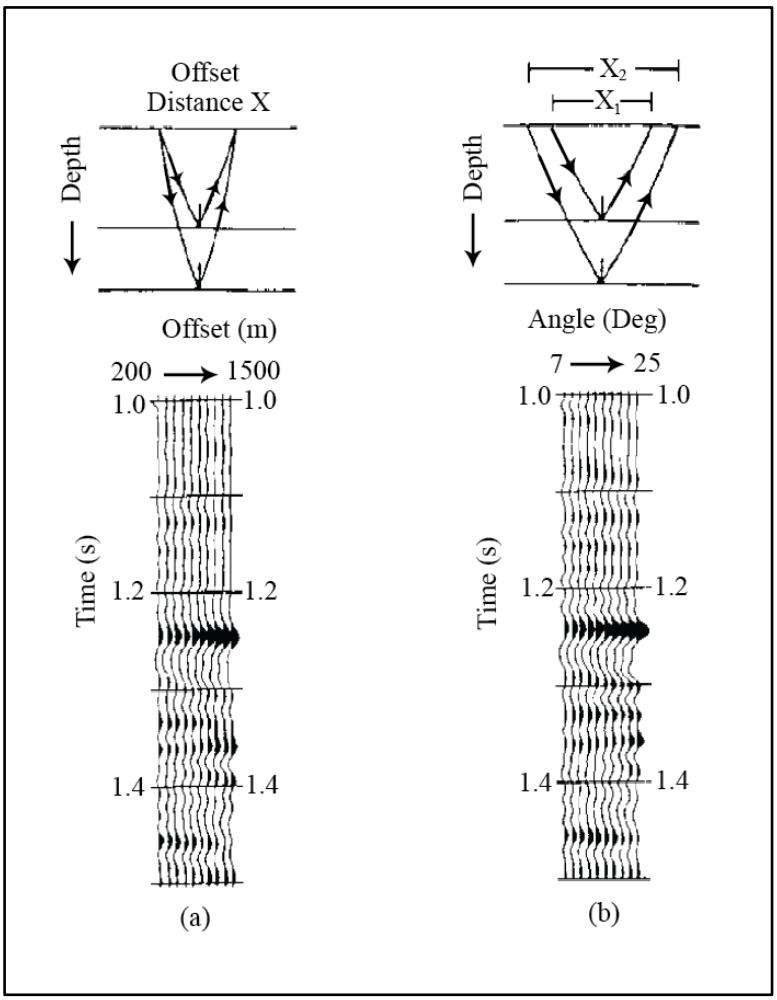

Figure 21: Schematic diagram showing the ray path geometry for offset dependent reflectivity (a) Shows AVO (amplitude versus offset) response while (b) shows transform of (a) in AVA (amplitude versus angle) response. Modified after B Russell and Hampson (2004).

4.7.1 Pre-stack simultaneous AVO inversion

The simultaneous inversion of pre-stack data includes the inversion of PP and PS angle stacks, which can be done separately or jointly. As previously mentioned, to understand the reservoir lithology and fluid content, it is useful to have S-waves or converted waves (PS-waves) to complement the information obtained from the P-waves. A diagram shows in Figure 22, represents how the AVO inversion works. The structural framework of a reservoir is shown, which contains the initial layer model to invert. The seismic data are angle stacks. The low frequency models are perturbed and for each angle stacks the reflectivity calculated using an approximation of the Zoeppritz equation and convolved with the wavelets extracted from the angle stacks. Finally, these synthetic data are compared with the measured angle stacks. The inversion is an iterative process which stops when some user defined criteria are matched. In general, the inverted parameters are acoustic impedance, shear impedance and the density cube which represent a perturbed version of provided low frequency models.

4.8 LITHOLOGY AND FLUID PREDICTION USING INVERSION

Reservoir characterization based on the lithology and fluid prediction from seismic data is very valuable in all phases of oil and gas exploration and production. With the application of simultaneous seismic inversion (PP and PS inversion), the improvement of prediction of lithology and fluid distribution across a reservoir is enhanced. The seismic amplitudes and amplitude variation angle/offset (AVA/AVO) deliver additional information about lithology, fluid type and quality of reservoir. Addition of converted waves (PS-waves) in inversion processes, (simultaneous PP&PS joint inversion), have greater impact on generating information about the density, lambda-rho ($\lambda\rho$ -incompressibility), Mu-rho ($\mu\rho$ - rigidity) (Davies, McInalley, & Barclay, 2003; Hammer, Kolbjørnsen, Tjelmeland, & Buland, 2012; Yoong, Lubis, & Ghosh, 2016). This is because the uniqueness of the shear waves. The S-waves are not directly affected by fluids as P-waves present in the reservoir. However, they can be

affected by fluid density, still S-waves can deliver reliable and precise information about rock lithology when combined with P-waves.

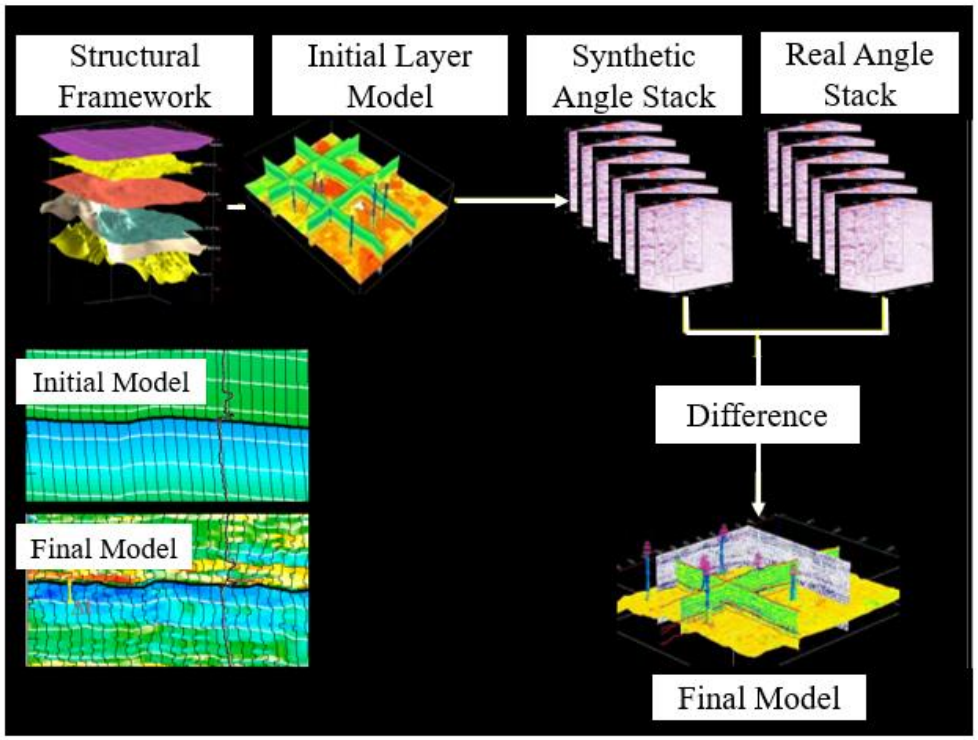

Figure 22: Figure showing the AVO inversion process, using the initial earth layer model and angle stack data. Modified after Hampson (2010).

4.9 Acquisition of converted waves

The particle motion of compressional waves is different from that of shear waves. For P-waves, the particle motion is parallel to the direction of propagation. When P-waves reflect from a horizontal reflector, their particle motion has a large vertical component at short to mid offsets, which is recorded by vertical component-geophones. However, shear waves are transverse waves, their particle motion is perpendicular to the direction of propagation, so the vertical component geophone is inadequate to record shear waves at these same offsets. S-waves are best recorded by

three component sensors (two perpendicular horizontal component and a vertical component) which allows to register and distinguish both P- and S- waves (Figure 23).

The typical marine seismic sources used in towed-streamer surveys do not directly generate S-waves. They generate P-waves, which convert partly to S-waves at the lithology boundaries of the subsurface. Therefore, these S-waves are called converted waves, PS-waves or C-waves as mentioned earlier. The P- and converted waves are registered by so-called Ocean Bottom Cable (OBC) that consists of four component sensors (three orthogonal geophones and a hydrophone) (Figure 23) (Barkved et al., 2004).

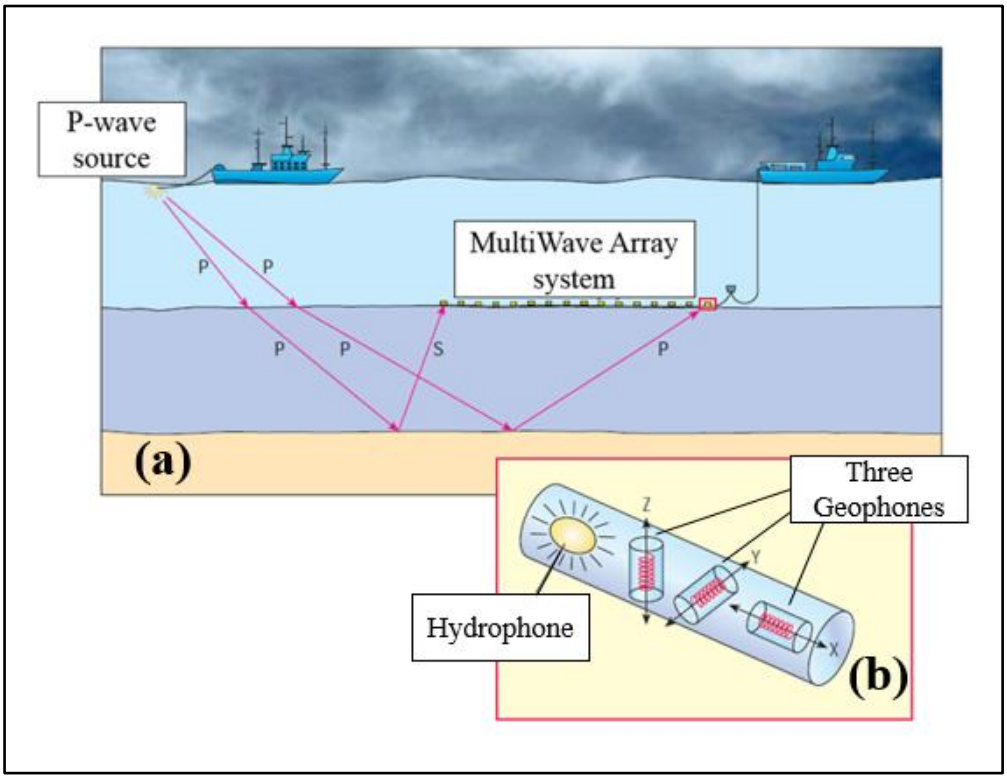

Figure 23: (a) Schematic diagram to show the recording of converted waves. The upgoing PS-wave is detected by a multicomponent receiver. (b) As shown in the inset, the multicomponent consists of one hydrophone and three orthogonally oriented geophones as X, Y and Z. Modified after Caldwell et al. (1999)

5. METHODOLOGY AND 2D SYNTHETIC DATA RESULTS

Synthetic data plays an important role in this project, as it is used to identify the most reliable inversion algorithm, which is used in the inversion of the data from the Oseberg Field.

5.1 PROPOSED WORKFLOW

The workflow is divided into four major steps; 2D forward modelling, low frequency model's construction, post-stack and AVO simultaneous inversion. Figure 24 exhibits the workflow of synthetic trace calculation for post-stack and angle stacks. The low frequencies have great impact on the accuracy of impedance and density estimation during inversion. Low frequency models of acoustic impedance (P-impedance), shear impedance (S-impedance) and density were designed to include the low frequencies in inversion. The workflow for this is shown in Figure 25. The Figures 26 and 27 explain the post-stack and pre-stack simultaneous inversion processes respectively which is operated on synthetic stacks data.

Five different types of inversions were achieved to estimate the best fitting and reliable inversion method. These inversion algorithms and their inverted output parameters are summarized in Table 3. These all four main algorithms are discussed in detail with results in following sections.

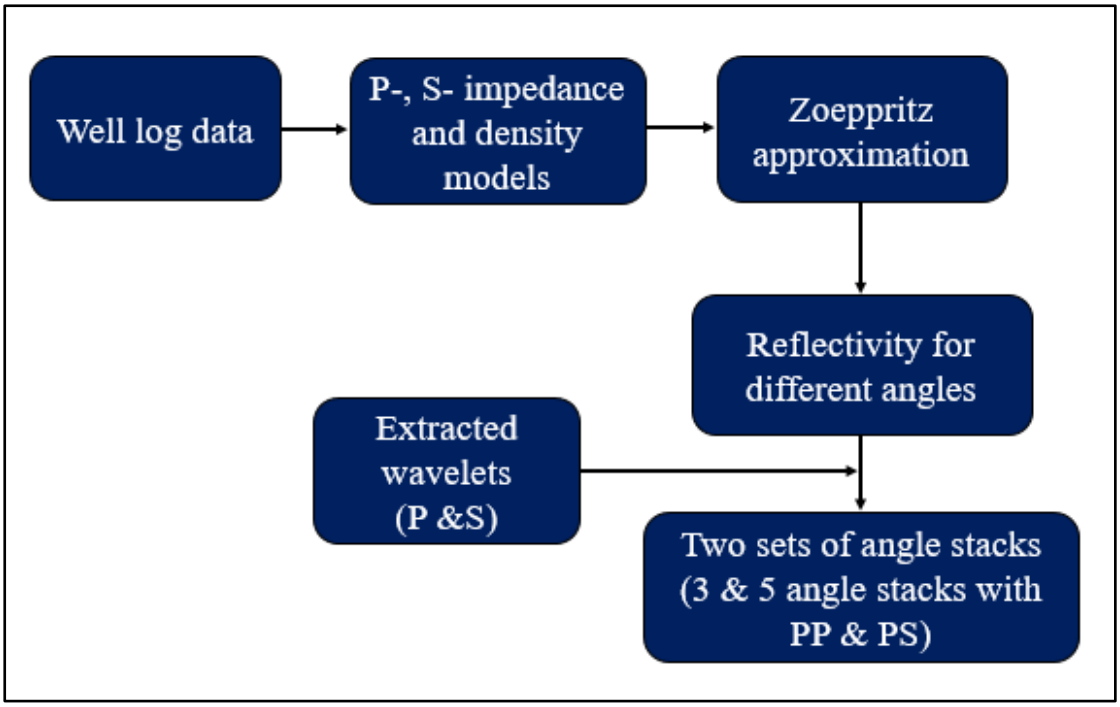

Figure 24: Schematic diagram showing workflow of 2D forward modelling, used to calculate post and pre-stack (angle stack) 2D synthetic traces.

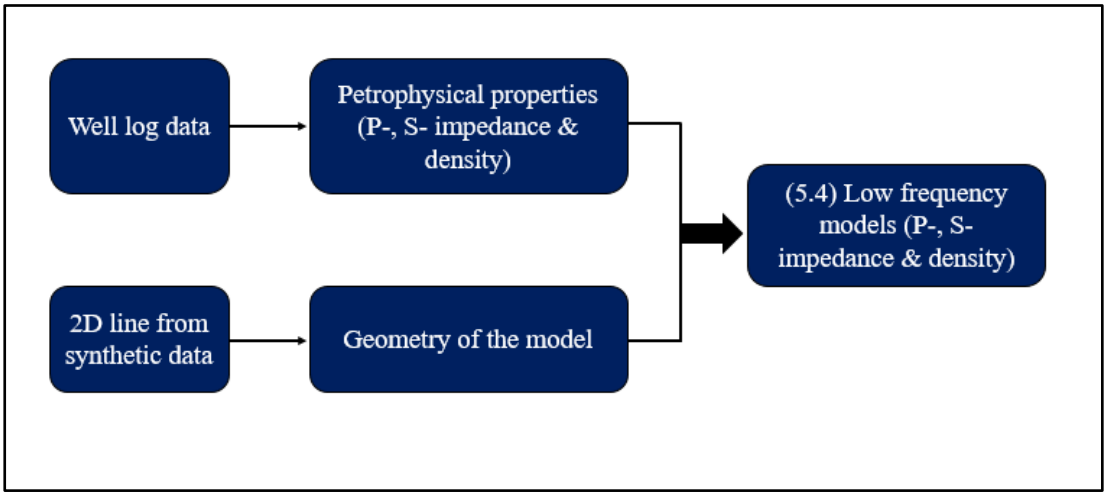

Figure 25: Shows the workflow to calculate the low frequency models of P-, S-impedance and density by using well log and 2D synthetic data

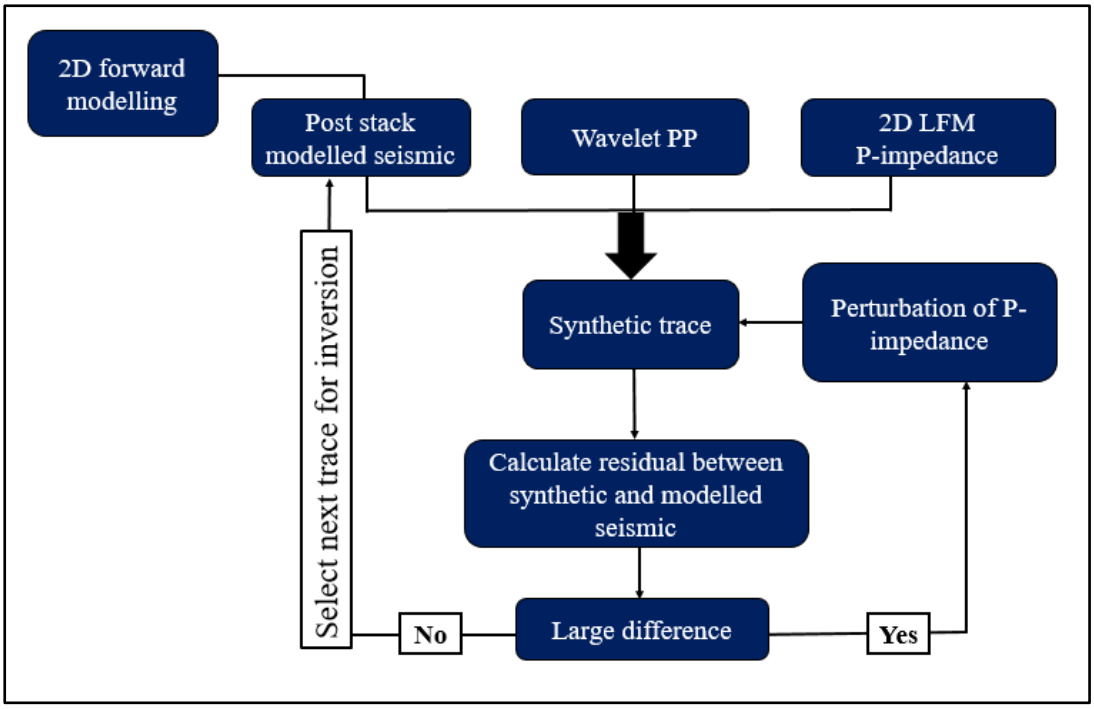

Figure 26: Workflow showing the process of post-stack seismic inversion, done by using zero angle stack trace. The output is residual and synthetic seismic section along the P-impedance cube

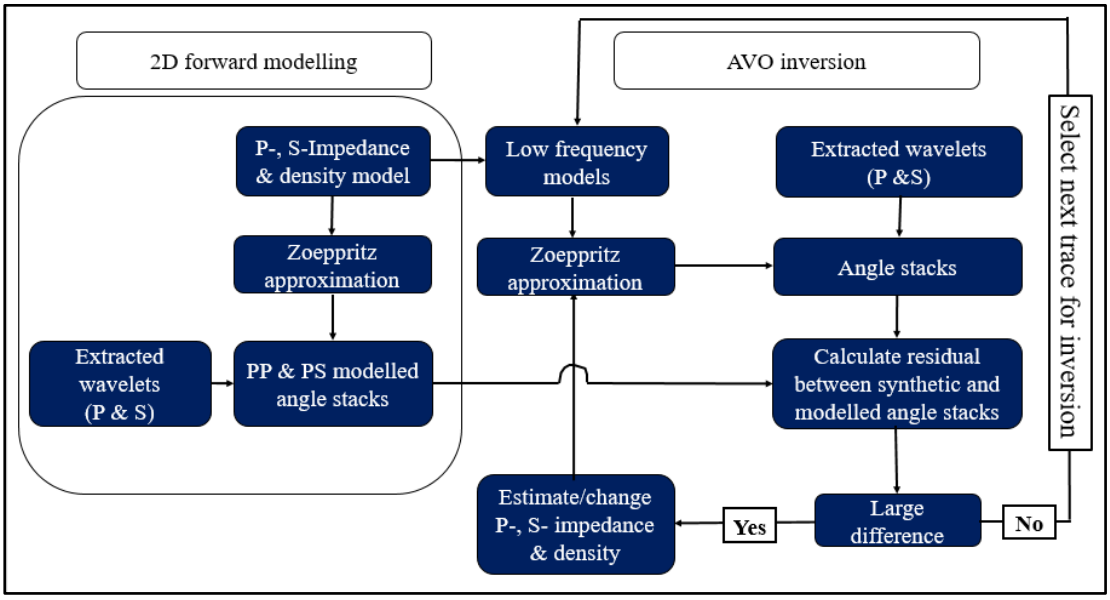

Figure 27: A schematic diagram of pre-stack simultaneous inversion workflow. This method includes both PP and PS seismic angle stacks as input with corresponded wavelet. The output is inverted P-, S- Impedance and density cubes.

Table 3: Inversion algorithms used for this thesis by using 2D synthetic data and their output parameters.

Inversion Algorithm		Inversion Results	Three & Five Angle Stacks data	Zero Angle Stack
Post-stack		P- Impedance		√
PP AVO	Aki & Richards	P-, S- Impedance & Density	√	
	Fatti	P- & S- Impedance	√	
PS AVO (Aki & Richards)		S- Impedance & Density	√	
PP & PS AVO (Aki & Richards)		P-, S- Impedance & Density	√	

5.2 WAVELET EXTRACTION AND SEISMIC TO WELL TIE

Seismic to well tie helps to relate the seismic horizons to stratigraphy through calculating the seismic response from the sonic and density log and compare it with seismic. The well 30/9-J-13H from the Oseberg Field data was taken and used for this purpose. This well contains compressional sonic log, density log and some hydrocarbon show, which makes it significant among all wells. The seismic to well tie was achieved by generating a synthetic trace from impedance log and ISIS wavelet. Figures 28, 29, 30 and 31 show the well section with the acoustic impedance log, wavelet, synthetic trace and the seismic sections for PP and PS angle stacks respectively. A bulk shift of 22ms was applied to the PP synthetic (Figure 29), while 45ms for PS synthetic (Figure 31).

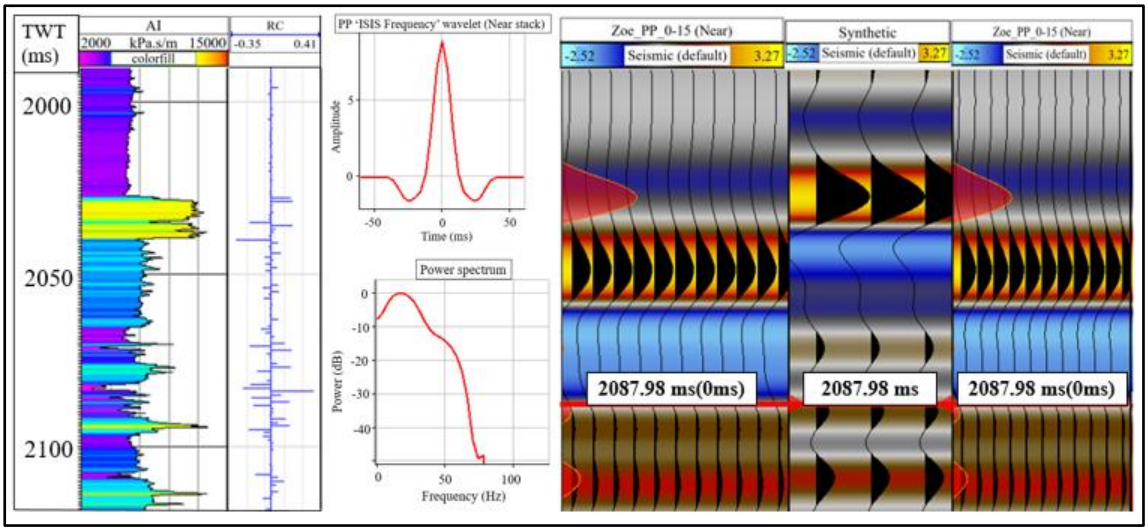

Figure 28: Seismic to well tie for PP (near) angle stack before applying the bulk shift to seismic section. On the left side, the acoustic impedance log is shown along with its reflectivity log. The used PP wavelet and its power spectrum is next to the reflectivity. The near angle stack is shown with the synthetic, which shows a large miss tie.

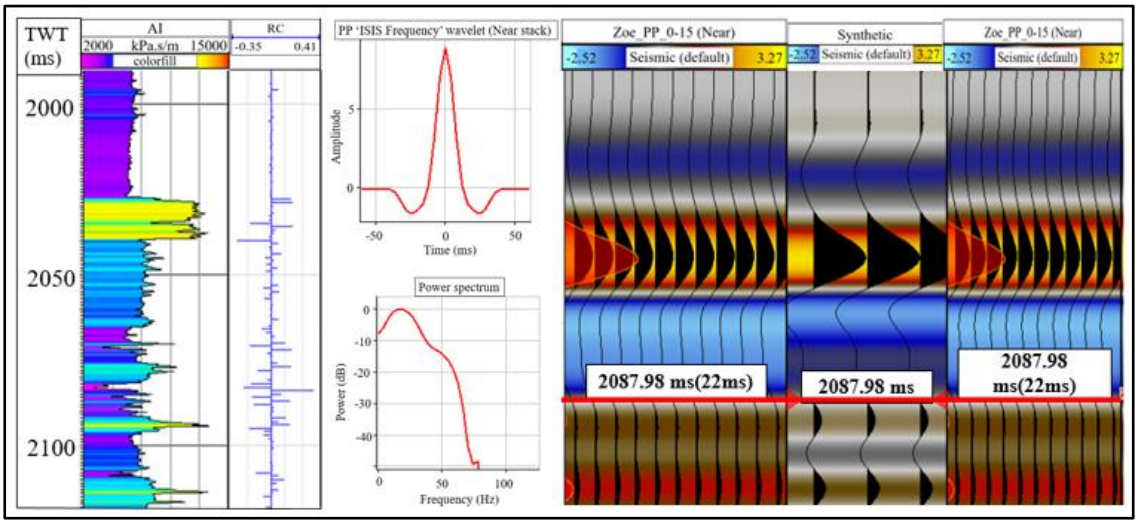

Figure 29: PP seismic section after the bulk shift of 22 ms is applied. The synthetic is matching with the near angle stack and the well log data.

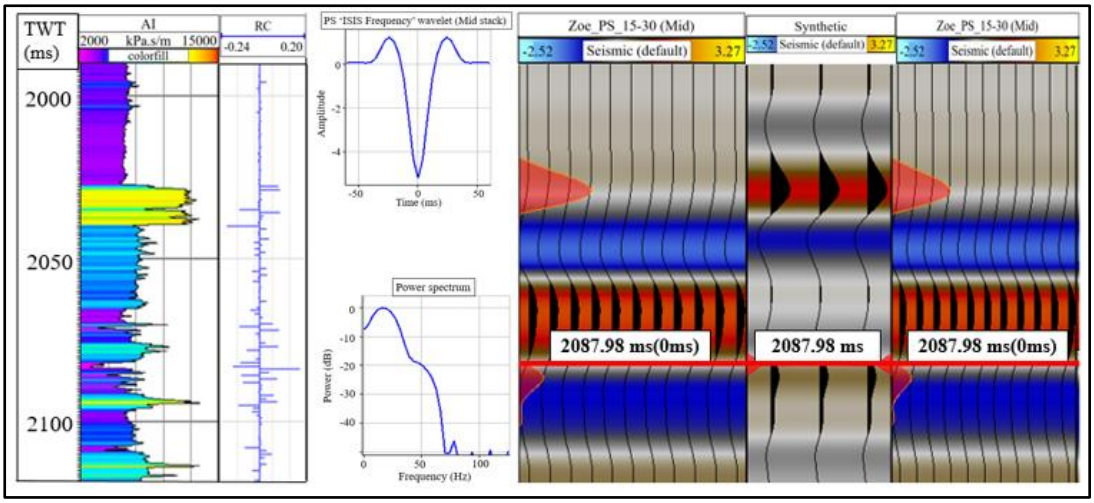

Figure 30: Seismic to well tie for PS (mid) angle stack before applying the bulk shift to seismic section. On the left side, the acoustic impedance log is shown along with its reflectivity. The inverted PS wavelet and its power spectrum is shown right beside the log. The mid angle stack is shown with synthetic, elaborating a miss tie with the seismic section.

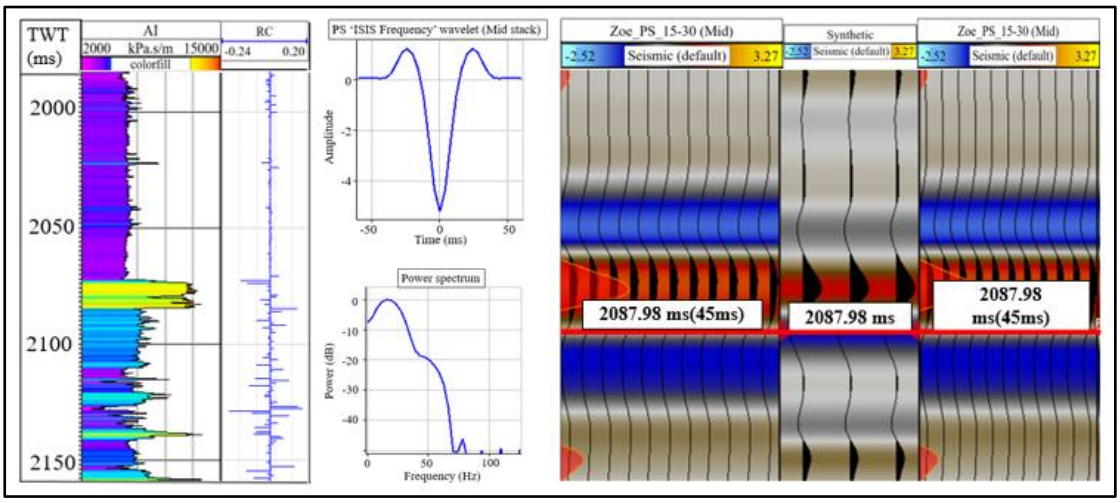

Figure 31: PS seismic section after the bulk shift of 45 ms is applied. The synthetic is matching with the mid angle stack and the well log data.

To achieve an accurate well tie, where the well log data matches the seismic amplitudes, a correctly extracted wavelet is necessary. The shape of a wavelet depends on its phase, frequency and amplitude spectrum. The algorithm used for the wavelet is *'Deterministic wavelet'* which allows to derive the wavelet from the seismic trace in the vicinity of the well path and the reflectivity. The wavelet was extracted within a

time window defined by the top and bottom of the reservoir, for PP and PS seismic in PP time domain. Two wavelets were calculated for PP and PS seismic angle stacks by using respective angles stacks from the Oseberg Field (Figures 32 & 33). The PP wavelet shown in Figure 32 is symmetric and centered at zero time, thus it followed the zero phase. However, the wavelet derived for PS seismic section has a phase shift of -180, as it gives the best seismic to well tie (Figure 31). This shows that the polarities of PP and PS seismic stacks are processed differently. The PP seismic stacks are processed according to SEG polarity, as mentioned in 3.1 section. However, the PS seismic stacks follow the European polarity system, where a 'hard kick' is blue in color and shows a negative peak. The wavelet contains a frequency range of ca 5-30Hz at -5dB (Figure 32 & 33 (b)).

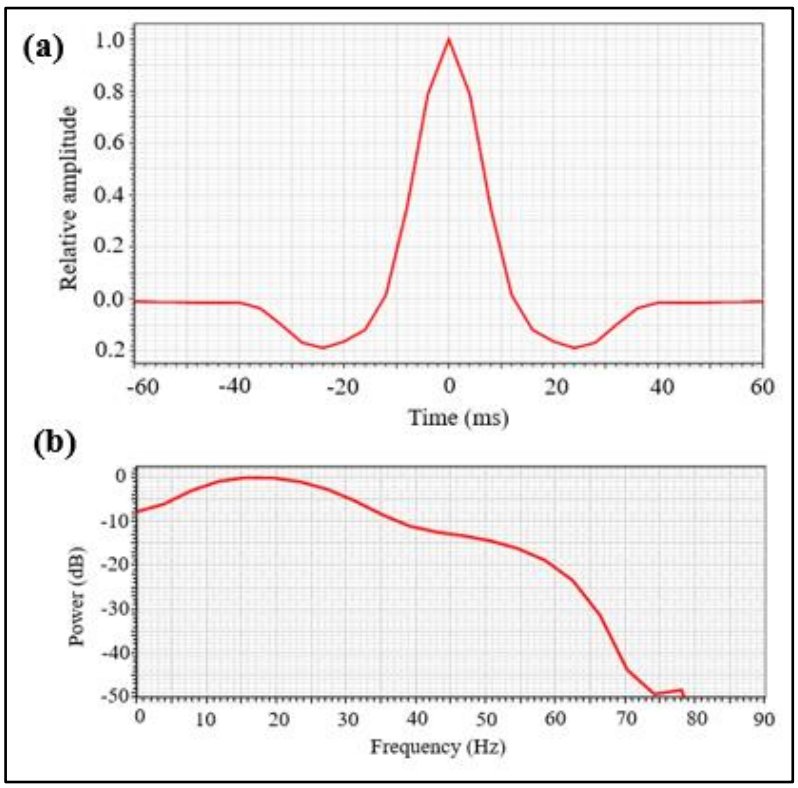

Figure 32: PP wavelet is extracted for near stack angle by using the respective seismic data from the Oseberg Field. (a) Shows the wavelet centered at zero phase while (b) is a power spectrum shows a frequency range of ca 5-30Hz at -5dB.

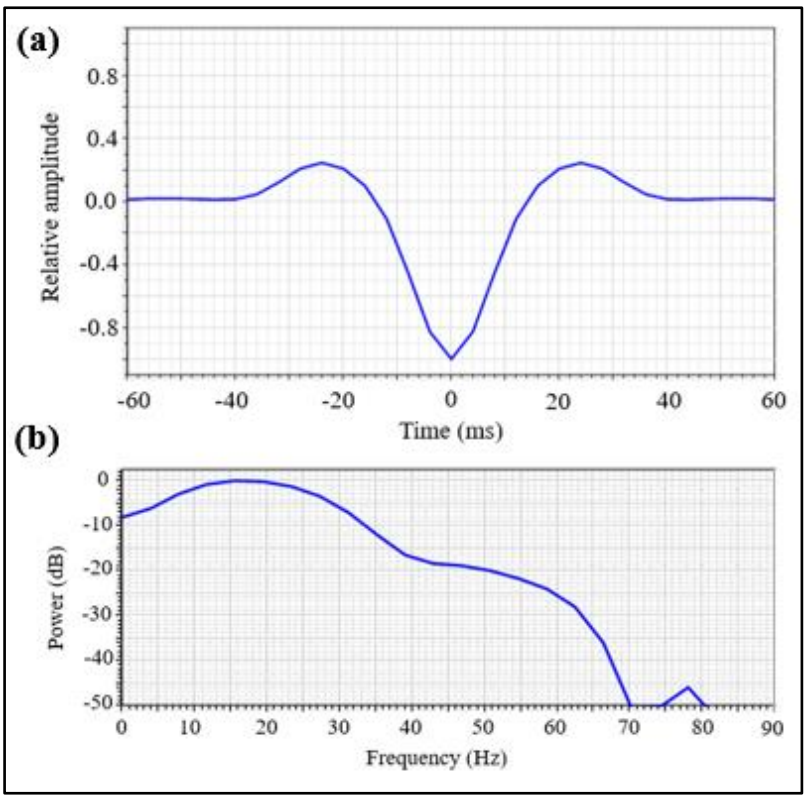

Figure 33: PS wavelet is extracted for near stack angle by using the respective seismic data from the Oseberg Field. (a) Shows the wavelet centered at -180 phase while (b) is a power spectrum shows a frequency range of ca 5-30Hz at -5dB.

5.3 2D FORWARD MODELLING

The *2D Forward Modelling* tool is used to create 2D synthetic data. This process uses the petrophysical properties derived from well log data, a wavelet and an algorithm based on Zoeppritz approximations to generate the synthetic data (Figure 24). A wedge-shaped model was created in which a reservoir is wedged between an overburden and under lying layers. The physical properties are taken from well log data. The logs needed are P-, S- sonic, P- and S- impedance and density. For this model the well 30/9-J 13H was used because only this well contains the measured shear sonic log.

Based on this well data 2D forward modelling generates the P-, S- impedance and density models estimated from the respective well logs. These impedance and density models are presented in Figure 34. The post-stack synthetic section was

calculated by using zero angle of incidence (Figure 35). The PP synthetic section is based on the P-impedance model. The Zoeppritz equation is needed to calculate the reflectivity for the PS stack and the PP angle stacks. Two sets of angles stacks were calculated, one is based on three angle ranges, the other based on five angle ranges. The angle ranges for the three angle stacks are: 0-15°, 15°-30° and 30-45° (Figures 36 & 37). The range for the five angle stacks is: 0-11°, 11-22°, 22-33°, 33-44° and 44-55° (Figures 38 & 39). The calculated reflectivity data is convolved with the corresponding wavelets (PP, PS, angle stacks) to get the synthetic 2D sections.

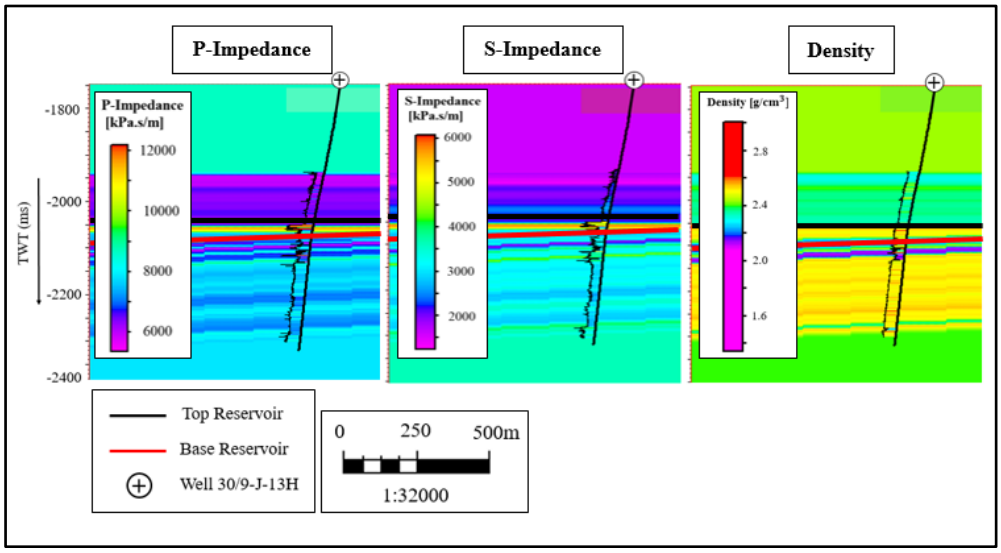

Figure 34: The 2D forward modelling calculates the P-, S- impedance and density sections as well. These parameters based on the respective well logs. Each parameter is shown with its corresponding well log. The top and base of the reservoir are marked for each parameter.

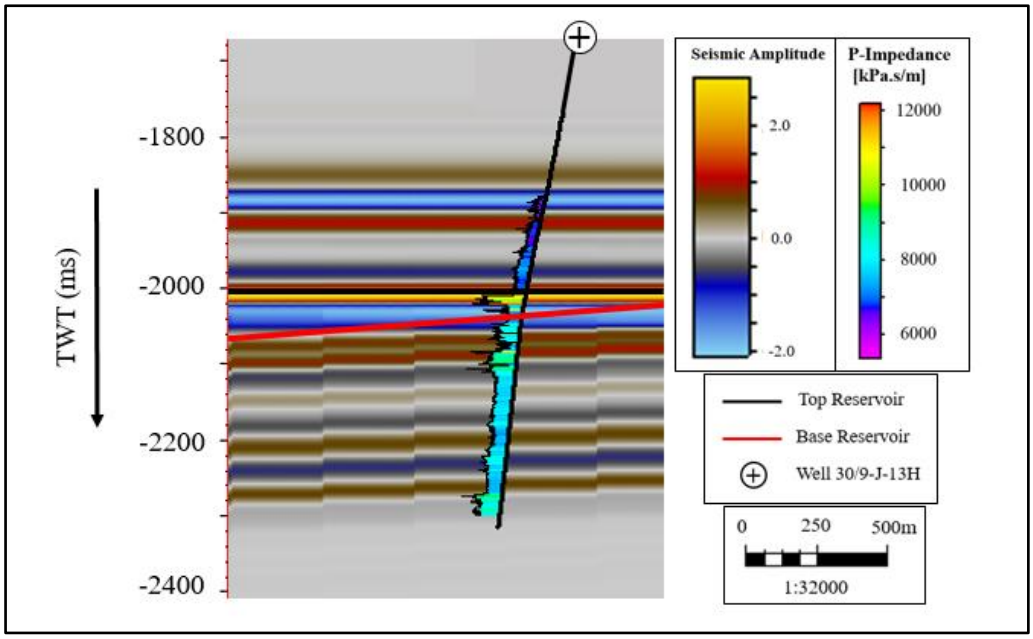

Figure 35:2D post-stack synthetic trace generated by 2D forward modelling. The well is showing the acoustic impedance log; the high acoustic impedance is corresponding to the high seismic amplitudes. The top and base of the wedged reservoir are marked.

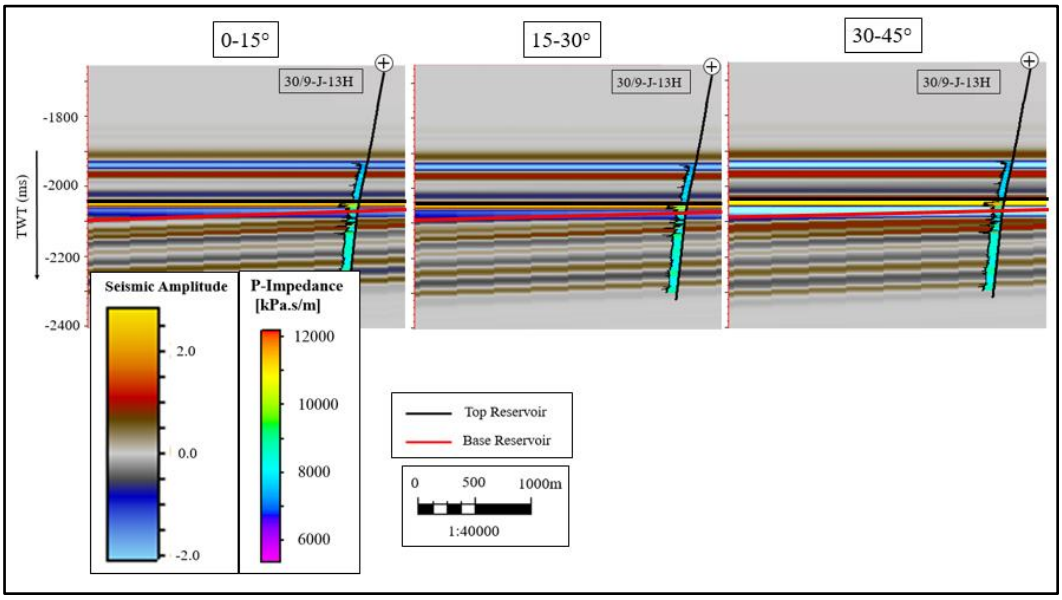

Figure 36: The three PP synthetic angle stacks 0-15°, 15-30° and 30-45° are shown in this figure, generated by using Zoeppritz approximations and PP ISIS Frequency wavelets. The well is showing the acoustic impedance log.

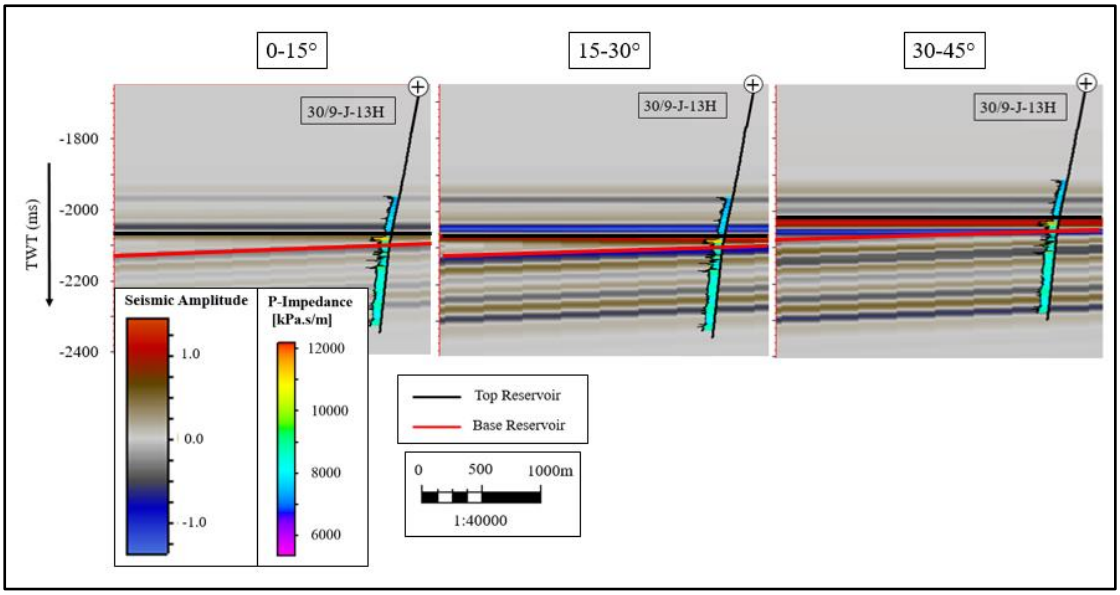

Figure 37: Three PS synthetic angle stacks 0-15°, 15-30° and 30-45° are calculated by using Zoeppritz approximations and the PS wavelets. The well is shown with its acoustic impedance log. The top and the base of the reservoir are marked.

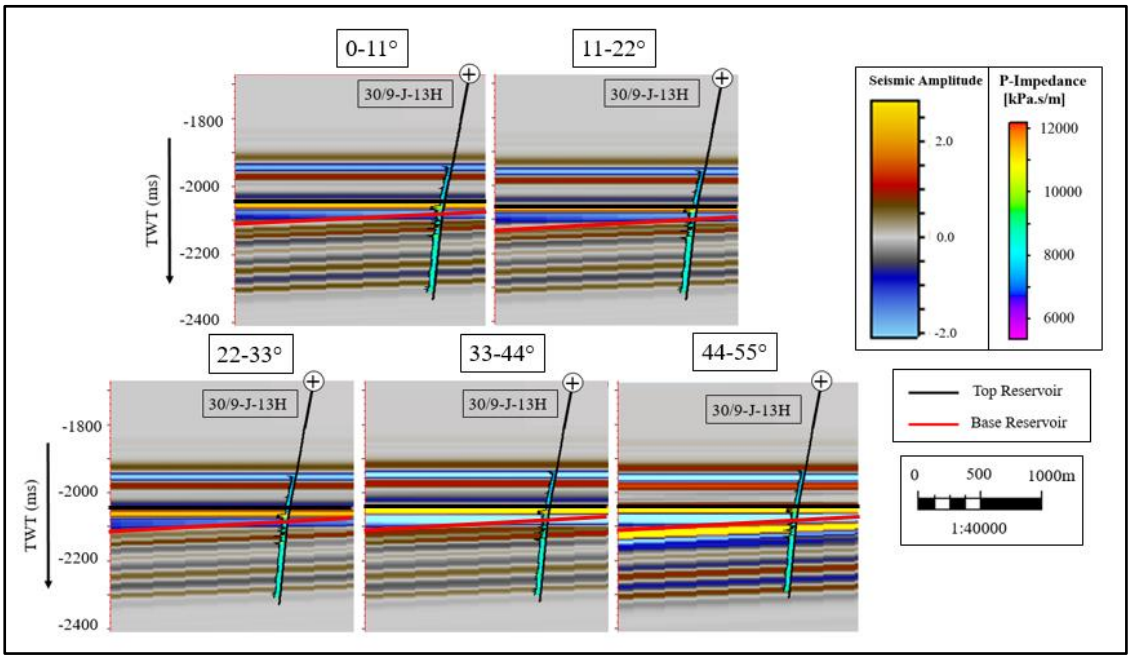

Figure 38: Five PP angle stacks set ranging 0-11°, 11-22°, 22-33°, 33-44° and 44-55° are shown in this figure. The angle stacks were calculated by using Zoeppritz approximation and PP wavelet.

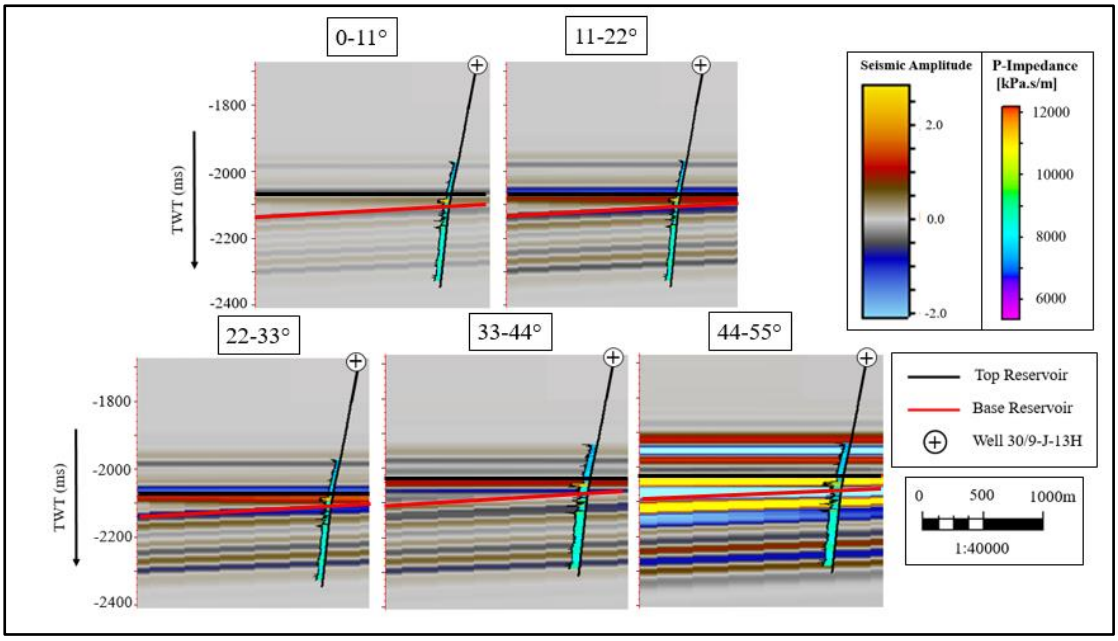

Figure 39: Five PS angle stacks set ranging 0-11°, 11-22°, 22-33°, 33-44° and 44-55° are shown. The angle stacks were calculated by using Zoeppritz approximation and PS wavelet.

5.4 LOW FREQUENCY MODEL (LFM)

The *Inversion property builder* tool is used to create low frequency models. The 2D synthetic seismic wedge model determines the geometry of a LFM. The acoustic, shear impedance and density log data is used to create the LFM and is extrapolated throughout the volume between the top and base of reservoir. A high cut filter of 8Hz is applied, which is the lowest frequency of the seismic frequency range. Consequently, the LFM only holds the frequencies below the seismic frequency spectrum. The LFMs generated for the P-, S- impedance and density (Figure 40). The LFMs shown in Figure 40 are used as initial models while operating the inversion and prevent the inversion to lose important information regarding low frequencies.

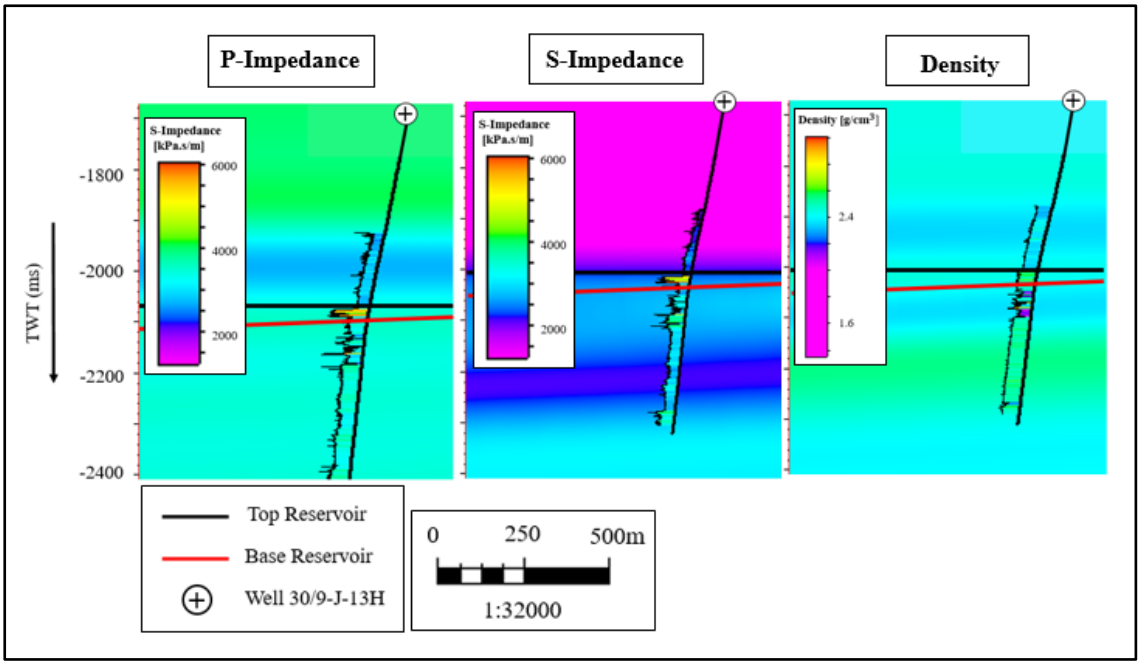

Figure 40: Three low frequency models, P-, S- impedance and density are shown along their respective well log. The seismic sections of LFMs are honoring the well logs very accurately. The increase in impedance and density is marked as the top of the reservoir.

5.5 POST-STACK INVERSION AND QC

Post-stack inversion was done by using *Simultaneous Inversion* process in *PETREL*. As already explained, the post-stack inversion works with stacked seismic data that can be represented by (migrated) zero-offset traces. In this thesis, for the synthetic data inversion, the zero offset traces were computed by using 2D forward modeling as explained in the schematic workflow in Figure 26. The reflectivity was calculated from the initial P-impedance model and convolved with the PP wavelet to achieve the synthetic stacks. The post-stack inversion gives the P-impedance as an output along with the synthetic and measured seismic trace. The residual is calculated between the 2D modelled seismic section and the synthetic section of the AVO inversion (Figure 41).

To check the reliability and quality of the post-stack inversion, a cross plot was made between the modelled and the calculated acoustic impedance. The correlation

coefficient is a statistical way to quantify the relationship of the post-stack inversion results with the P-impedance of the 2D model (Figure 42). The correlation coefficient of the post-stack inversion is 0.97. This elaborates that the post-stack inversion is a reliable means to calculate the P- impedance, provided the LFM is reliable. However, the post-stack data does not provide information about S-impedance and density.

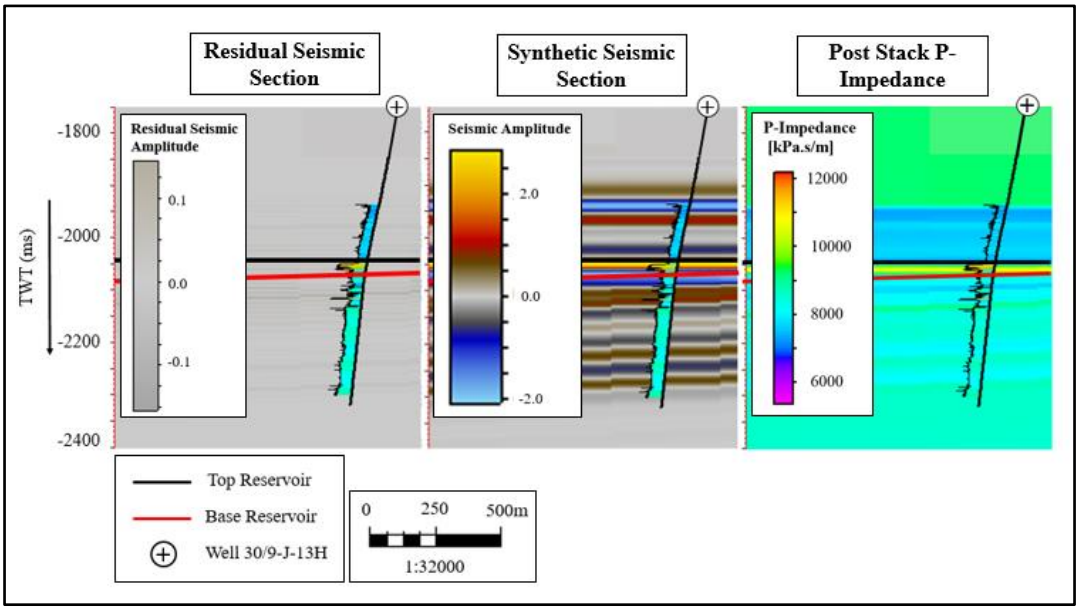

Figure 41: Post-stack seismic inversion results are shown here. The inversion results include residual, synthetic measured seismic sections and post-stack P-impedance. The inverted pos stack impedance shows a good match compared to the acoustic impedance log.

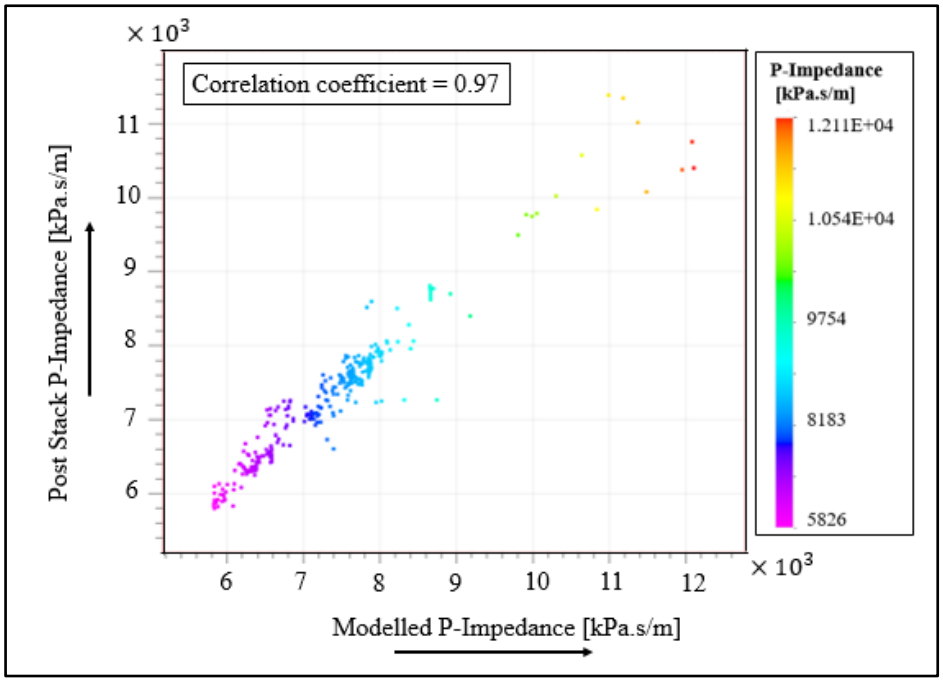

Figure 42: The QC of post-stack inversion is computed by cross plotting the modelled and post-stack inverted P-impedance. The correlation coefficient of 0.97 indicates that the post-stack inversion is reliable algorithm to achieve P-impedance.

5.6 PP AVO PRE-STACK INVERSION

PP AVO pre-stack simultaneous inversion involves the incident P-wave which reflects as a P-wave. In this thesis, two different Zoeppritz approximations were used for PP AVO inversion algorithm. These approximations are Aki and Richards (1980) and Fatti et al (1994). *Simultaneous inversion* process has the ability to use these algorithms and derive the PP angle reflectivity from perturbed P-, S- impedance and density models, and then convolve it with PP angle stack derived wavelet. It then compares the synthetic stacks with the seismic angle stacks. Both PP AVO inversions and their QC is discussed in following sections.

5.6.1 Aki and Richards approximation inversion algorithm and QC

The two sets of PP angle stacks described in 2D forward modelling, were used for inversion. Aki & Richards (1980) approximation which delivers acoustic and shear impedance (P-, S- impedance) and density sections, is used for both sets of angle stacks

sets. The resultant inverted impedance and density 2D lines for the three and five angle stacks are shown in Figures 43 and 44 respectively.

The cross plots are made between the modelled impedances and density and the those calculated from the AVO inversion based on the Aki and Richards approximation. The P- and S- impedance do not show much difference for the two sets of angle stacks, however the density shows a quite difference (Figures 43 & 44). Only the density cross plot is shown in this section (Figure 45) which shows a great difference in their correlation coefficients. The correlation coefficient would be 1.0 if the data is perfectly estimated. The difference between synthetic and measured PP angle stacks, for both sets of angles are shown in Figures 85 and 86 which are present in Appendix. The cross plots of P- and S- impedance for both angles stacks are elaborated in Figures 87 and 88 respectively in Appendix.

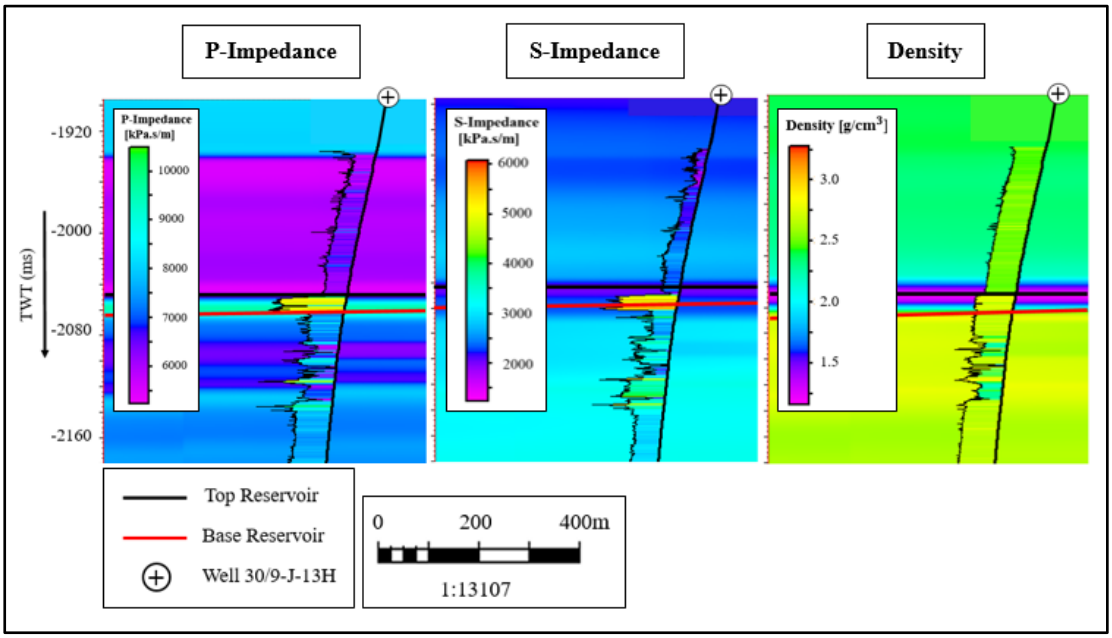

Figure 43: Aki and Richards inversion results for three angle stacks set. The P-, S-impedance and density sections are shown along corresponding well log. The well log data is honoring the inversion results.

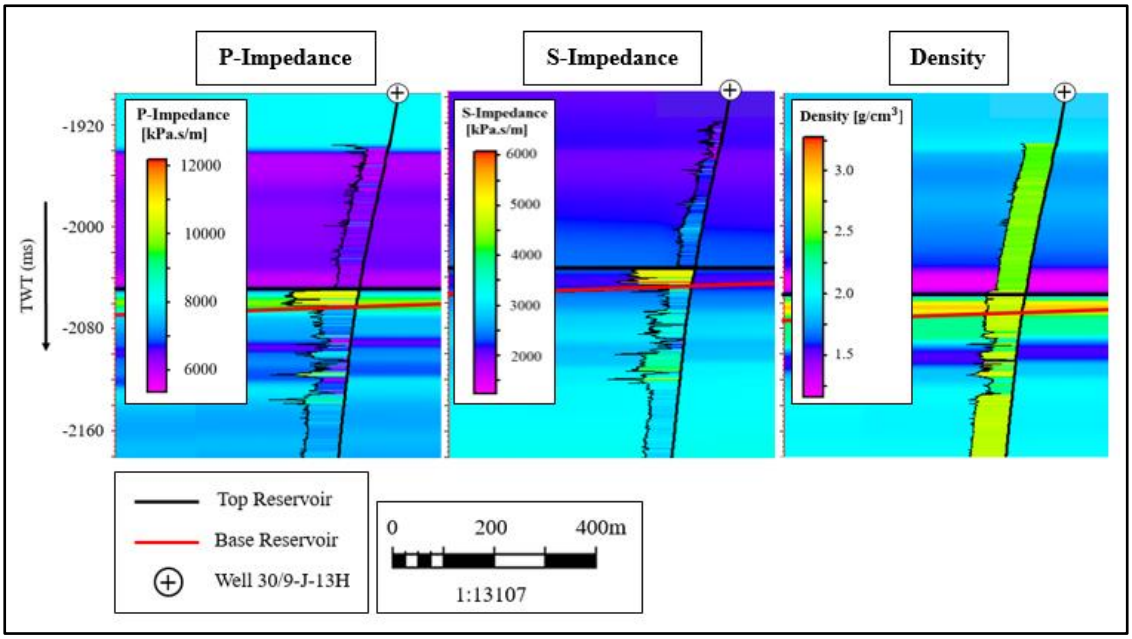

Figure 44: Aki and Richards inversion results for five angle stack set. The inversion results P-, S- impedance and density sections are honoring the corresponding well logs. This is an indication of a reliable inversion. However, the density section is quite different from the density based on the three sets of angle stacks.

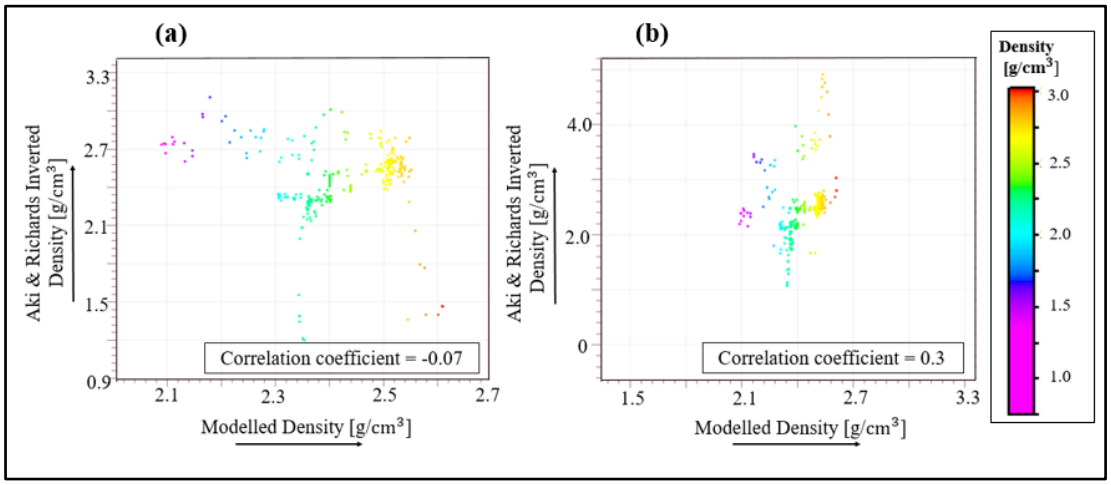

Figure 45: QC Cross plots of Aki and Richards inversion results. (a) Cross plot between modelled and Aki and Richards inverted density for three angle stacks of set showing a correlation coefficient of -0.07. (b) Cross plot for the same parameters for five angle stacks set. This shows a correlation coefficient of 0.3, which shows that long range of angles give a bit better results for density.

5.6.2 Fatti et al. approximation inversion algorithm and QC

Fatti et al. (1994) approximation which delivers the acoustic and shear impedance as inverted output is also used in this thesis. Again, the inversion algorithm is applied for both sets of angle stacks (Figures 46 & 47). The cross plots are made between modelled and Fatti et al. inverted P- and S- impedance and shown in Figures 48 and 49 respectively along with their correlation coefficients. The correlation coefficients for the P-inverted differ by 6% and for the S-inversion by 15% for the two angle stack sets, in favor of the five angles stacks set. The difference between synthetic and measured PP angle stacks, for both angle stacks sets are explained in Figures 89 and 90 which are documented in Appendix.

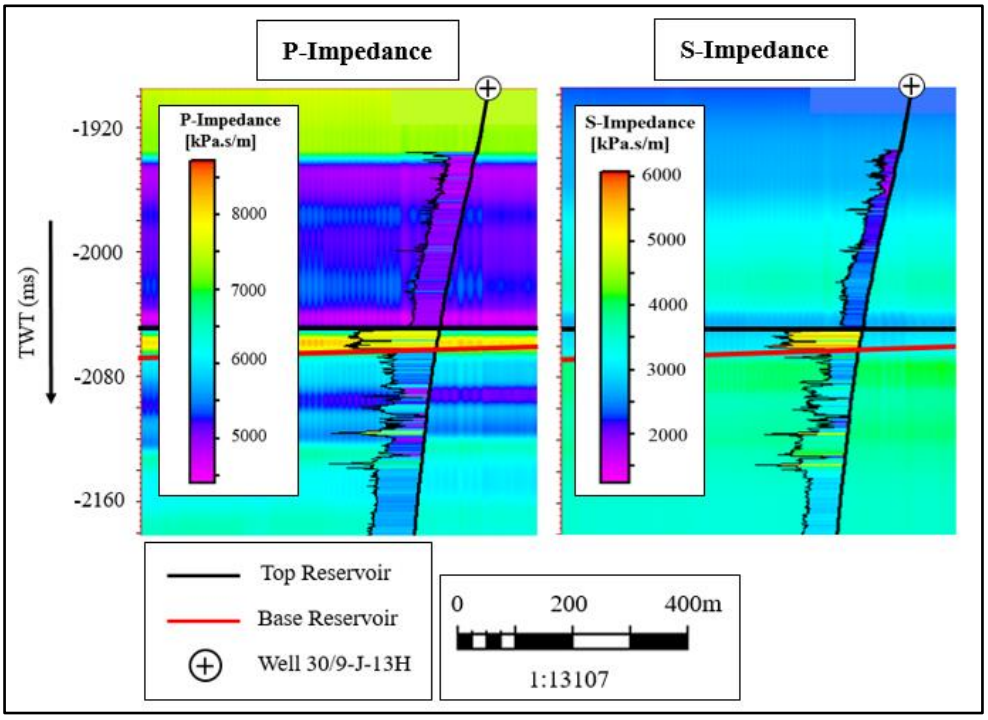

Figure 46: Inversion results of Fatti et al. algorithm applied to the three sets of angle stacks. (a) Shows an inverted P-impedance section with its well log. Both are showing high impedance at the top of the reservoir. (b) Shows an inverted S-impedance section along with well log. S-impedance is not honoring the well log very well, which shows the unreliability of inversion for S-impedance.

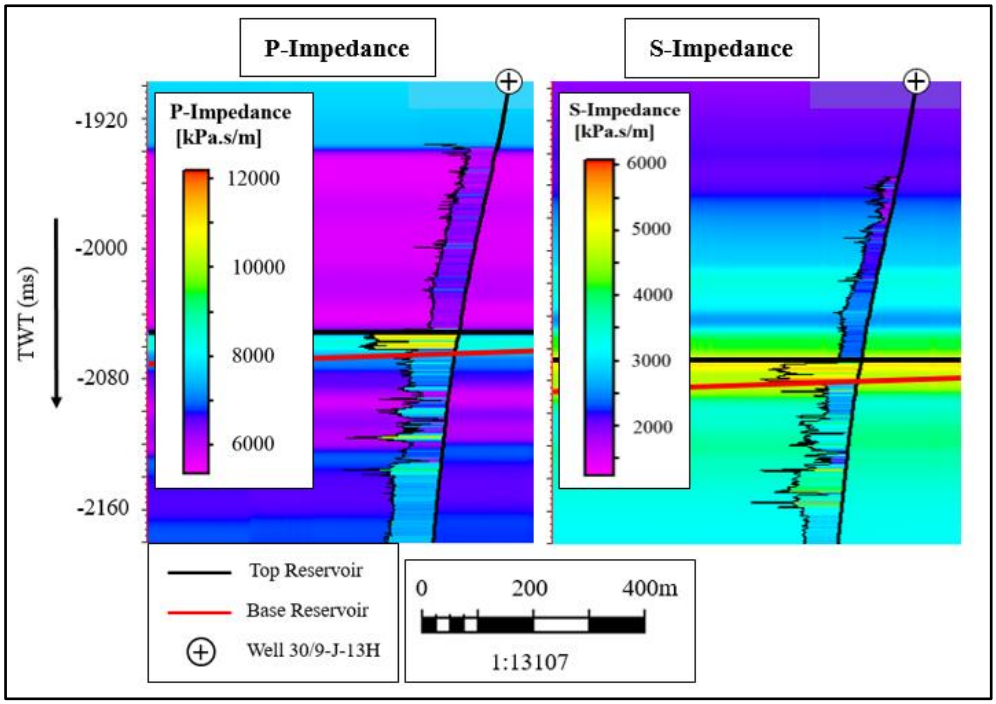

Figure 47: Inversion results of Fatti et al. algorithm applied to the five sets of angle stacks. (a) Shows an inverted P-impedance section along its well log. Both are showing high impedance at the top of the reservoir. (b) Shows an inverted S-impedance section with the respective well log. Both well log and inverted S-impedance show high impedance at top of reservoir, depicting a reliable inversion results for S-impedance as well.

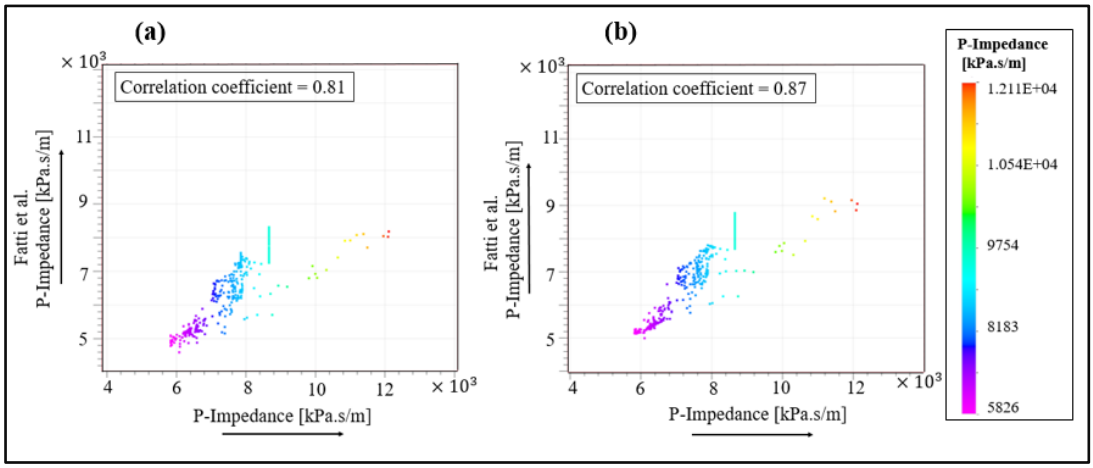

Figure 48: QC Cross plots of Fatti et al. inversion results. (a) Cross plot between modelled and Fatti et al. inverted P-impedance based on three angle stacks shows a correlation coefficient of 0.81. (b) Is a cross plot for the same parameters based on five angle stacks. This shows a correlation coefficient of 0.87.

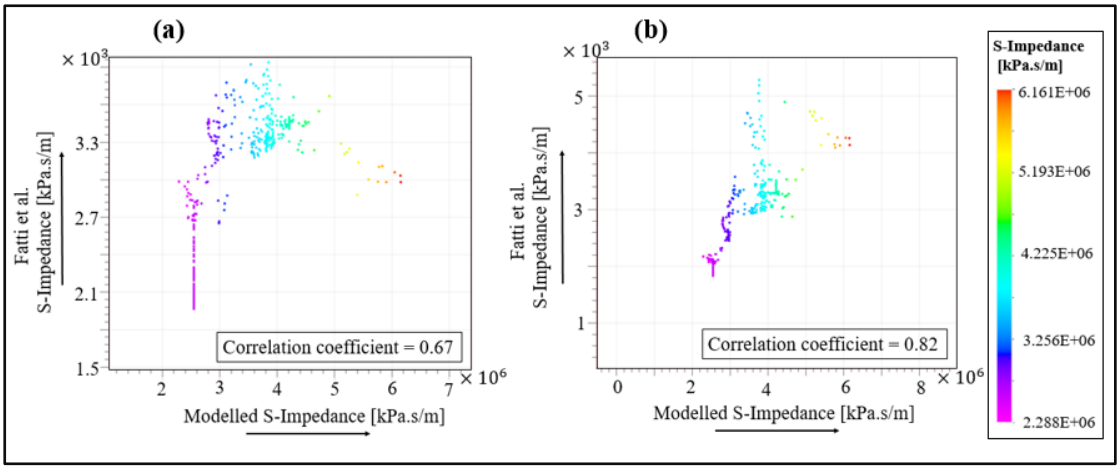

Figure 49: QC Cross plots of Fatti et al. inversion results. (a) Cross plot between modelled and Fatti et al. inverted S-impedance based on three angle stacks shows a correlation coefficient of 0.67. (b) Is a cross plot for the same parameters based on five angle stacks. This shows a correlation coefficient of 0.82. The correlation difference of 0.15 between the two angle stack coefficients show that five angle stacks set gives a more reliable S-impedance.

5.7 PS AVO PRE-STACK INVERSION AND QC

PS AVO pre-stack simultaneous inversion involves the incident P-wave which reflects as S-wave from an interface. The only inversion algorithm available for PS seismic angle stack inversion is Aki and Richards approximation. This algorithm delivers S-impedance and density as an output but does not calculate P-impedance. The inverted 2D lines of S-impedance and density for three and five angle stacks sets are shown in Figures 50 and 51 respectively. The QC of S- impedance and density from PS inversion for both angle stacks is shown in Figure 52 and 53 respectively. The difference between synthetic and measured PS angle stacks for both sets of angle stacks are explained in Figure 91 and 92, which are shown in Appendix.

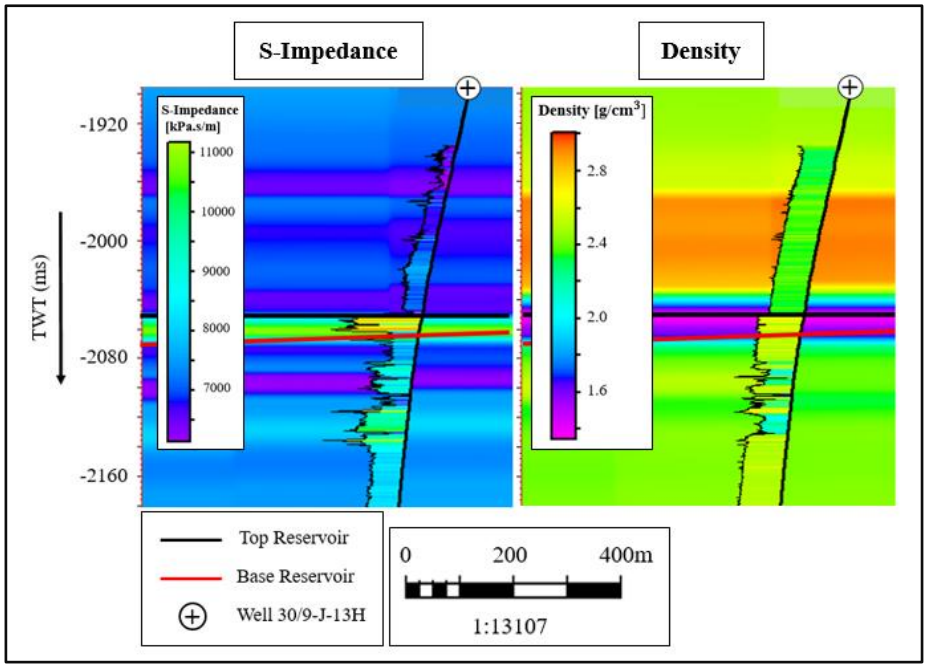

Figure 50: PS inversion results for three angle stacks are shown. S- impedance and density are shown with their respective shear impedance and density logs. Inverted S-impedance is fairly honoring the log data while the inverted density is not responding in reliable way.

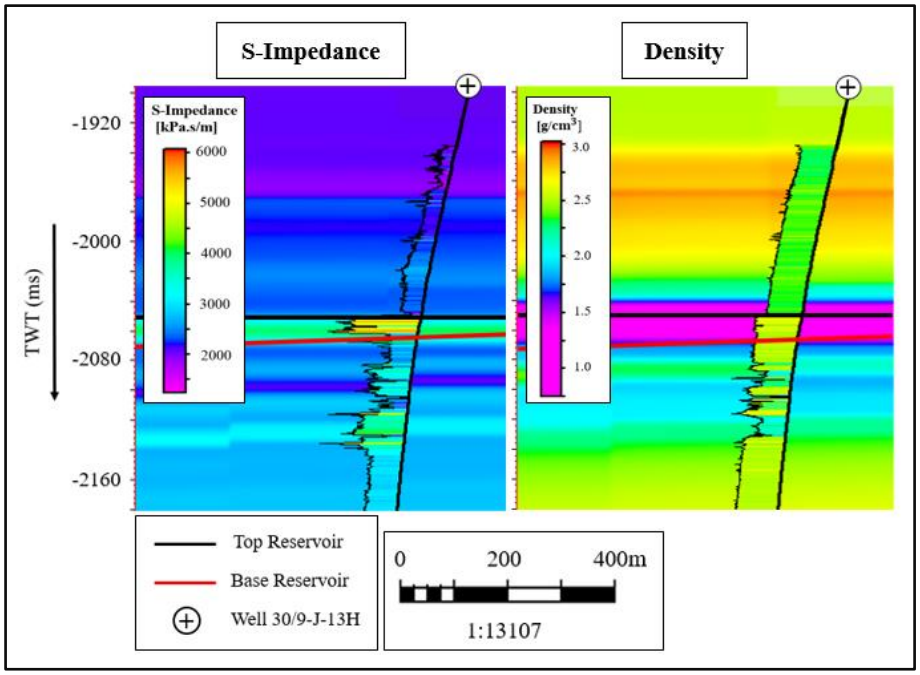

Figure 51: PS inversion results for five angle stacks are shown. S- impedance and density are shown along with their respective shear impedance and density logs. Inverted S-impedance is correlating the log data while inverted density does not illustrate any improvements.

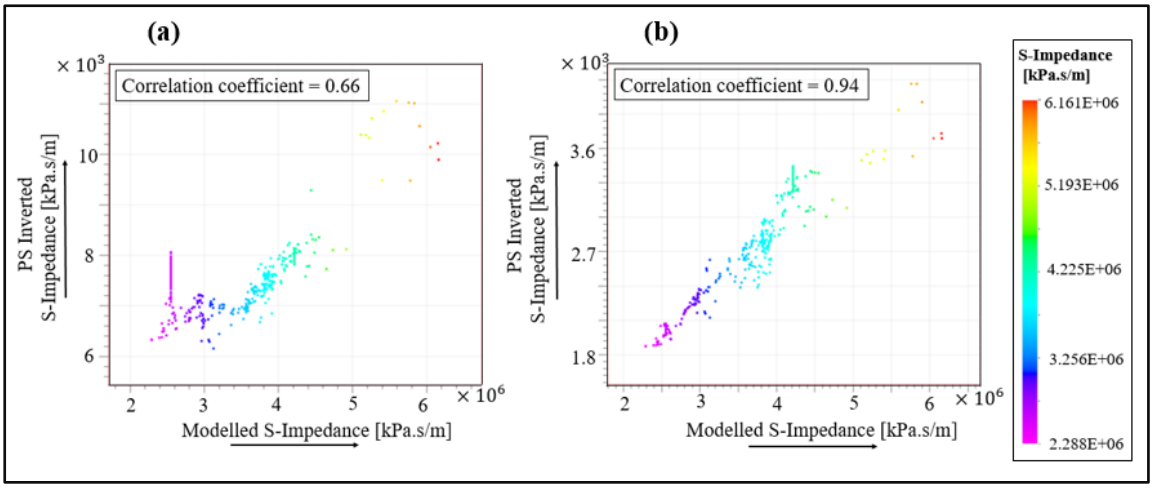

Figure 52: QC cross plots of PS AVO inversion results. (a) Cross plot between modelled and inverted S-impedance based on three angle stacks gives a correlation coefficient of 0.66 while (b) Is a cross plot of same parameters based on five angle stacks with a correlation coefficient of 0.94. The correlation coefficient difference of 0.28 between the both angle stacks shows that five angle stacks set gives a more reliable S-impedance.

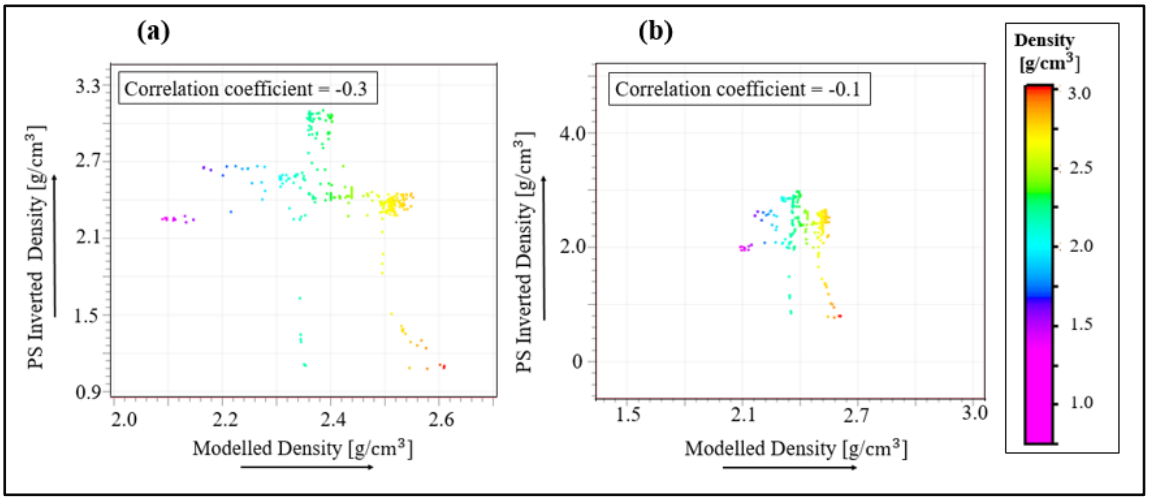

Figure 53: QC cross plots of density based on PS AVO inversion results. (a) Cross plot between modelled and inverted density based on three angle stacks gives a correlation coefficient of -0.3 while (b) Is a cross plot of same parameters based on five angle stacks with a correlation coefficient of -0.1. Both sets of angle stacks do not deliver a reliable density section.

5.8 JOINT PP & PS PRE-STACK INVERSION AND QC

Joint PP & PS pre-stack inversion involves both PP & PS angle stacks. The algorithm that was available for joint inversion is Aki and Richards approximations.

Joint inversion delivers the inverted P-, S- impedance and density cubes. The inversion was achieved by using both three and five angle stacks sets, LFMs and the respective wavelets. The inverted P-, S- impedance and density 2D lines are shown in Figures 54 and 55 for both angle stacks sets respectively. The P- and S-impedance do not show a large difference for both angle stacks. However, for the density 2D line, there is a slight difference around the top reservoir. The difference between synthetic and measured PP and PS angle stacks are documented in Figures 93, 94, 95 and 96 which are present in Appendix.

The QC of joint inversion is done by cross plotting the modelled and inverted parameters. Only the density cross plot is shown here (Figure 56), while the P- and S-impedance for both sets of angle stacks are shown in Appendix in Figure 97 and 98. The inverted density shows a slightly different behavior from three angles to five angle stacks; however, the correlation difference is still about 5%, which demonstrates that even with a long range of angle stacks joint inversion is not delivering reliable density cube.

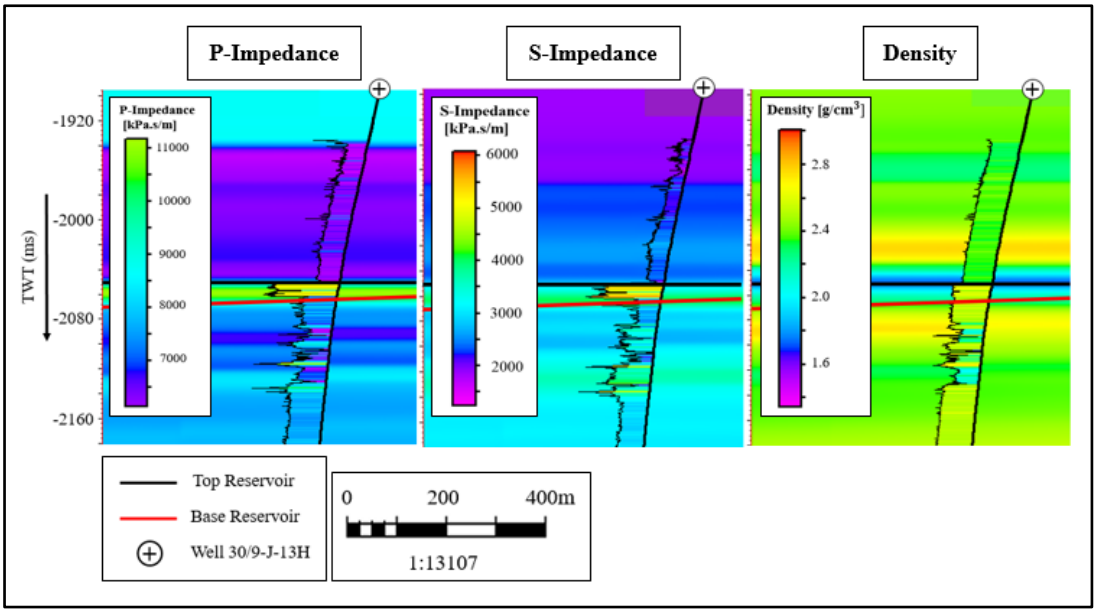

Figure 54: Joint PP & PSAVO inversion results for three angle stacks, comprising P-, S- impedance and density sections. The inversion results are shown along with their corresponding well logs. P- and S-impedance inversions are following the log data, while the inverted density does not show a good match with the density log.

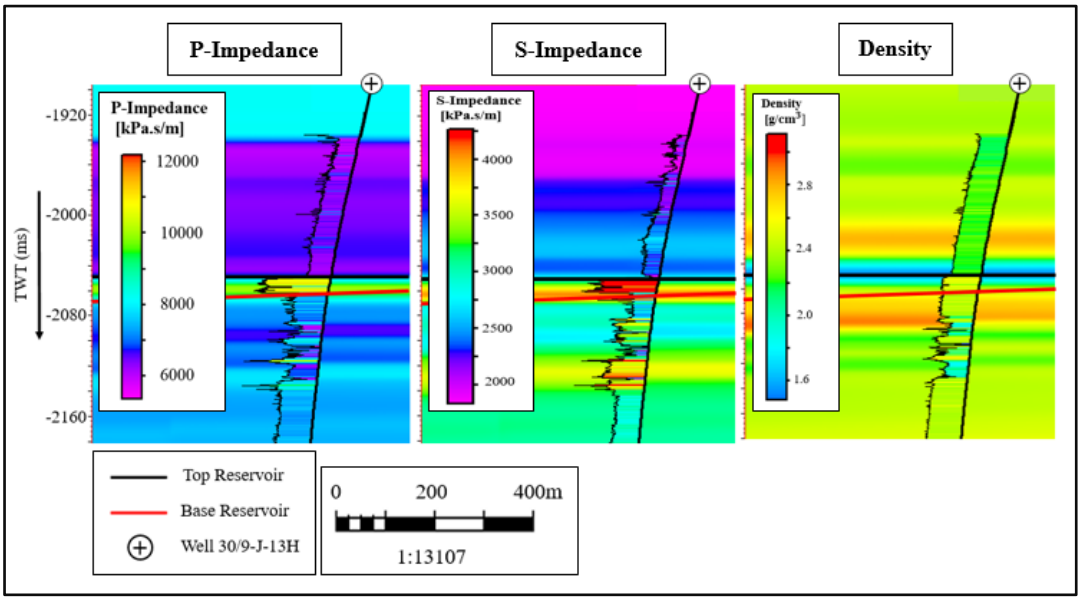

Figure 55:Joint PP & PSAVO inversion results based on the five angle stacks, encompassing P-, S- impedance and density sections. The inversion results are shown along their corresponding well logs. P- and S-impedance inversions are following the log data. However, the inverted density showing a closer match to the density log than three angle stacks.

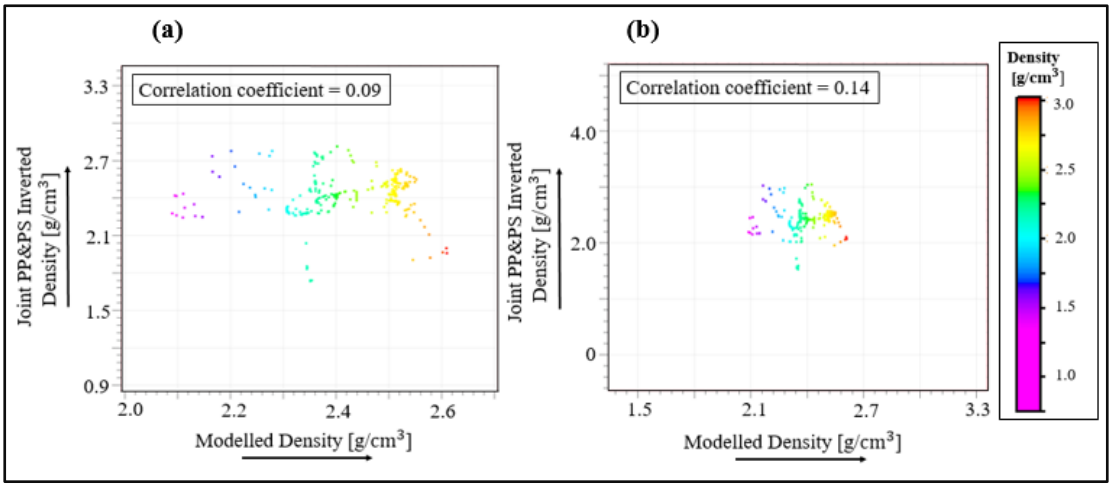

Figure 56: QC cross plot of density from modelled and PP and PS inversion results. (a) Is the cross plot for three angle stacks showing a coefficient of 0.09 while (b) is for five angle stacks which has a coefficient of 0.14.

5.9 BRIEF COMPARISON OF INVERSION RESULTS

The cross plots of inversion results deliver the correlation coefficients, which is an efficient and quick way to find out the reliable inversion method. Two bar graphs were made by using these correlation coefficients, calculated by different inversion algorithms (Figures 57 & 58). These bar graph show the comparison of all four inversion methods done by using three and five angle stacks sets. The graphs show that joint PP & PS inversion algorithm is working better for all inversion results P-, S-impedance and density. Also, there is no large difference between the inversion results of the three and five angle stacks sets. The only largest difference is shown by the density sections. The density section derived from the PP AVO Aki and Richards inversion has a 37% correlation coefficient in favor of the five angle stacks.

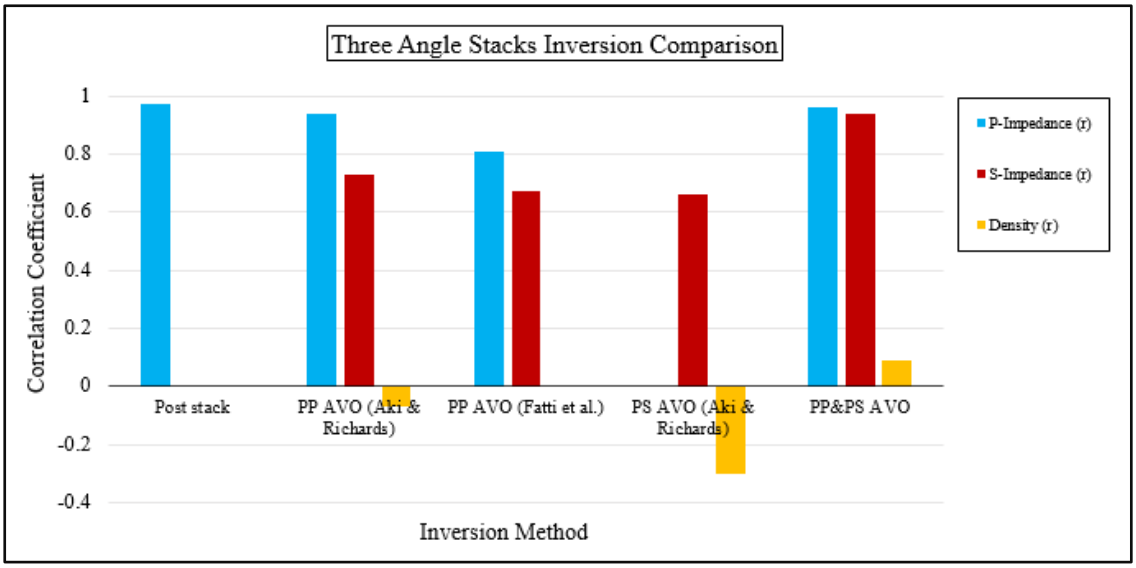

Figure 57:Comparison of inversion algorithm for three angle stacks. For the parameters P-, S-impedance joint PP & PS inversion is delivering a most reliable result. The density result does not correlate with the density model and hence is unreliable.

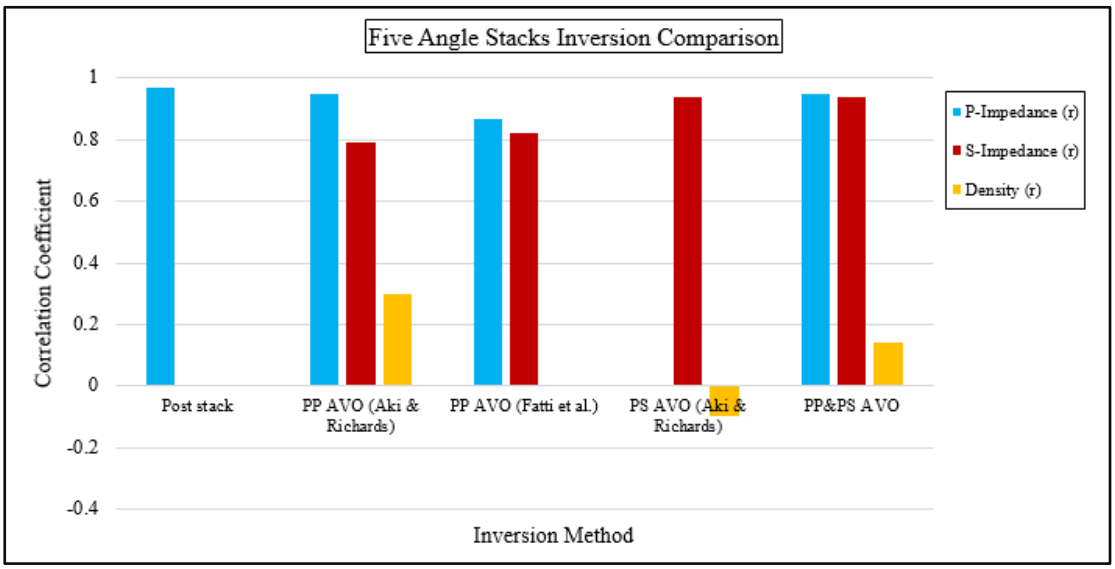

Figure 58: Comparison of inversion algorithm for five angle stacks. For the parameters P-, S-impedance joint PP & PS inversion is delivering the most reliable result. The density parameters of all algorithm show a poor correlation and hence cannot be regarded as reliable.

6. JOINT PP & PS SIMULTANEOUS INVERSION ON THE OSEBERG FIELD AND LITHOLOGY PREDICTION

The different inversion methods discussed in the previous sections explain that the joint PP & PS inversion gives a reliable result in term of P- and S- impedance. However, it does not provide a reliable density section. It is also discussed in the previous chapter that the inversion algorithm operates better for several angle stacks covering a large angle range. Because of its reliable results the joint inversion method was applied to the Oseberg Field. The lithology prediction was based on these inversion results. In this chapter the joint inversion along with the lithology cube, achieved from the Oseberg Field are discussed.

6.1 PROPOSED WORKFLOW FOR OSEBERG FIELD DATA

The workflow for joint inversion on the Oseberg Field data is quite similar to the synthetic joint inversion workflow. Figure 59 shows a schematic diagram of the joint PP & PS inversion workflow. The seismic and well log data has already been discussed in chapter 3. The next step after getting reliable seismic inversion results, is to predict the lithology distribution of the reservoir zone for the Oseberg Field. A work flow is proposed for mapping the lithology classes (Figure 60).

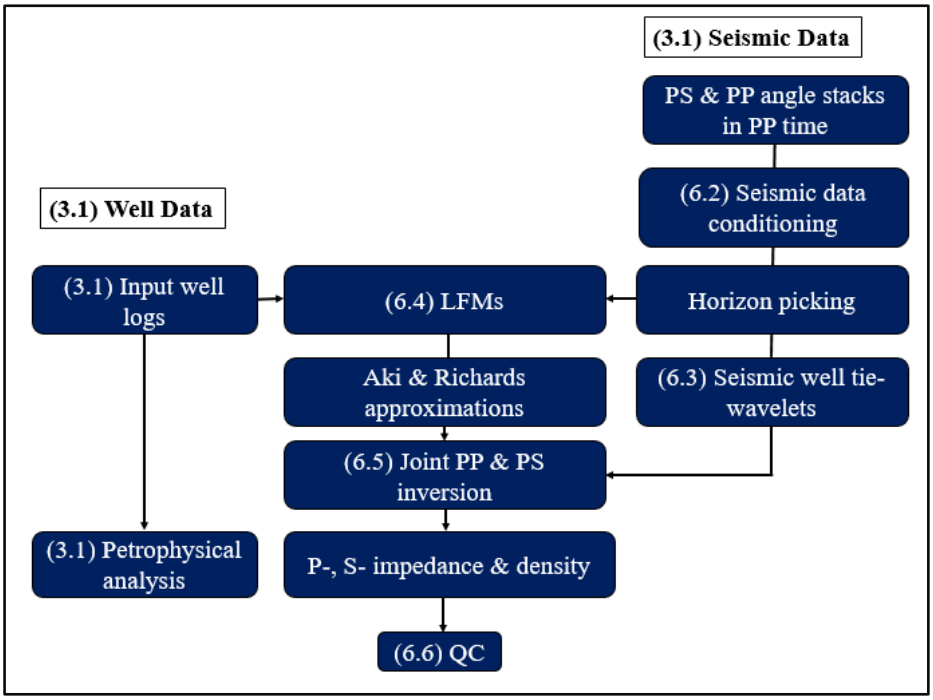

Figure 59: A schematic diagram to show the workflow for joint PP & PS AVO inversion for the Oseberg Field.

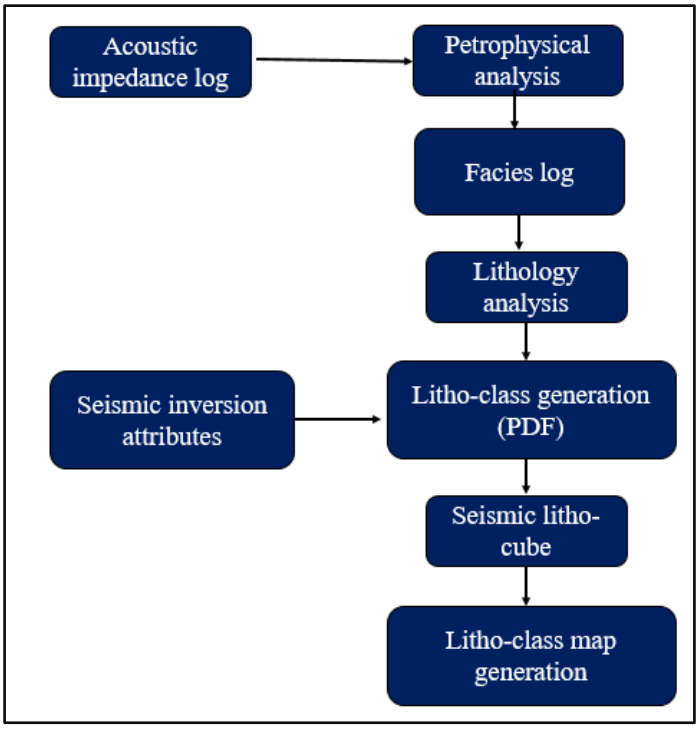

Figure 60: A diagram illustrating the workflow for seismic lithology cube, derived from the well log data and seismic inversion attributes. The seismic litho-cube is used to map the reservoir of the Oseberg Field.

6.2 SEISMIC DATA CONDITIONING

Seismic data conditioning is an important step to improve quantitative seismic interpretation or reservoir characterization. For this thesis the data is delivered by Statoil and most of data conditioning has already been applied. However, the data was thoroughly checked and only the following data conditioning processes were applied.

6.2.1 Area of interest and seismic horizons

The seismic cube was given for this project comprises a large area. To make the inversion efficient, the seismic cube was cropped down to the area of interest, which is between the top and base horizon of the reservoir. The Shetland Group is the top at a depth of ca -2030 ms while the base is Drake Formation at a depth of ca -2110 ms (Figure 61). The important reservoir of the Oseberg Field, the Brent Group lies between this depth of 80 ms. The seismic cube was cropped according to this precise depth (Figure 61).

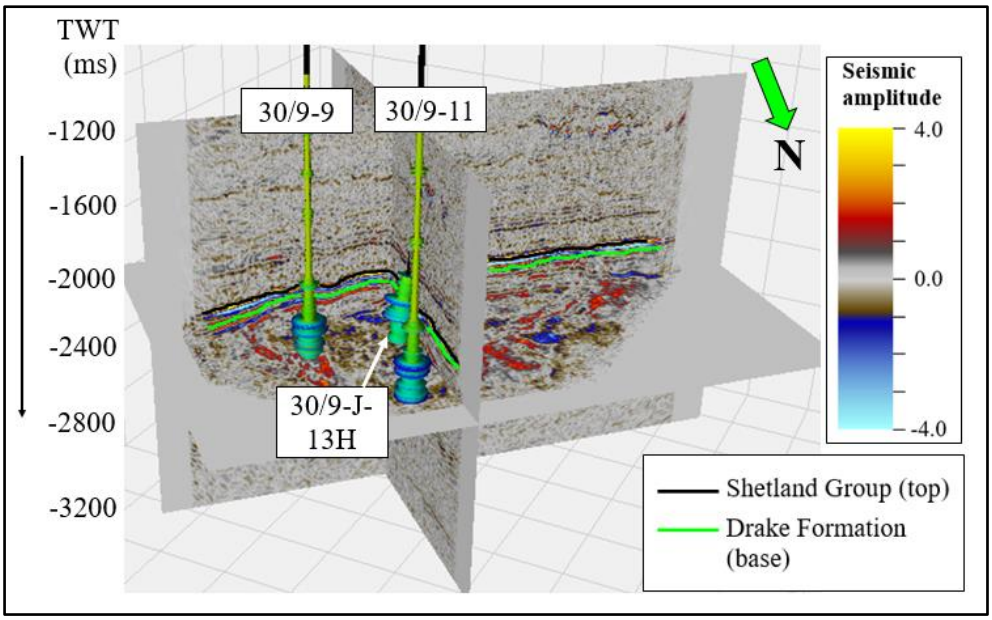

Figure 61: Seismic cube, cropped to an area of interest, is shown along with three wells and the top and base reservoir horizons.

6.2.2 Time alignment

The pre-stack seismic data consists of PP and PS angle stacks which range 0-15°, 15-30°, 30-45°. In this thesis they have been referred as near, mid and far angle stacks respectively. The increase in angle effects the arrival time, with larger angle of incidence, the arrival time starts to delay for far offsets or angles. The *time alignment* technique from *seismic data conditioning (SDC)* tool was used to remove this effect on the far angle stacks. The misalignment of the angle stacks was corrected. Figures 62 and 63 show time alignment for near and far stacks angles for PP seismic sections respectively. Similarly, time alignment was done for PS seismic sections however it is not demonstrated here.

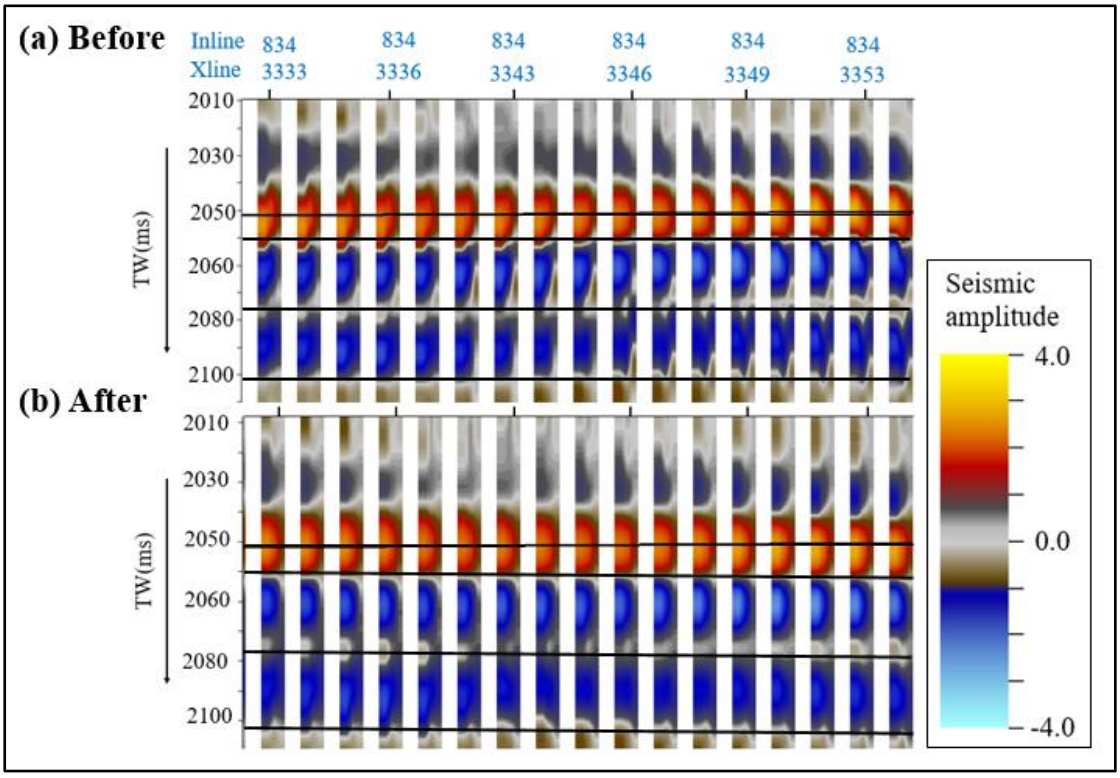

Figure 62: Time alignment for near angle stacks for PP seismic section. (a) Shows the misalignment of the seismic trace marked by the black lines (b) The traces are aligned.

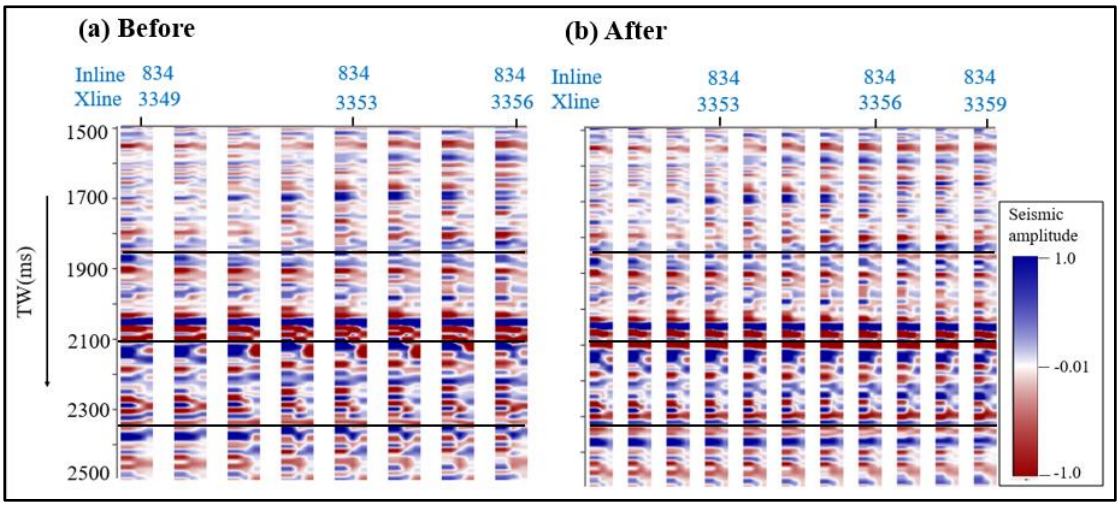

Figure 63: Time alignment for the far angle stacks for PP seismic sections. (a) Stacks before alignment; the black lines mark the most misaligned area. (b) Seismic section after applying the time alignment.

6.3 SEISMIC TO WELL TIE

Two different types of wavelets were calculated for PP and PS seismic angle stacks. The process and algorithm to extract the wavelets is the same as explained in the previous section for synthetic data. Well 30/9-5S and 30/9-J-13H were used to calculate all six wavelets for the PP and PS angle stacks used for seismic to well tie for the respective wells. However, only the wavelets calculated for well 30/9-5S are shown here. Three zero phased PP *ISIS Frequency* wavelets were computed for near (0-15°), mid (15-30°) and far (30-45°) angle stacks (Figure 64). The Figure 64 shows these three different PP wavelets for each angle stacks along with their power spectrum. Similarly, three PS *ISIS Frequency* wavelets for near, mid and far angles were calculated showing an inverted polarity to achieve accurate seismic well tie. These PS wavelets along with their power spectrum are shown in Figure 65.

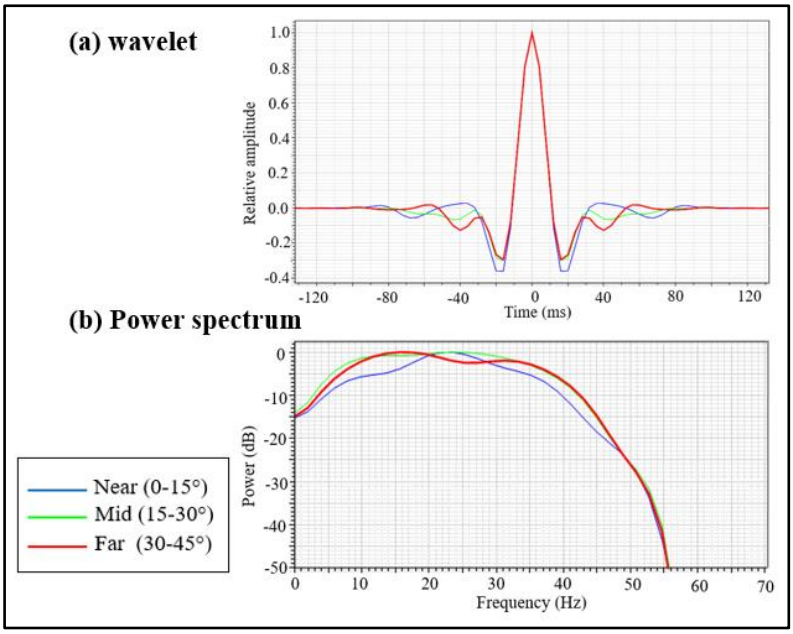

Figure 64: Three PP ISIS Frequency wavelets, centered at zero phase. (a) Shows all three wavelets for near, mid and far angle stacks while (b) is the power spectrum of each wavelet, which shows a frequency range of ca 8-55 Hz.

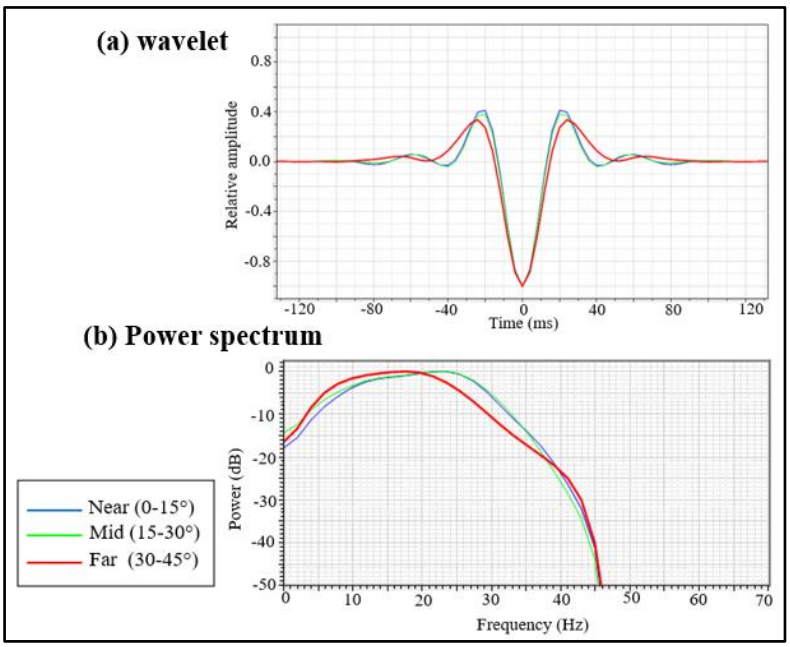

Figure 65: Three PS ISIS Frequency wavelets, centered at -180 phase. (a) Shows all three wavelets for near, mid and far angle stacks while (b) is a power spectrum of each wavelet, which shows a frequency range of ca 8-45Hz. The PS wavelet frequency range is lesser than PP wavelet.

Seismic to well tie was performed for each angle stack for PP and PS seismic sections and for the wells. The seismic to well tie calculated from well 30/9-5S is shown in Figures 66, 67 and 68. The seismic to well ties for near, mid and far angle stacks were achieved for both PP and PS seismic sections. The top and base reservoir represented by the Shetland Group and the Drake Formation, were used as a time boundary for the well tie. Figures 67 and 68 show the well tie section for the PP near angle stack section. The bulk shift of 12ms was applied. A PS well tie section is shown in Figure 69. The well tie sections for the mid and far angle stacks for PP and PS seismic sections are shown in Figures 99, 100, 101, 102, 103 and 104 respectively in Appendix.

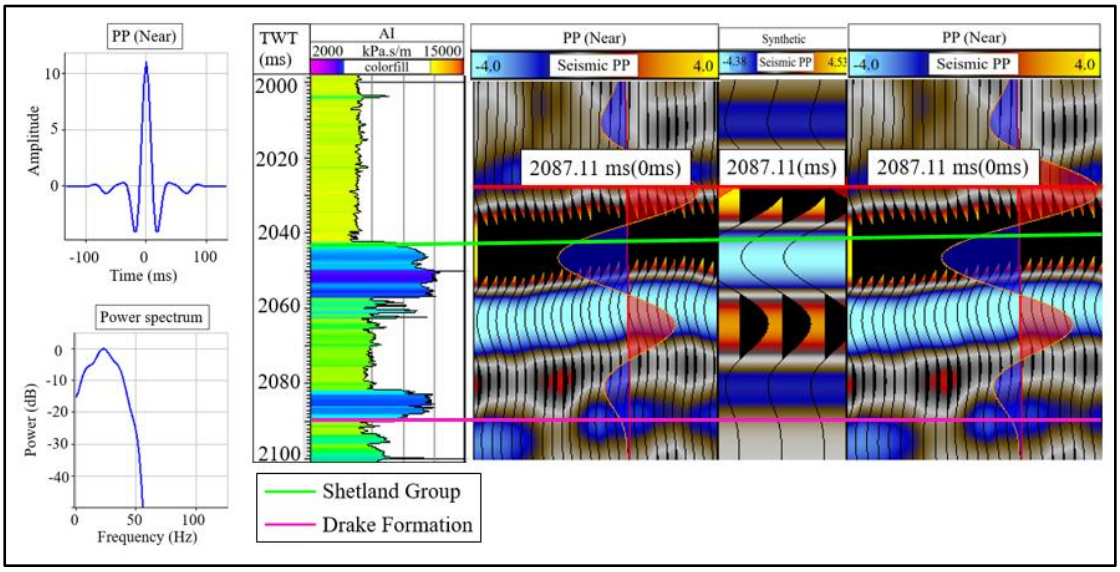

Figure 66: Well tie for the PP (near) seismic section and the well 30/9-5S. On the left side, the PP ISIS wavelet and power spectrum are shown. Next to it, the acoustic impedance log is shown. The seismic data is clearly not matching the well.

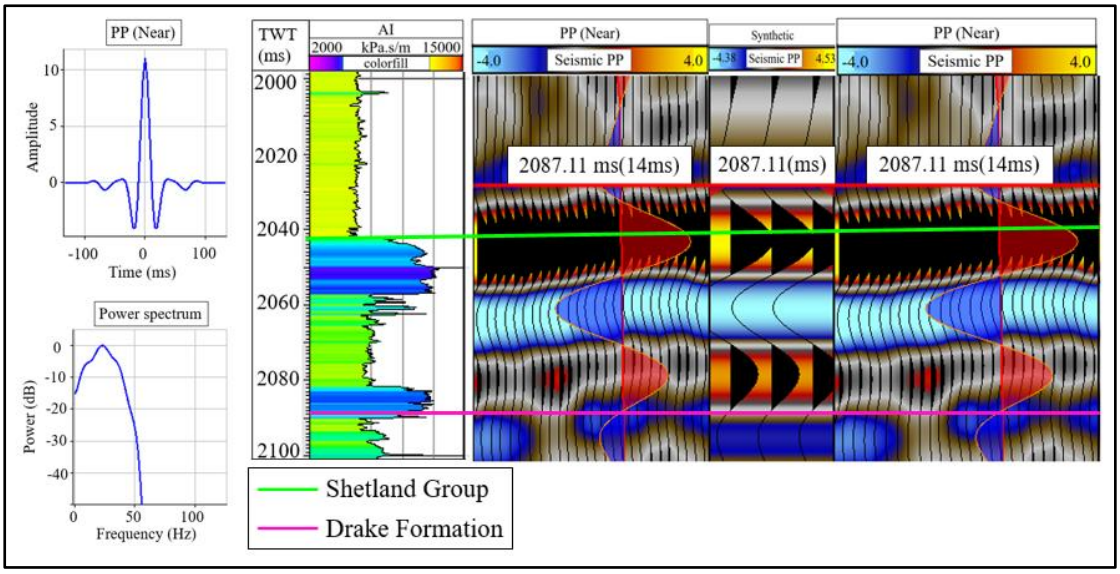

Figure 67: Well tie section of the PP (near) with well 30/9-5S after applying the bulk shift of 14 ms. On the left side, the PP ISIS wavelet and power spectrum are shown. Next to it, the acoustic impedance log is shown. The well data is matching to seismic section after applying the bulk shift.

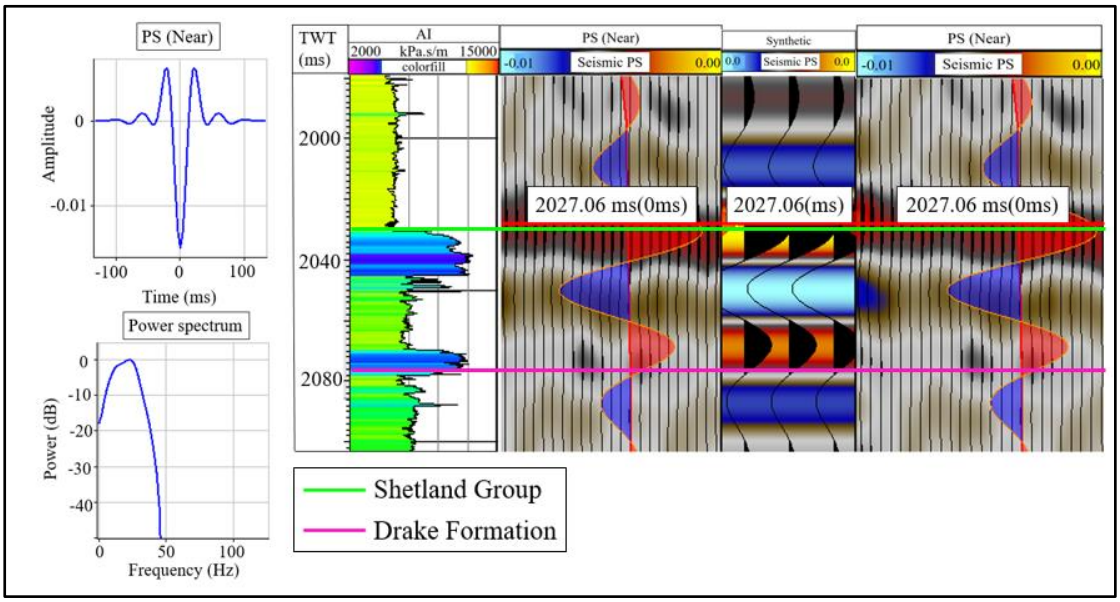

Figure 68: Well tie for the PS seismic section (near) with well 30/9-5S. On the left side, the PS ISIS wavelet and power spectrum are shown. Next to it, the acoustic impedance log is shown. The seismic section is already fairly matching with the well data.

6.4 LOW FREQUENCY MODELS (LFMS)

The low frequency models were calculated by the same process as explained in section 5.4. However, while dealing with real seismic data, four wells 30/9-5S, 30/9-9, 30/9-11 and 30/9-J-13H which also have shear sonic in addition to compressional sonic and the density log, were used to calculate the LFMs. The top and base of the reservoir define the vertical boundaries for the LFMs. The lowest frequency of the seismic power spectrum is 8Hz. Therefore, a high cut filter of 8Hz was applied to the LFMs to encompass the lower frequencies. The LFMs are derived for P-, S- impedance and density and shown in Figure 69 with the respective well logs.

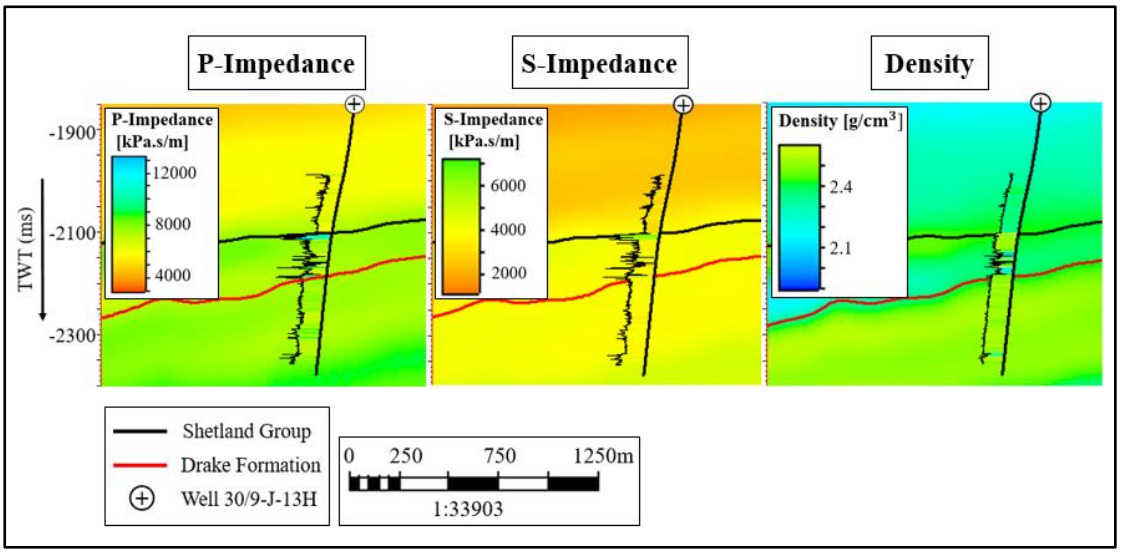

Figure 69: The LFMs based on P-, S-impedance and density are shown here with the respective well logs. The LFMs seem to honor the well log data.

6.5 JOINT PP & PS SIMULTANEOUS INVERSION

The joint PP & PS inversion (Aki & Richards algorithm) was performed on the Oseberg Field data. This method was chosen because according to the 2D modelling results it delivers the most reliable inversion sections in terms of P- and S-impedance. However, the 2D modelling also demonstrates that the density section of the PP & PS inversion is not reliable and cannot be used for the further work. The synthetic data

inversion clarified that the method works best when dealing with a long range of angle stacks. However, for the Oseberg Field only three angle stack, within the range of 0-45° are available.

All six wavelets, three for PP and three for PS angle stacks and LFMs were used for the synthetic stacks calculations. The PP & PS AVO inversion based on the 2D modelling was used as a guide for setting of the inversion parameters. These parameters control the algorithm for determining the optimum synthetic angle stacks that deliver the minimum difference with the measured data. The joint inversion result delivers P-, S- impedance and density cubes, shown in Figures 70 and 71 respectively. In both figures the inversion results for P- and S- impedance are following the well log data, hence confirming the 2D modelling result that joint PP & PS inversion is the most reliable inversion algorithm. The difference between the synthetic and measured PP & PS seismic cubes is shown in Figures 105 and 106, which are present in Appendix.

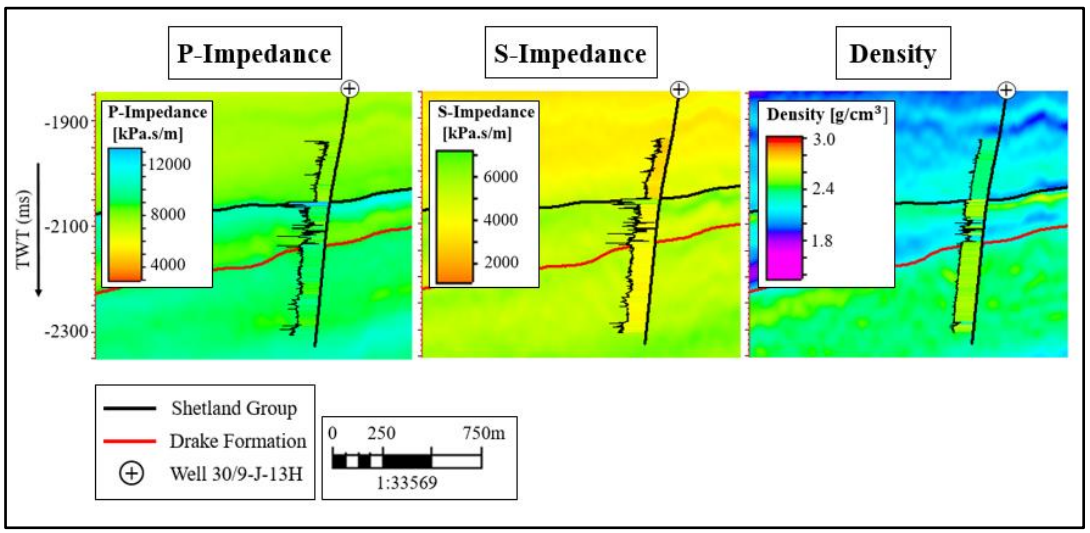

Figure 70: Joint PP & PS inversion results based on the Oseberg Field data. The 2D lines of P-, S- impedance and density are shown with their corresponding well logs.

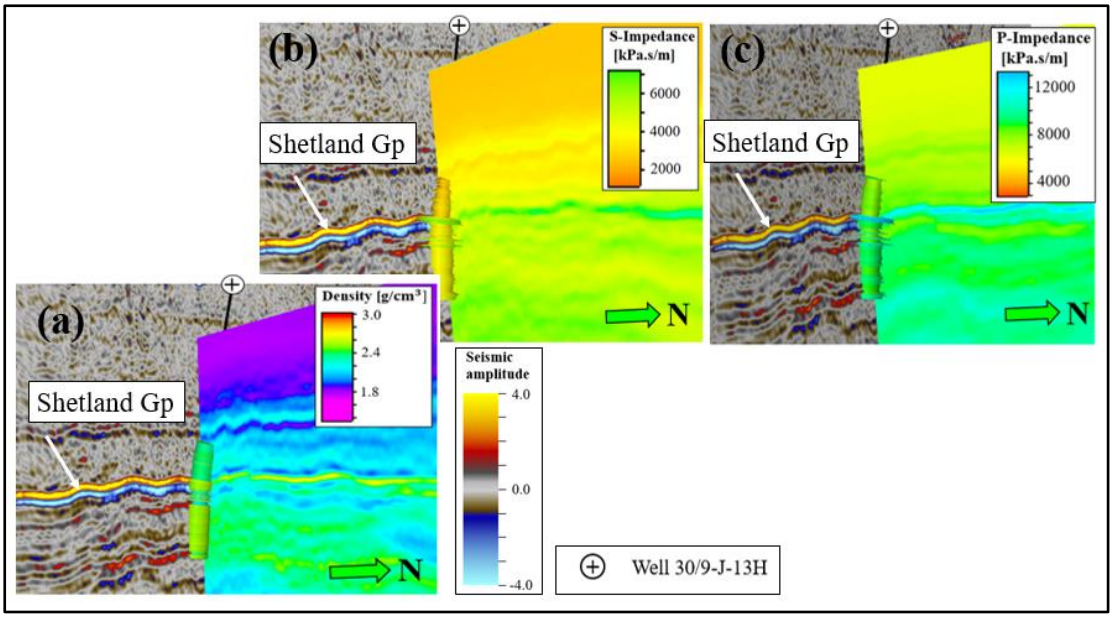

Figure 71: The joint inversion results P-, S- impedance and density are shown along with the seismic sections. The bright red color on seismic section is the top of the Shetland Group, which shows high impedances and density for the inversion results.

6.6 QC OF JOINT INVERSION

Quality control of the inversion is an important technique to check the reliability of inversion results. A tool in *PETREL*, *'inversion QC plot'* was used for this purpose. The tool has a built-in mechanism which compares the seismic inversion attributes to the respective logs. The QC of P-, S- impedance and density cubes was done for each study well. As a representative example, the QC of inversion attributes for well 30/9-J-13H is shown in Figures 72, 73 and 74. The well was used to create LFM and as well was used in inversion. All three inversion results are correlating the well log data reasonably well. This underlines the point of view that the joint inversion is the best algorithm for the Oseberg Field data to compute P-, S- impedance and density cubes.

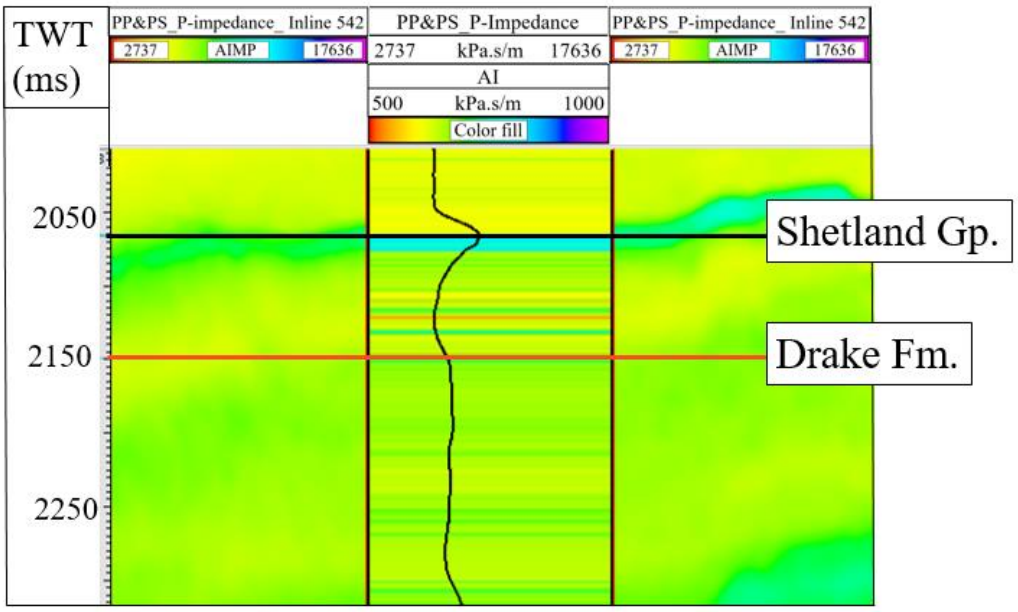

Figure 72: QC of P-impedance results from joint PP & PS inversion of well 30/9-J-13H. The sections show the P-impedance, while the middle track contains the acoustic impedance log and the P-impedance of the inversion.

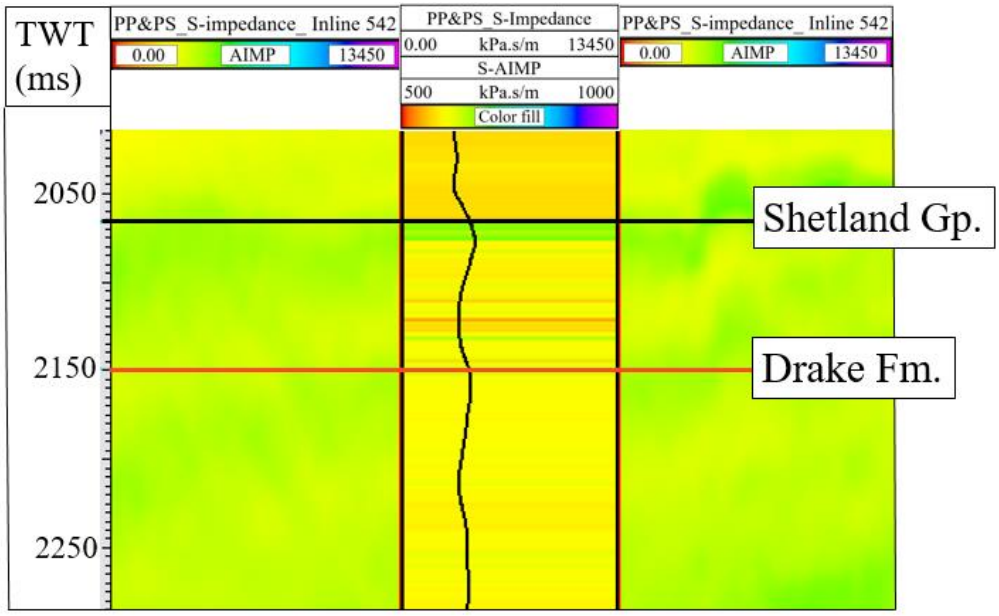

Figure 73: QC of S-impedance results from joint PP & PS inversion of well 30/9-J-13H. The sections are showing the S-impedance based on inversion, while the middle track contains the shear impedance log with the inverted S-impedance.

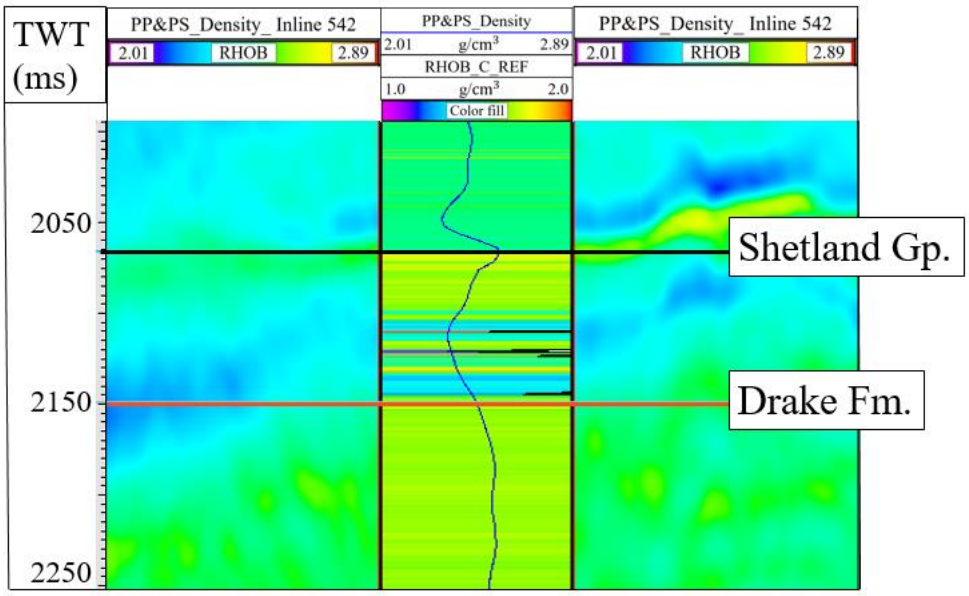

Figure 74: QC of density results from joint PP & PS inversion of well 30/9-J-13H. The tracks at the left and right side are showing the density based on inversion, while the middle track contains the density log and the density from the inversion.

6.6.1 Blind well test

The blind well test is another way to check the reliability of the inversion results. Well 30/9-15 was used for this purpose. It has not been used for the inversion discussed in this thesis. Only the P-impedance and the density sections are shown Figures 75 and 76. The inversion data is matching the well log data reasonably well. The S-impedance shows a similar good match with the well S-impedance log, shown in Figure 107 in Appendix.

6.7 LITHOLOGY ANALYSIS

The lithology analysis allows to calculate the probabilities of litho-facies of the reservoir. The important input to lithology analysis are the facies log, seismic horizons and the logs which are equivalent to the seismic AVO inversion attributes. The probability density function (PDF) graphs derived from the litho-analysis are helpful to estimate the possibility of identifying reliably some specific facies in reservoir zone.

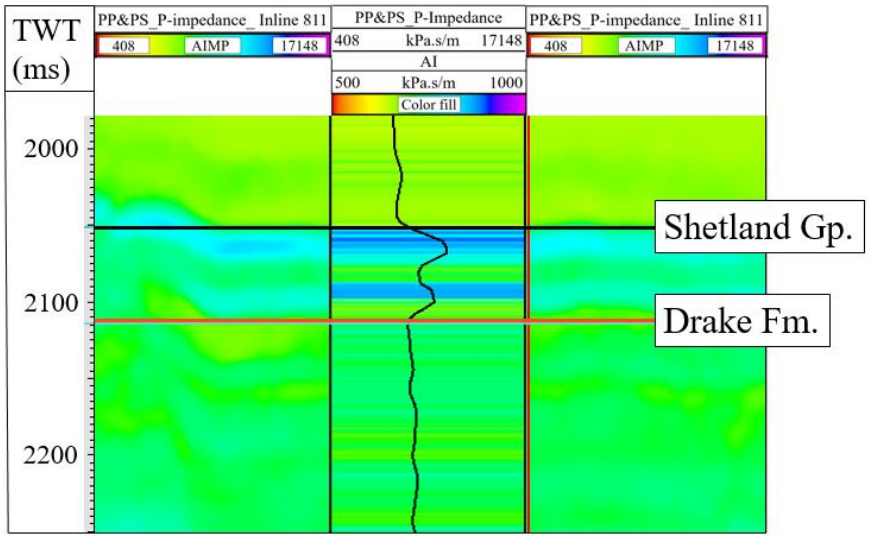

Figure 75: QC of P-impedance results from joint PP & PS inversion of well 30/9-15. The tracks to the left and the right are shown the P-impedance based on inversion, while the middle track contains the acoustic impedance log and inverted P-impedance.

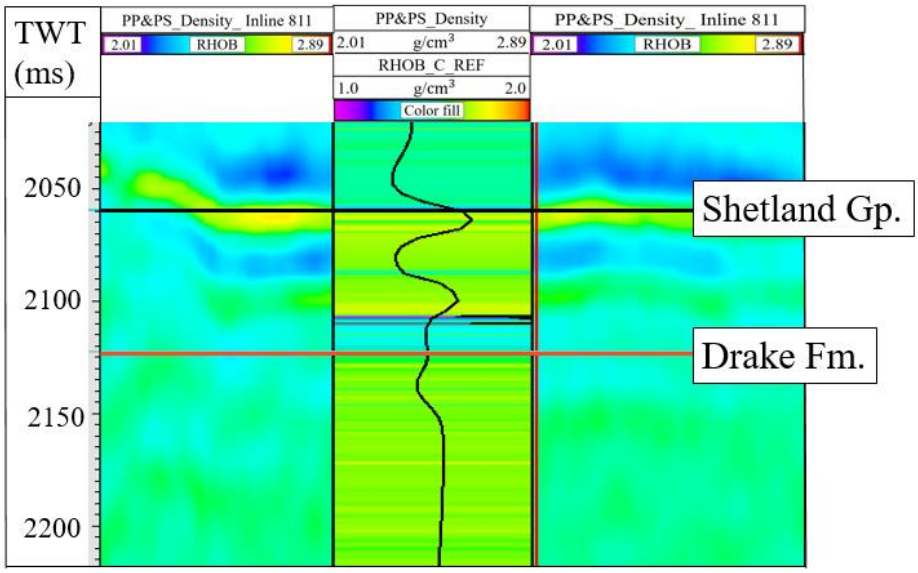

Figure 76: QC of density results from joint PP & PS inversion of well 30/9-15. The tracks to the left and the right are showing the density based on inversion, while the middle track contains the density log and inverted density section.

6.7.1 Facies log

Facies logs can be derived from gamma ray log, volume of shale or water saturation log. However, as described in Table 2 (section 3.1), only well 30/9-J-13H

contains these three important logs. Another method to generate the facies log is based on the acoustic-, shear-impedance and density logs. The acoustic impedance log was used as a main reference log to derive the facies. The analysis was guided by the gamma ray and water saturation log for well 30/9-J-13H. Three main facies were established after investigating the logs and stratigraphy of the reservoir zone. These facies are carbonate, HC sand and shale as shown in the Figure 77. The strong high impedance at the top of the Shetland Group is linked to the presence of carbonates. The facies logs for the other study wells were setup in a similar (Figure 77).

6.7.2 Probability density function (PDF) of facies

The PDF describes the probabilities of a facies to be encountered for a specific set of underlying parameters. In this thesis, PDFs were computed by using facies log along with the P-, S- impedance and density logs. The PDF based on the acoustic impedance discriminates better between the facies compared to the three logs P- and S-impedance combined with density (Figure 78). Table 4 shows how good the individual facies are predicted by the P-impedance log. Note the high degree of prediction for the carbonate and the HC sand. The shale prediction is poor. However, the given a reliable prediction for the carbonate and the HC sand the distribution of the shale is following in a natural way. The PDFs derived by using the combined three logs, P- and S-impedance and density logs, deliver comparable results (Figure 79). Table 5 shows again the predictability of the three facies. Most notably the predictability of the shale has increased.

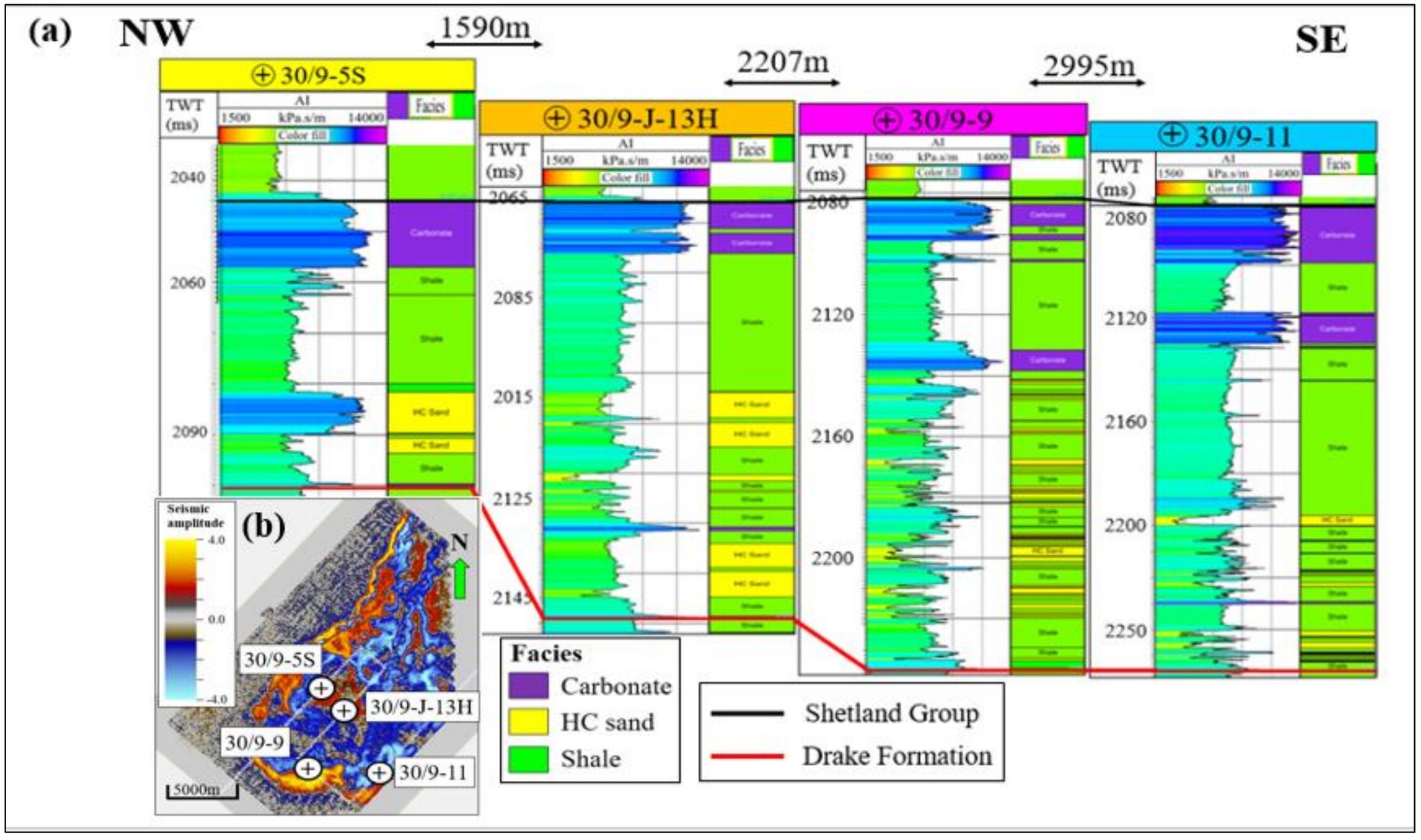

Figure 77: (a) A NW-SE well section with four wells is illustrated here. Facies logs derived from acoustic impedance log are present. The top and the base of the reservoir are marked. (b) The inset shows the location of the wells on a time slice at reservoir depth ca -2100 ms.

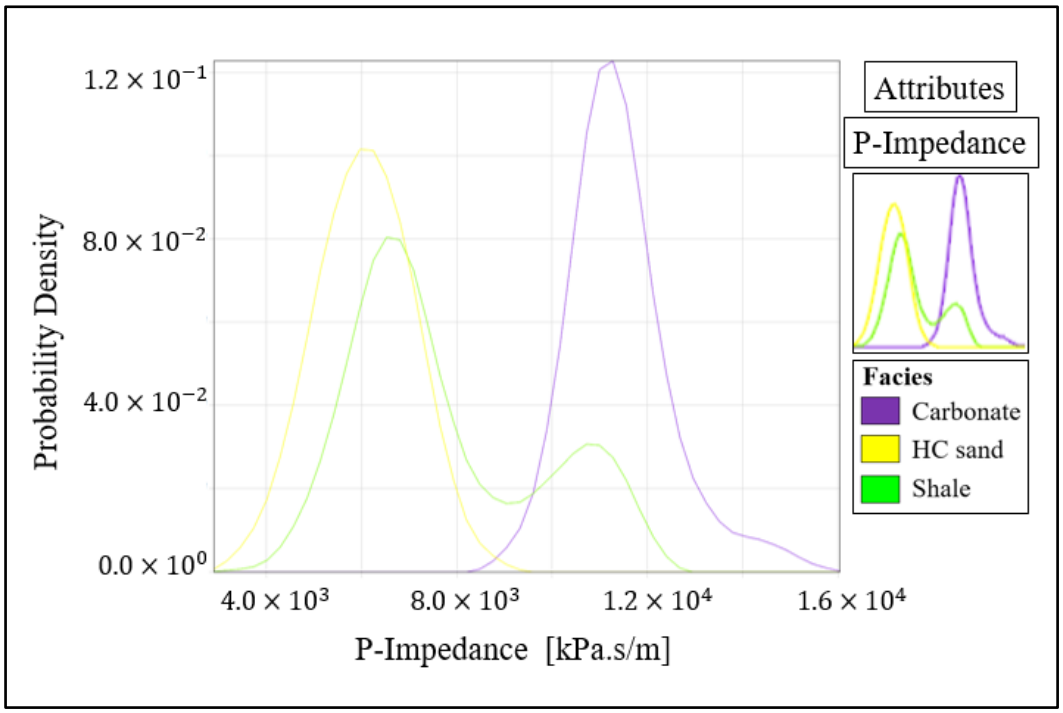

Figure 78: Probability density function derived by using acoustic impedance log. Carbonate separates well from the HC sand and shale. In the small inset the used attributes are shown. The probability values of each facies calculated from this PDF are described in Table 4.

Table 4: The table shows the predictability of the three facies based on the P-impedance.

P (Prediction / True)			
Facies name	Carbonate	Shale	HC Sand
Carbonate	99.09%	24.94%	00.04%
Shale	00.91%	16.51%	08.19%
HC sand	00.00%	58.55%	91.77%

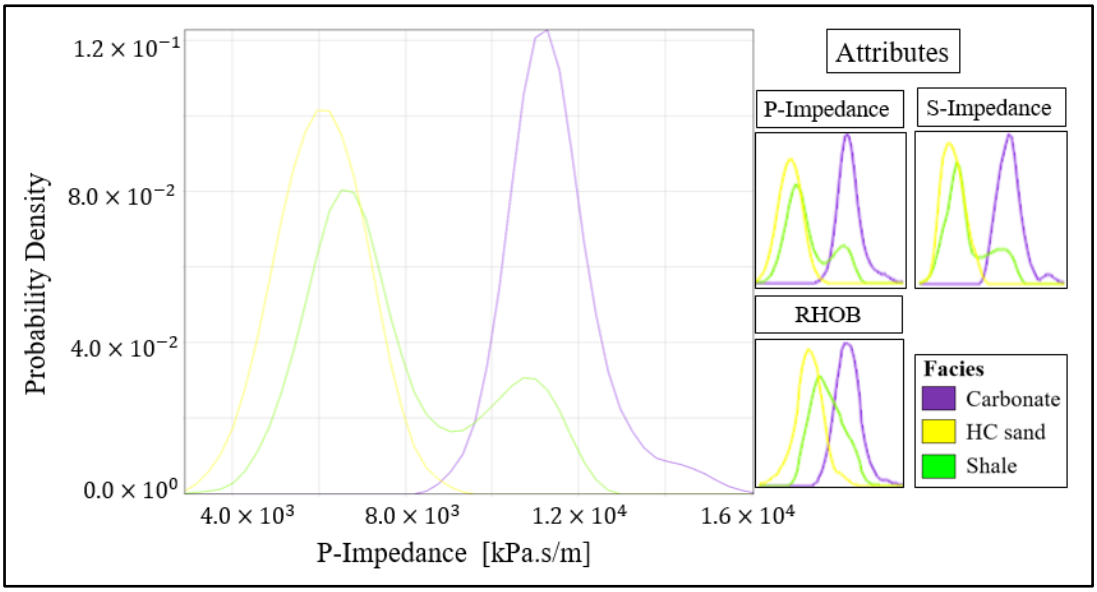

Figure 79: Probability density function graph derived by using P-, S- impedance and density logs. Carbonate separates well from the HC sand and the shale. In the small inset probability density function is given for the individual attribute. The probability values of each facies is given in table 5.

Table 5: The table shows the predictability of the three facies based on the P-, S-impedance and the density.

P (Prediction / True)			
Facies name	Carbonate	Shale	HC Sand
Carbonate	99.59%	22.29%	00.00%
Shale	00.41%	40.13%	16.37%
HC sand	00.00%	37.59%	83.62%

6.7.3 Seismic lithology cube (Litho-cube)

Seismic litho-cube is computed by using seismic inversion attributes and litho-analysis (PDF). The tool *litho-cube* can convert the PDFs into continuous actual facies by using seismic inversion attributes. The litho-cube is limited by the top (Shetland Group) and the base (Drake Formation) surfaces of the reservoir. The facies are plotted between these two boundaries. Litho-cube with all three facies was generated from PDF, based only on the P-impedance. To check the consistency of litho-cube, the facies

logs are illustrated along with the seismic litho-cube in Figure 80. The three facies are shown separately in Figure 81 with the seismic litho-cube to check the accuracy of probability of lithology distribution in the reservoir zone.

The litho-cube derived from the combined P-, S- impedance, and density logs do not correlate with facies log as shown in Figure 82. Out of three wells shown in Figure 82, only the facies log of well 30/9-5S correlates to some extent. Carbonates can be clearly separated from other two facies however; the HC sand and shale are not clearly separable by selected well log data. Moreover, the HC sand and carbonate lacks the continuity. Consequently, the result based on the P-impedance, is regarded as more reliable and is used for the subsequent analysis.

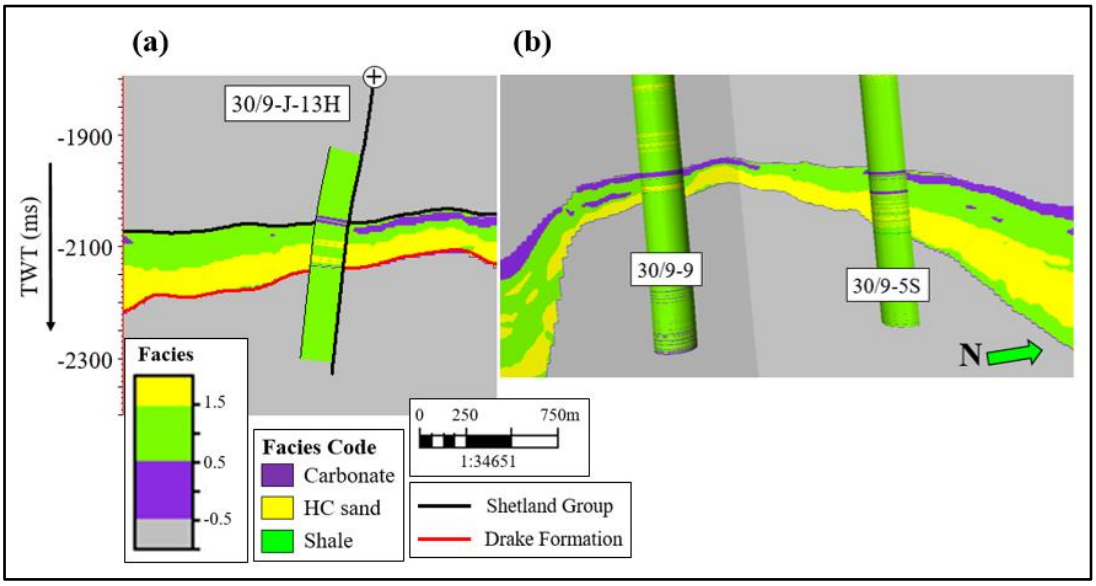

Figure 80: Facies log is shown with seismic lithology cube. (a) 2D line of the seismic lithology cube with facies log for well 30/9-J-13H. The seismic lithology cube honoring the carbonate and HC sand facies quite well. (b) Two wells 30/9-9 and 30/9-5S are shown together with the litho-cube section. Seismic lithology and log data are in reasonable agreement.

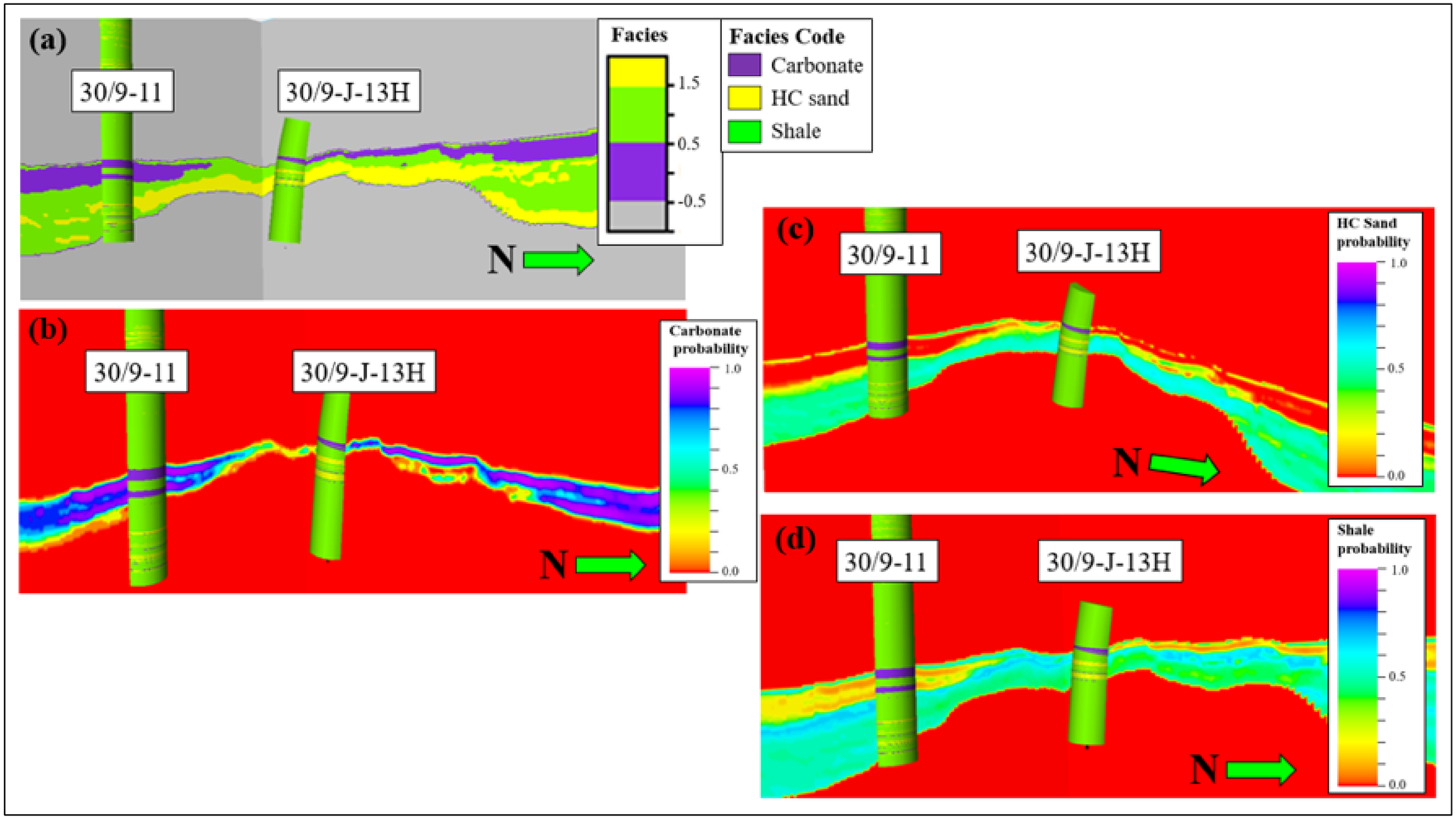

Figure 81: Facies logs are shown with the seismic litho-cube to observe the facies distribution. The wells 30/9-J-13H and 30/9-11 are used. (a) Classifies all the facies. (b) Shows the carbonates. (c) Depicts the HC sand in the reservoir. (d) Shows the distribution of shale in reservoir zone. All facies in seismic litho-cube are honoring the facies log for both wells.

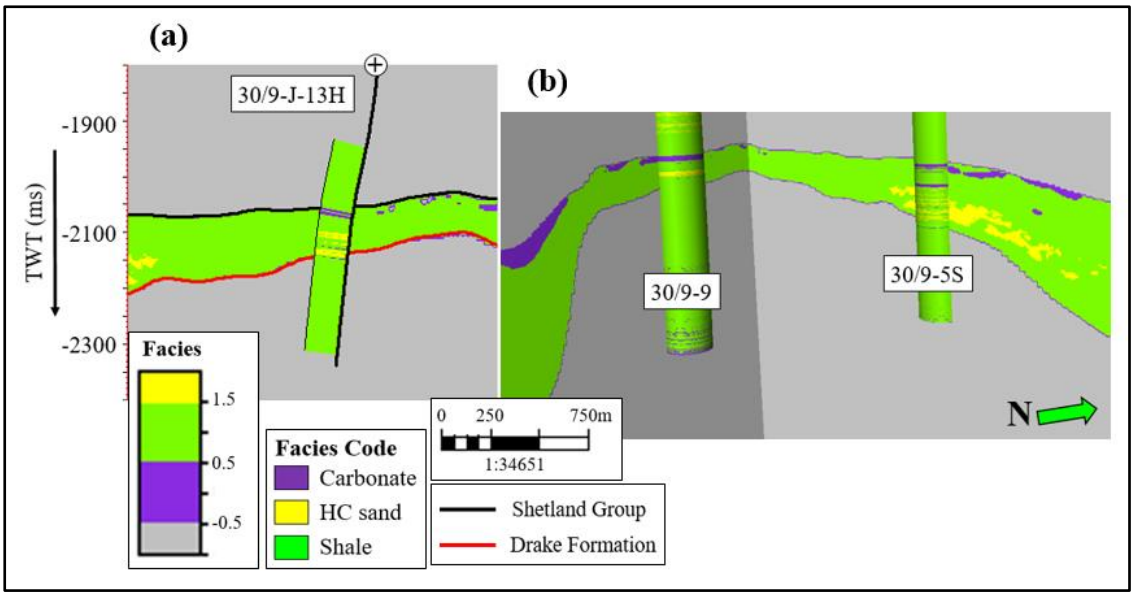

Figure 82: Facies log is shown with seismic lithology cube. (a) 2D line of the seismic lithology cube with facies log for well 30/9-J-13H. The seismic lithology does not correlate with facies log. (b) Two wells 30/9-9 and 30/9-5S are shown together with the litho-cube section. Only well 30/9-5S correlating the facies log quite well.

6.8 LITHOLOGY CLASS MAP

The outcome of this thesis is to construct the lithology map of the reservoir zone of the Oseberg Field. Based on the available PSDM velocity cube, the seismic litho-cube was converted into the depth domain and the facies thickness mapped for the reservoir. In Figure 83, three lithology classes/facies isochores maps are shown for the reservoir. From the maps it can be observed that the northeast part of the reservoir has mainly shale, while in the southwestern part the HC sand is dominating.

The Figure 84 elaborates the lithology class map with respect to the facies log of the wells 30/9-J-13H and 30/9-15. It is clear from this figure that the HC sand class predicted mainly on the southwestern side of the reservoir, and the facies log of the wells are in good agreement with the observation. The shale is dominating the northeastern flank of the reservoir which is confirmed by the facies log of well 30/9-15.

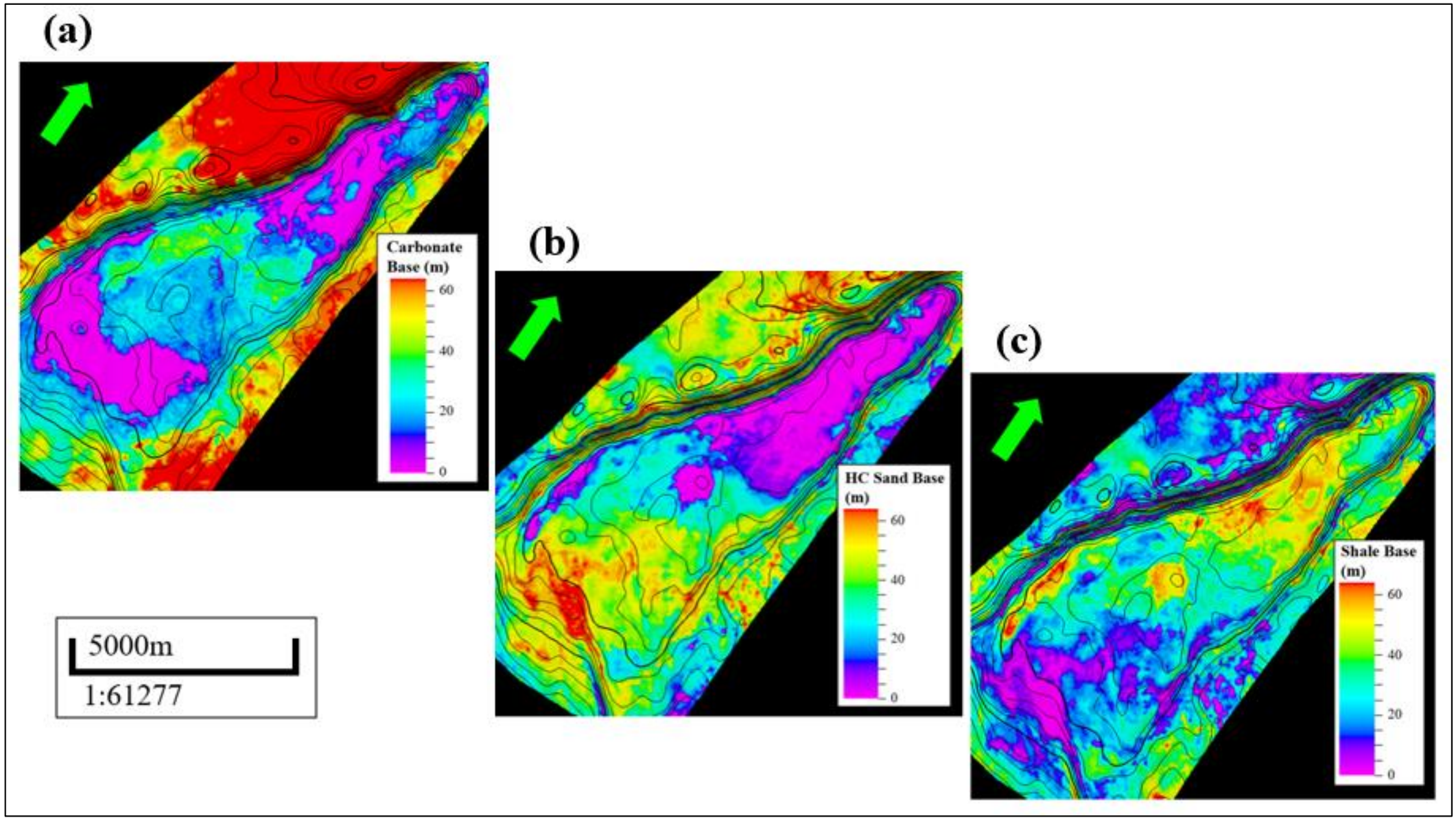

Figure 83: The lithology distribution maps for the reservoir zone at depth of ca -2080. The high topographic structure is the area of interest. (a) Carbonate facies are showing a high distribution in the middle of the reservoir. (b) The SW part of the reservoir is mainly consisting of HC sand. (c) Shale is more distributed on NE side of the reservoir.

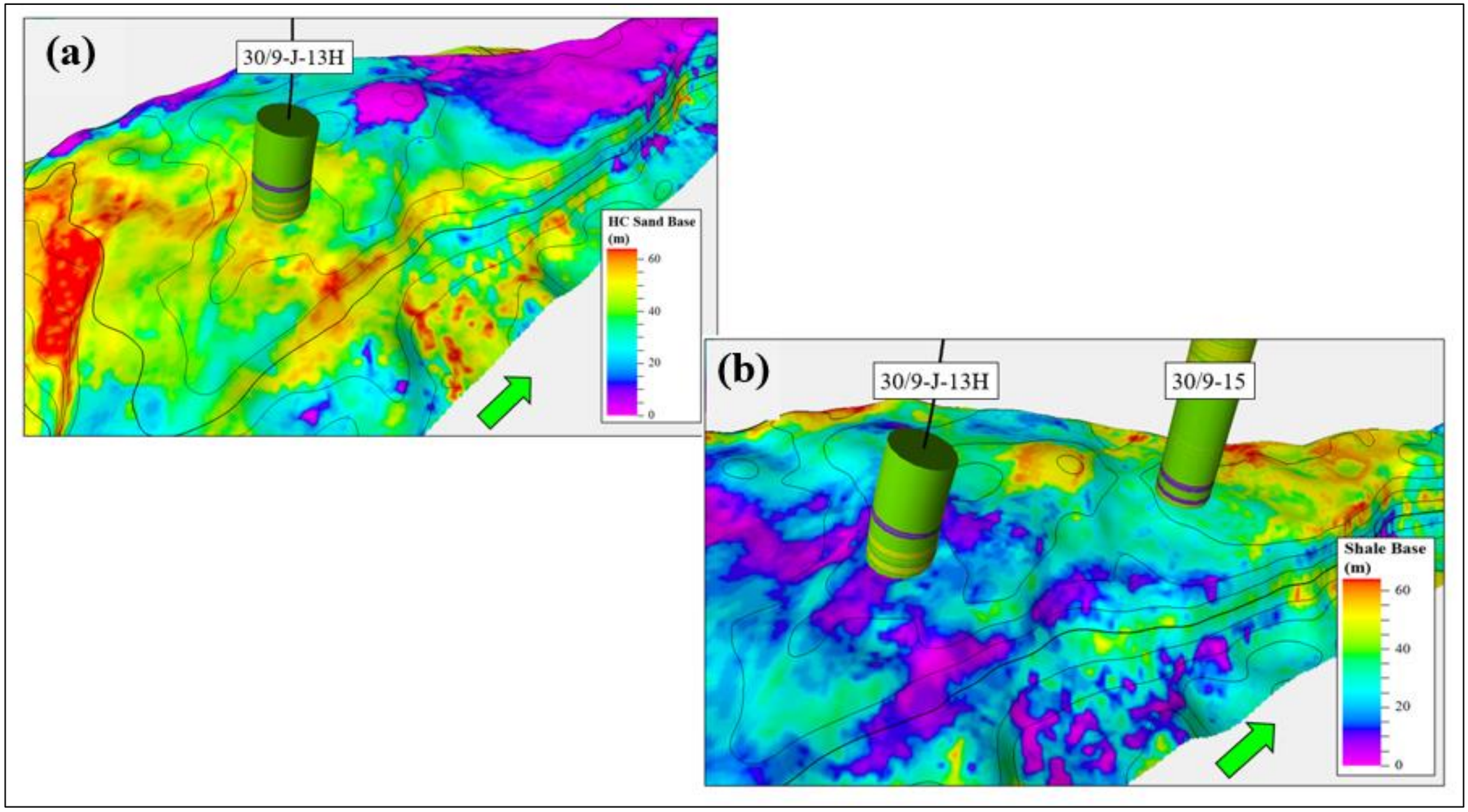

Figure 84: The two lithology class maps are shown along with the facies logs of the wells 30/9-J-13H and 30/9-15. (a) Shows the HC sand map with the facies log of well 30/9-J-13H. (b) The map the shale distribution with the facies log of the two wells 30/9-J-13H and 30/9-15.

7. DISCUSSION

This thesis compares the different inversion algorithms mentioned in Table 3; post-stack, PP AVO (Aki & Richards and Fatti et al. approximations), PS AVO (Aki & Richards approximation) and joint PP & PS AVO (Aki & Richards approximation). The inquiry was carried out on 2D synthetic data which consists of two sets of angle stacks. The first one contains three angles stacks which covers the angle range from 0-45°, the second one includes five sets of angle stacks covering 0-55°. Both sets of angle stacks comprises of PP and PS angle stack sections. Different inversion algorithms were applied to the data sets and the P-, S- impedance and density sections were calculated. The QC of these results shows that the joint inversion PP & PS is most reliable for P- and S- impedance, however it does not calculate a reliable density section. Comparing the results of the two angle stacks data sets, the one with five angle stacks delivers more reliable results. The important thing to note is the behavior of the density section. According to literature, AVO inversion delivers a reliable density cube typically while dealing with several angle stacks covering a large or ultra large angle range. However, in this thesis, the 2D modelling does not deliver the reliable density section. However, the joint inversion of the three-stack data from the Oseberg Field is providing a reliable density cube, though the angle stacks cover a range of only 0-45°. An explanation of this reason cannot be given.

The limitations of this project primely relate to inadequacy of available inversion algorithms and lack of well log data. For PP AVO simultaneous inversion algorithm Aki & Richards and Fatti et al. approximations were available. While for PS AVO and joint simultaneous inversion only Aki & Richards approximations were accessible. This condition lowers the possibility of exploring many inversion algorithms. To investigate other approximations, one should enhance the capability of software by adding programming and coding related to the approximations.

Lack of well log data is slightly affecting the seismic litho-cube and ultimately the reservoir mapping. Only well 30/9-J-13H has gamma ray (GR), volume of shale (Vsh) and effective water saturation (SWE) logs. These logs are basics to make the facies log, which is used for the seismic litho-cube.

No geophysical current research or literature exists in public domain, to my approach, that documents the joint inversion of the Oseberg Field data. Therefore, the inversion results of this study cannot be compared with published work.

Future research studies can be carried out in order to get more reliable probability density functions (PDFs) for the facies, using rock moduli such as Young or Poisson's ratio. The reliability of the density cube coming from the AVO inversion based on the 2D forward modelling data should be investigated. For this purpose, one can increase the angle range or apply algorithms other than the Aki & Richards approximations.

8. CONCLUSIONS

Four different inversion algorithms were tested by using 2D synthetic seismic data as mentioned in the previous section. It is recognized that the four inversion algorithms are working better while applying on long range of angle stacks. By observing the results, it is found that joint PP & PS simultaneous inversion is the most reliable method for delivering P- and S- impedance cube. This supports the experience that compressional waves combined with shear waves, carries more information about the rock physics properties i.e. impedances, density, etc.

The joint PP & PS simultaneous inversion is applied on the Oseberg Field data, which led us to new insight of the reservoir properties. The inverted P, S- impedance and density cubes honored the well log data, stating the fact that inversion is reliable.

By using the inversion seismic attributes, and the facies logs the seismic lithology cube was constructed. The litho-cube helped to map the reservoir zone between the Shetland Group and the Drake Formation. Three facies carbonate, HC sand and shale were mapped in the reservoir. The maps exhibit that the reservoir is HC sand prone on the south-western part while the north-eastern part mainly consists of shale.

9. REFERENCES

Aki, K., & Richards, P. G. (2002). *Quantitative seismology*.

Barclay, F., Bruun, A., Rasmussen, K. B., Alfaro, J. C., Cooke, A., Cooke, D., . . . McHugo, S. (2008). Seismic inversion: Reading between the lines. *Oilfield Review, 20*(1), 42-63.

Barkved, O., Bartman, B., Gaiser, J., Van Dok, R., Johns, T., Kristiansen, P., . . . Thompson, M. (2004). The many facets of multicomponent seismic data. *Oilfield Review, 16*(2), 42-56.

Booth, A. D., Emir, E., & Diez, A. (2015). Approximations to seismic AVA responses: Validity and potential in glaciological applications. *Geophysics, 81*(1), WA1-WA11.

Caldwell, J., Christie, P., Engelmark, F., McHugo, S., Özdemir, H., Kristiansen, P., & MacLeod, M. (1999). Shear waves shine brightly. *Oilfield Review, 11*(1), 2-15.

Cooper, B., & Barnard, P. (1984). Source rocks and oils of the central and northern North Sea.

Davies, D., McInalley, A., & Barclay, F. (2003). Lithology and fluid prediction from amplitude versus offset (AVO) seismic data. *Geofluids, 3*(4), 219-232.

Directorate, N. P. (2018). FactMaps.

Faerseth, R. B. (1996). Interaction of Permo-Triassic and Jurassic extensional fault-blocks during the development of the northern North Sea. *Journal of the Geological Society, 153*(6), 931-944. doi:10.1144/gsjgs.153.6.0931

Faerseth, R. B., & Ravnås, R. (1998). Evolution of the Oseberg fault-block in context of the northern north sea structural framework. *Marine and Petroleum Geology, 15*(5), 467-490. doi:https://doi.org/10.1016/S0264-8172(97)00046-9

Farvardini, M. (2017). The Sedimentological Distribution of Upper Brent, Oseberg Field, North Sea. In.

Ganssle, G. (2012). Calculation of a Synthetic Gather using the Aki-Richards Approximation to the Zoeppritz Equations.

Glennie, K. W. (2009). *Petroleum Geology of the North Sea Basic Concepts and Recent Advances*: Wiley-Blackwell.

Graue, E., Helland-Hansen, W., Johnsen, J., Lømo, L., Nøttvedt, A., Rønning, K., . . . Steel, R. (1987). Advance and retreat of Brent delta system, Norwegian North Sea. *Petroleum geology of north west Europe*, 915-937.

Halland, E. K., Gjeldvik, I., Johansen, W., Magnus, C., Meling, I., Pedersen, S., . . . Tappel, I. (2011). *CO2 Storage Atlas Norwegian North Sea* (Vol. 600).

Hammer, H., Kolbjørnsen, O., Tjelmeland, H., & Buland, A. (2012). Lithology and fluid prediction from prestack seismic data using a Bayesian model with Markov process prior. *Geophysical Prospecting, 60*(3), 500-515.

Hampson, D. (2010). Lithology Prediction using Seismic Inversion Attributes.

Haq, B. U., Hardenbol, J., & Vail, P. R. (1987). Chronology of fluctuating sea levels since the Triassic. *Science, 235*(4793), 1156-1167.

Ilesanmi, M. (2013). Linearization of Zoeppritz equations and practical utilization. *International Journal of Physical Sciences, 8*(24), 1298-1306.

Industry, N. P. (2018). Fact Maps.

Johnsen, J. R., Rutledal, H., & Nilsen, D. E. (1995). Jurassic reservoirs; field examples from the Oseberg and Troll fields: Horda Platform area. *Norwegian Petroleum Society Special Publications, 4*, 199-234.

Knot, C. (1899). Reflection and refraction of elastic waves with seismological application. *Philos. Mag, 5*, 64-97.

Knudsen, B.-E., Liljedahl, T., Midbøe, P., & Søderstrøm, B. (1997). Oblique rifting and sequential faulting in the Jurassic development of the northern North Sea. *Journal of Structural Geology, 19*(10), 1285-1302.

Kristiansen, P. (2000). *years experience with 4C seismic: what we have learned: Presented at the SEG.* Paper presented at the EAGE Summer Research Workshop, Boise, Idaho.

Latimer, R. B., Davidson, R., & Riel, P. v. (2000). An interpreter's guide to understanding and working with seismic-derived acoustic impedance data. *The Leading Edge, 19*(3), 242-256. doi:10.1190/1.1438580

Roberts, A. M., Price, J. D., & Olsen, T. S. (1990). Late Jurassic half-graben control on the siting and structure of hydrocarbon accumulations: UK/Norwegian Central Graben. *Geological Society, London, Special Publications, 55*(1), 229-257.

Russell, B., & Hampson, D. (1991). Comparison of poststack seismic inversion methods. In *SEG Technical Program Expanded Abstracts 1991* (pp. 876-878).

Russell, B., & Hampson, D. (2004). AVO theory. *Hampson-Russell Software Services Ltd*, 22-26.

SEG. AVO equations. *SEG Wiki.* Retrieved from https://wiki.seg.org/wiki/AVO_equations

Sheriff, R. E., & Geldart, L. P. (1995). Exploration seismology. In (2nd ed., pp. 73-83): Cambridge university press.

Shuey, R. (1985). A simplification of the Zoeppritz equations. *Geophysics, 50*(4), 609-614.

Spencer, A., Holter, E., Campbell, C., Hanslien, S., Nelson, P., Nysæther, E., & Ormaasen, E. (1987). Geology of the Norwegian oil and gas fields. *Norwegian Petroleum Society: London, Graham & Trotman*.

Stewart, R. R., Gaiser, J. E., Brown, R. J., & Lawton, D. C. (1999). Converted-wave seismic exploration: a tutorial. *CREWES Res Rep, 11*.

Stewart, R. R., Gaiser, J. E., Brown, R. J., & Lawton, D. C. (2003). Converted-wave seismic exploration: Applications. *Geophysics, 68*(1), 40-57.

Telford, W. M., Telford, W., Geldart, L., & Sheriff, R. E. (1990). *Applied geophysics* (Vol. 1): Cambridge university press.

Ten Kroode, F., Bergler, S., Corsten, C., de Maag, J. W., Strijbos, F., & Tijhof, H. (2013). Broadband seismic data—The importance of low frequencies. *Geophysics, 78*(2), WA3-WA14.

Ter Voorde, M., Ravnås, R., Faerseth, R., & Cloetingh, S. (1997). Tectonic modelling of the Middle Jurassic synrift stratigraphy in the Oseberg–Brage area, northern Viking Graben. *Basin Research, 9*(2), 133-150.

Veeken, P., & Da Silva. (2004). Seismic inversion methods and some of their constraints. *First break, 22*(6), 47-70.

Verwest, B. (2004). *Elastic impedance revisited.* Paper presented at the 66th EAGE Conference & Exhibition.

Wang, Y. (2016). *Seismic inversion: theory and applications*: John Wiley & Sons.

Waters, K. H. (1987). *Reflection seismology : a tool for energy resource exploration* (3rd ed. ed.). New York: Wiley.

Yoong, A. A., Lubis, L. A., & Ghosh, D. P. (2016). *Application of Simultaneous Inversion Method to Predict the Lithology and Fluid Distribution in "X" Field, Malay Basin.* Paper presented at the IOP Conference Series: Earth and Environmental Science.

Zoeppritz, K. (1919). *Nachrichten von der Gesellschaft der Wissenschaften zu Göttingen, Mathematisch-Physikalische Klasse*.

10. APPENDIX

The appendix mostly contains the figures from chapter 5 and 6. The figures are shown here are the parts of results.

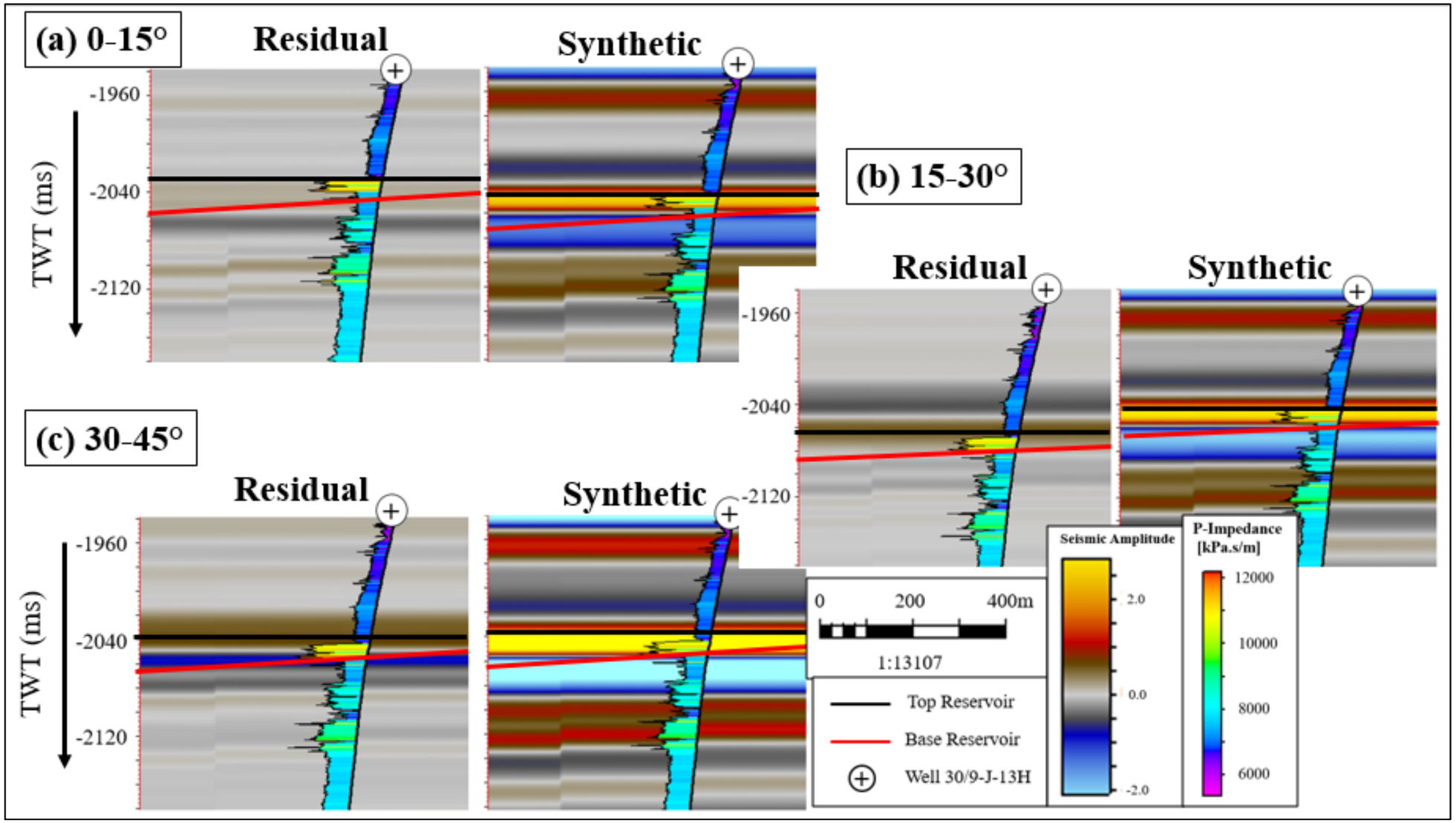

Figure 85:The difference between synthetic and measured angles stacks (residuals) are shown here for three set of angle stacks based on Aki and Richards inversion algorithm.

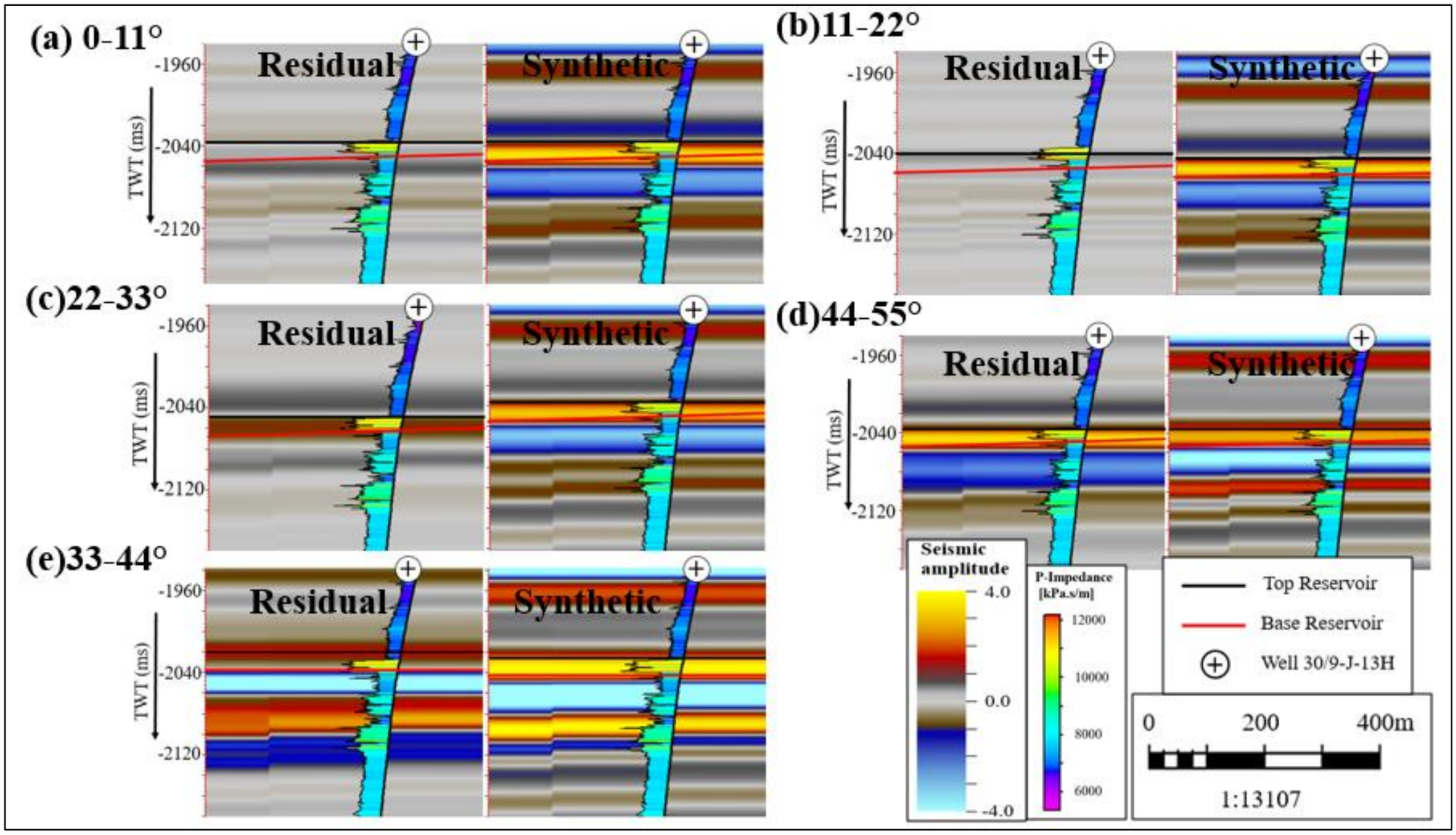

Figure 86: The difference between synthetic and measured angles stacks (residuals) are shown here for the five set of angle stacks

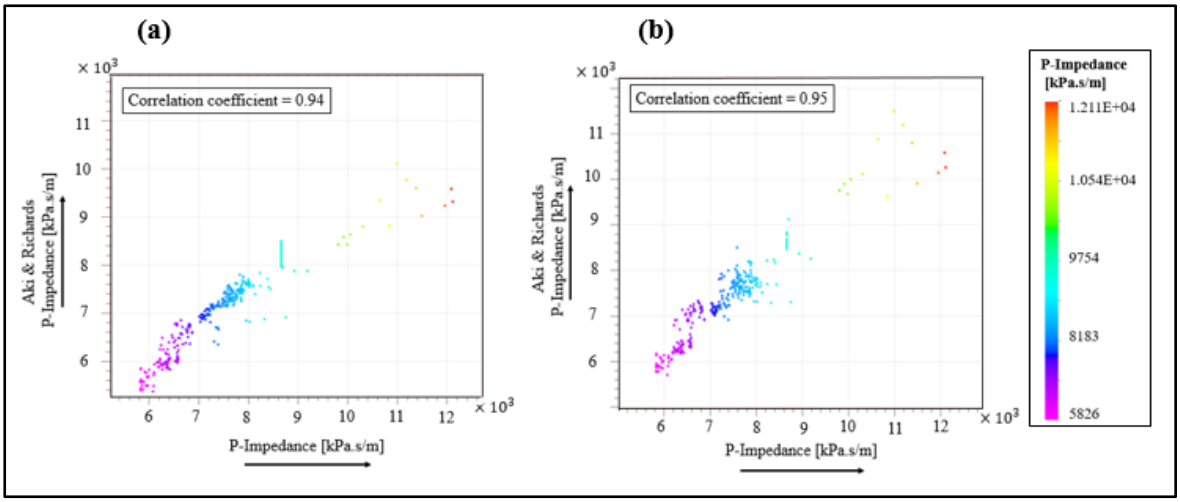

Figure 87: QC Cross plots of Aki and Richards inversion results. (a) Cross plot between modelled and Aki & Richards inverted P-impedance for three angle stacks of set shows a correlation coefficient of 0.94. (b) Is a cross plot for the same parameters for five angle stacks set. This shows a correlation coefficient of 0.95.

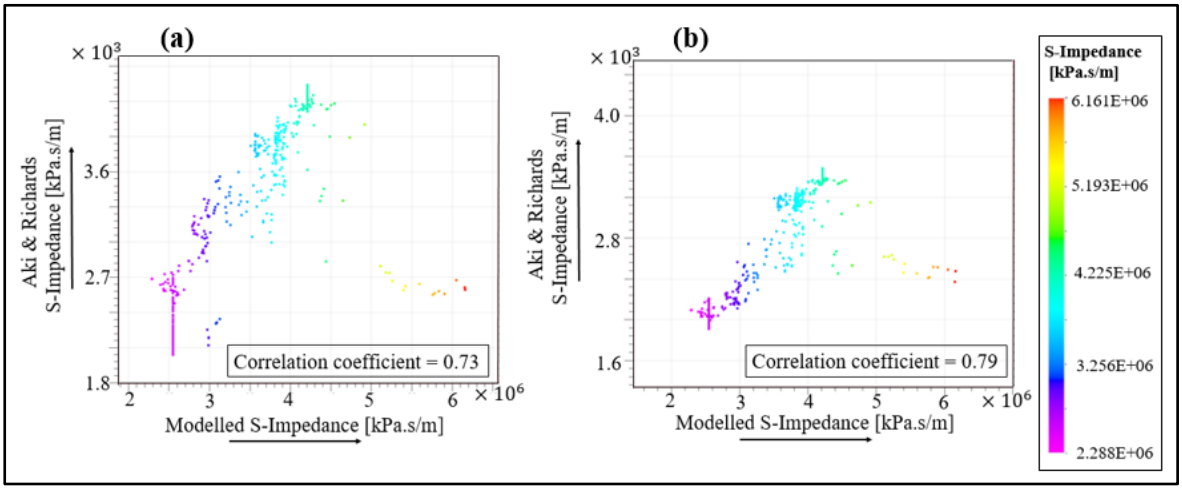

Figure 88: QC Cross plots of Aki and Richards inversion results. (a) Cross plot between modelled and Aki & Richards inverted S-impedance for three angle stacks of set shows a correlation coefficient of 0.73. (b) Is a cross plot for the same parameters for five angle stacks set. This shows a correlation coefficient of 0.79.

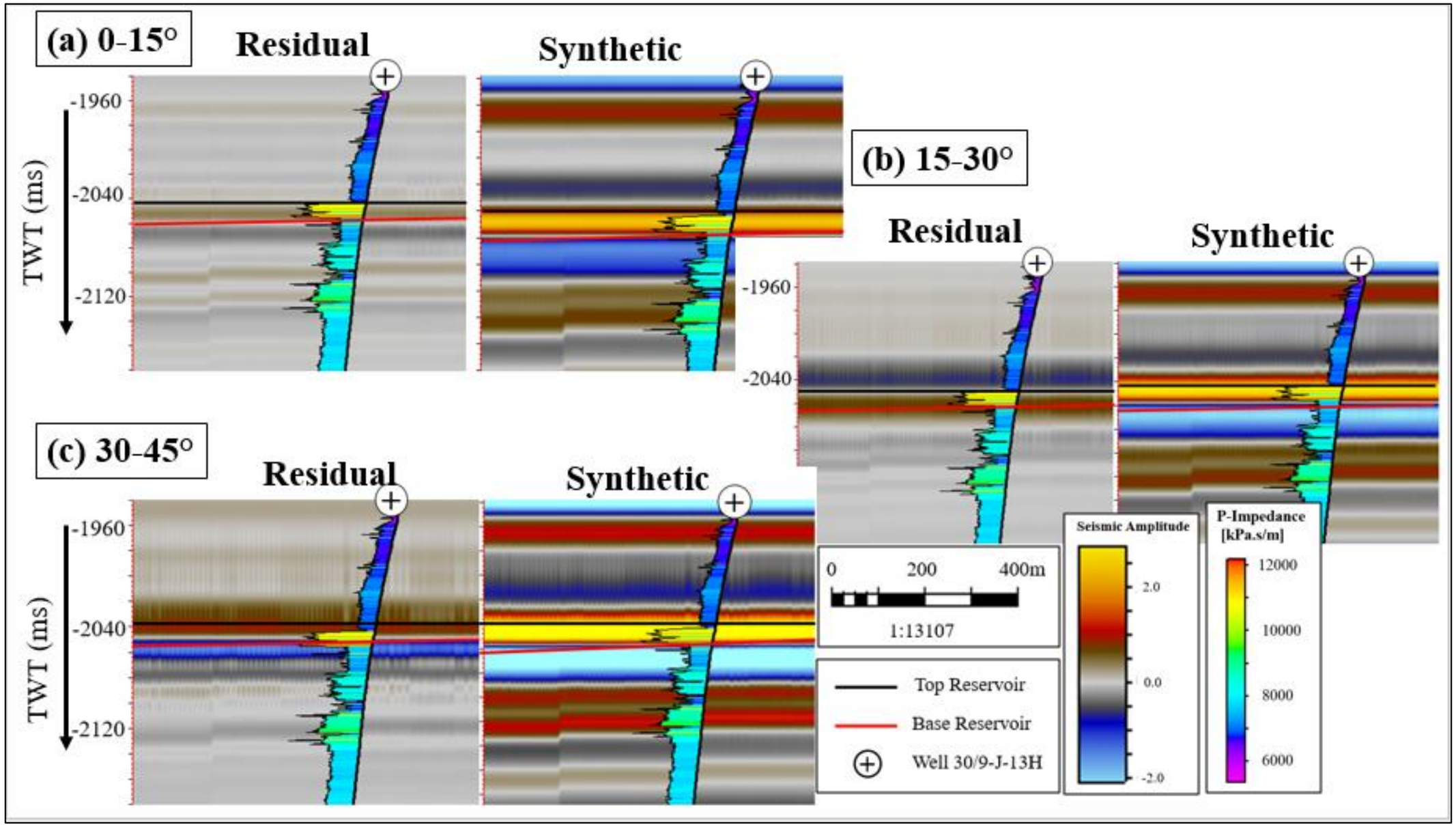

Figure 89: The inversion results from Fatti et al. algorithm for three angles stacks set is shown here. The difference (residual) between the synthetic and measured angle stacks and the synthetic PP angle stacks are shown here separately.

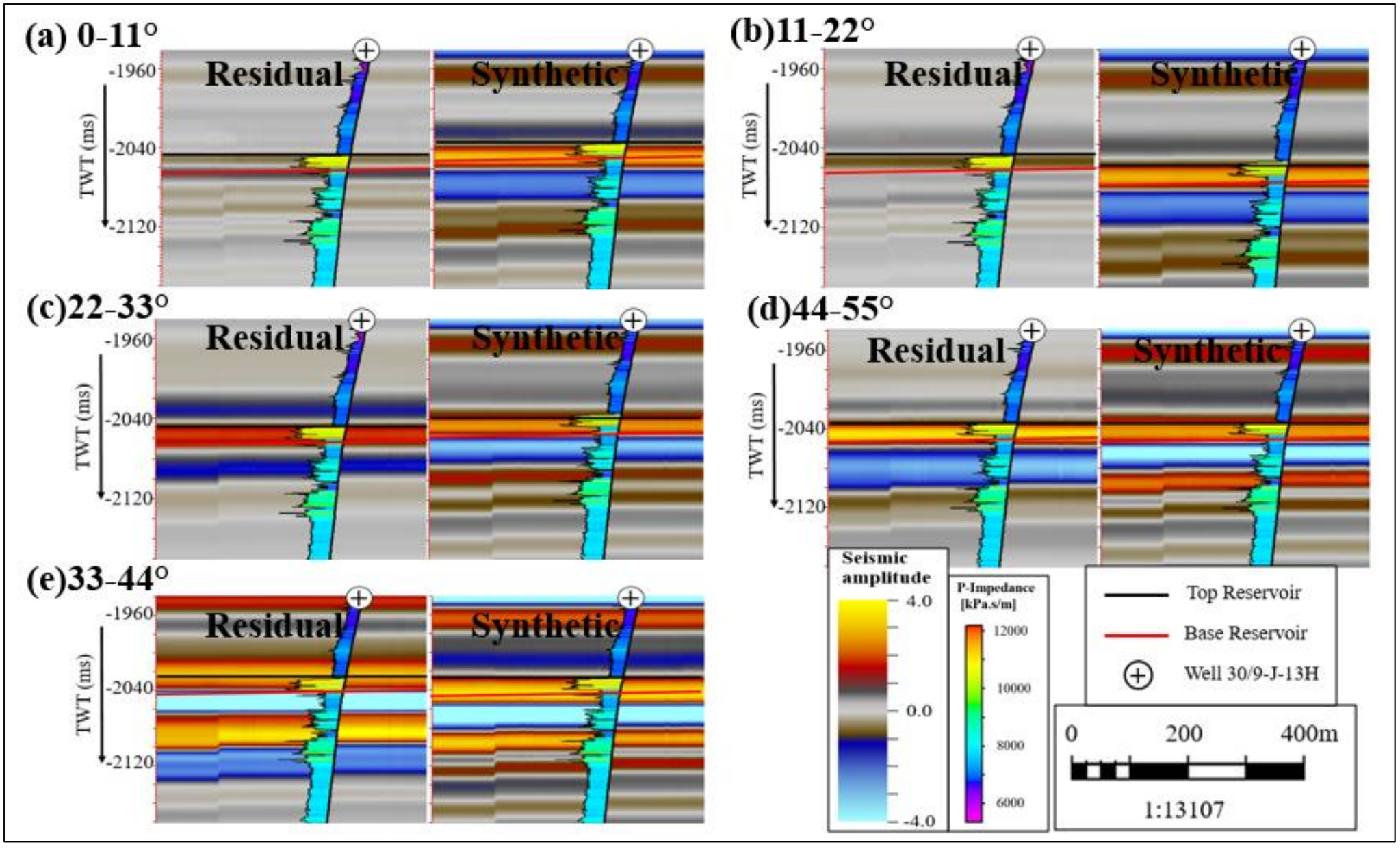

Figure 90:The inversion results from Fatti et al. algorithm for five angles stacks set is shown here. The difference (residual) between the synthetic and measured angle stacks and the synthetic PP angle stacks are shown here separately.

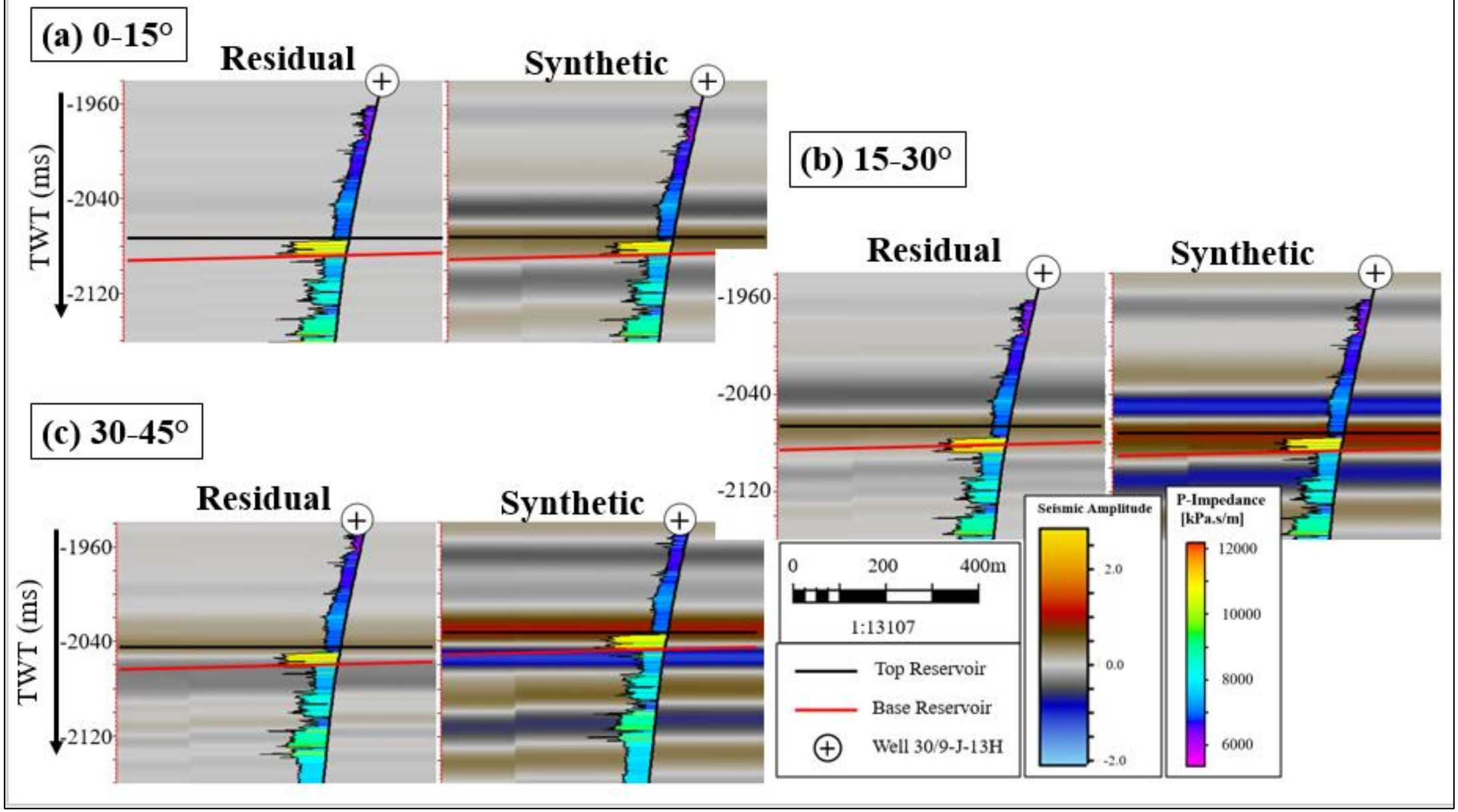

Figure 91: The results from PS AVO inversion for sets of three angle stacks by using the algorithm of Aki & Richards. The difference (residual) between the synthetic and measured PS angle stacks and the synthetic angle stacks are shown here separately.

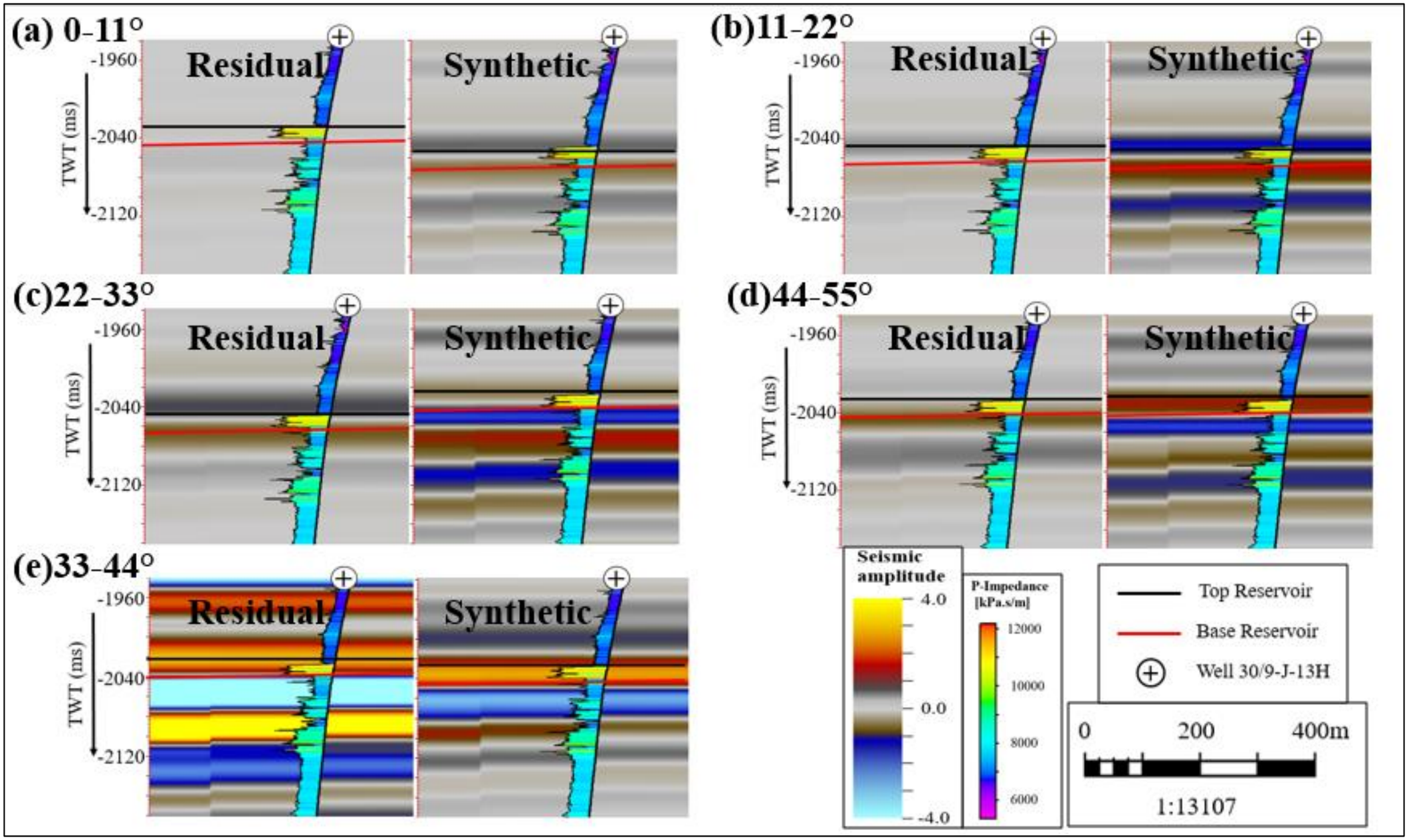

Figure 92: The results from PS AVO inversion for sets of five angle stacks by using the algorithm of Aki & Richards. The difference (residual) between the synthetic and measured angle stacks and the synthetic PS angle stacks are shown here separately.

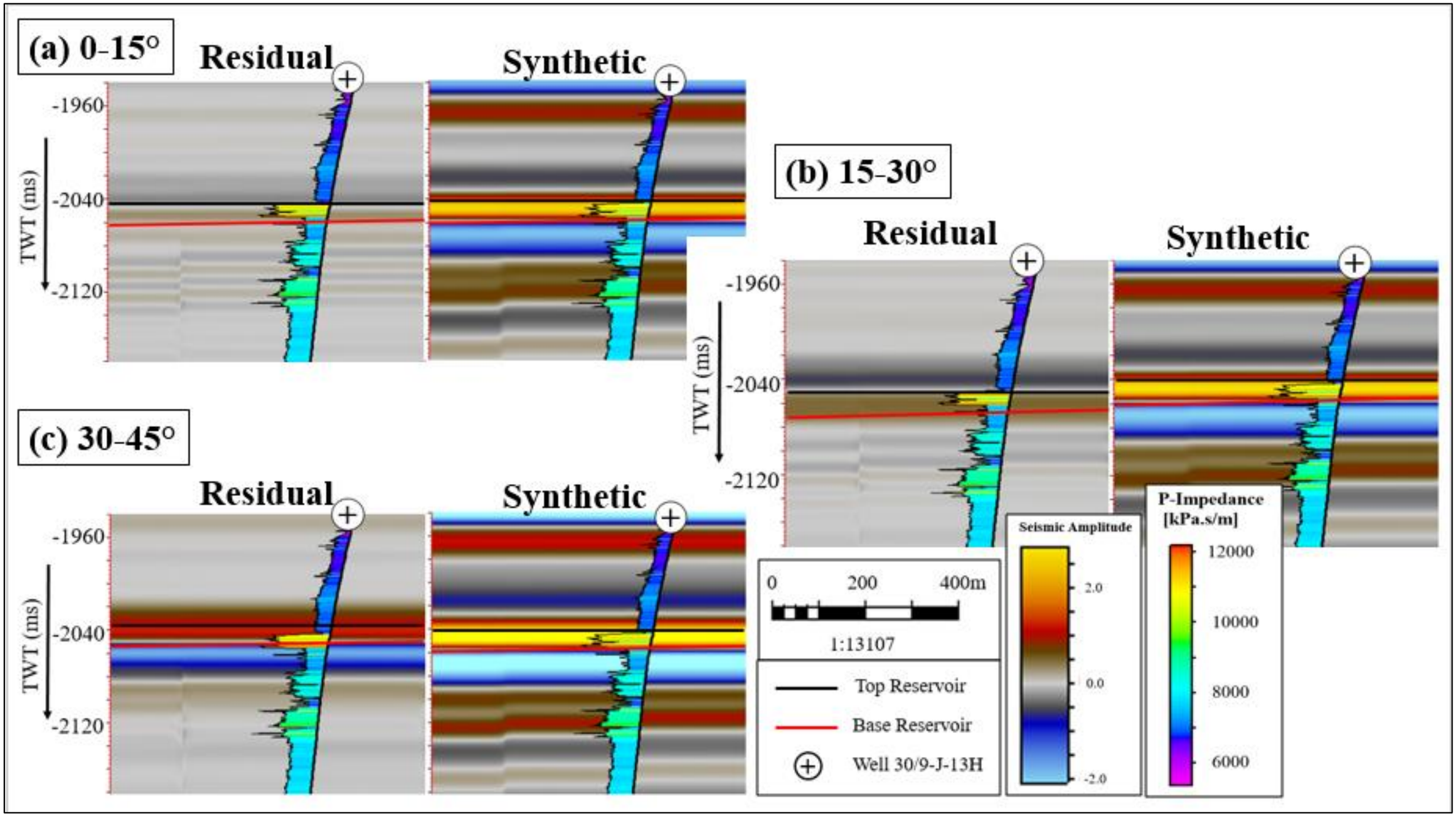

Figure 93: The residual and synthetic PP angle stacks, based on the result from joint PP & PS inversion for sets of three angle stacks by using the algorithm of Aki & Richards.

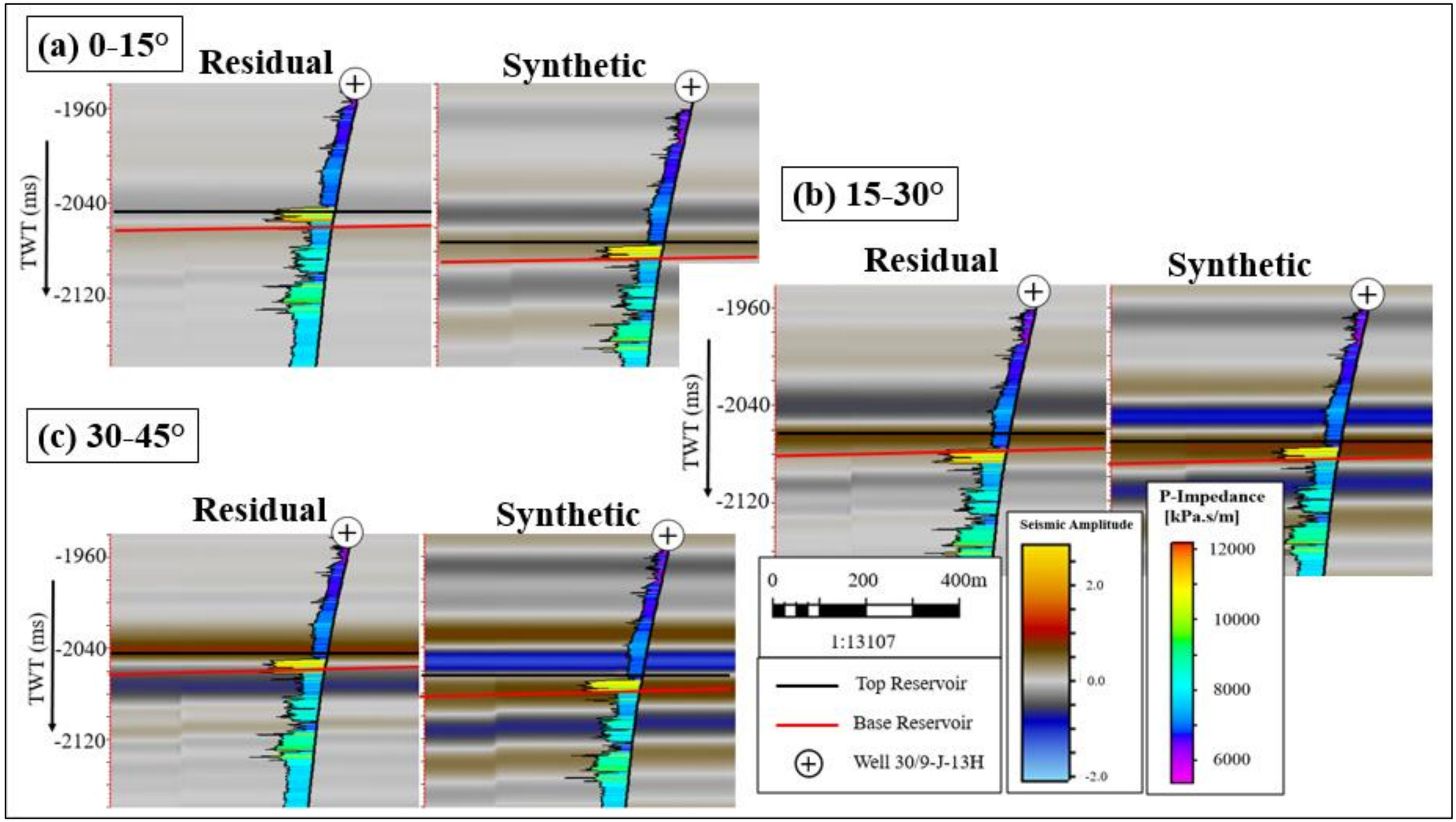

Figure 94: The residual and synthetic PS angle stacks, based on the result from joint PP & PS inversion for sets of three angle stacks by using the algorithm of Aki & Richards.

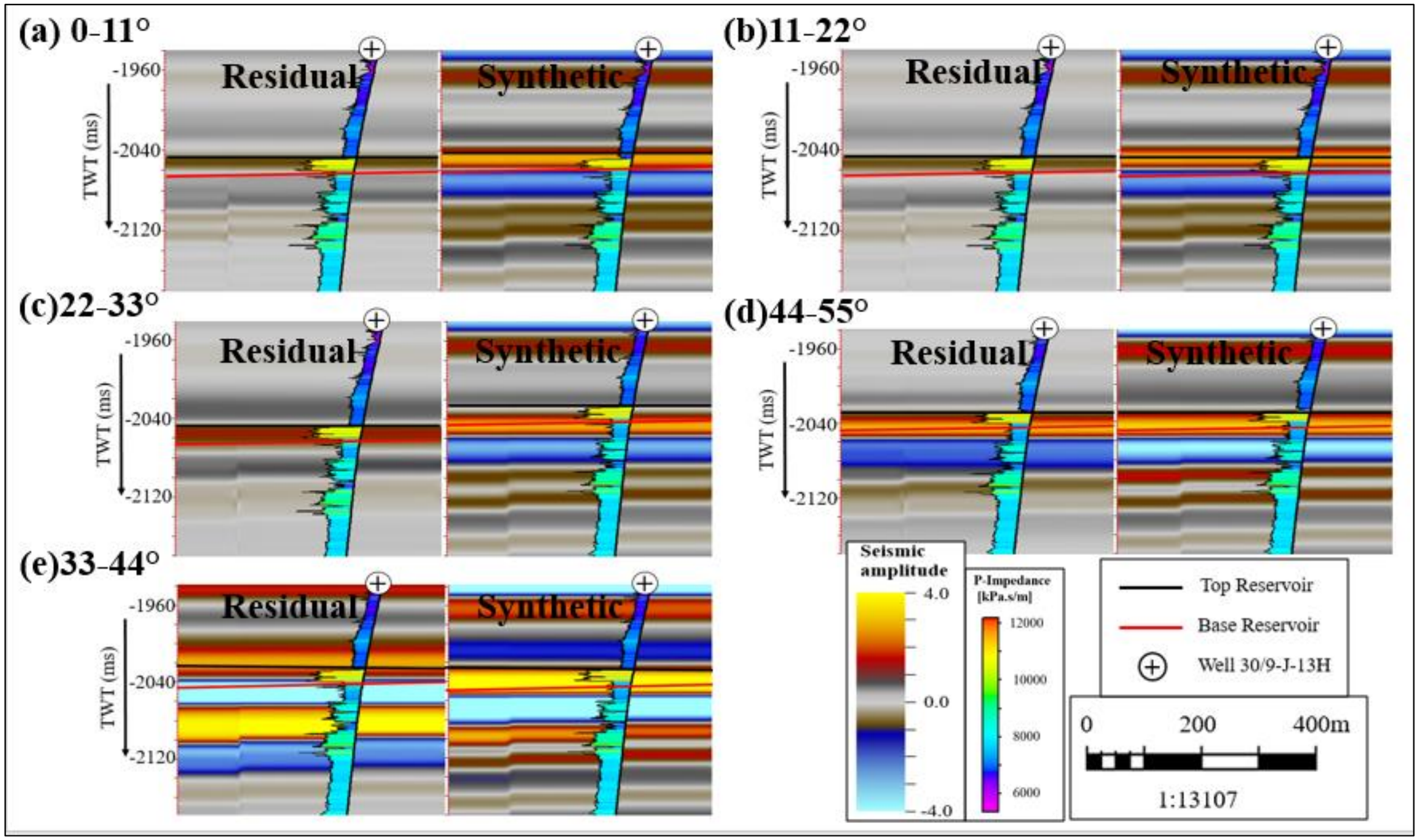

Figure 95: The residual and synthetic PP angle stacks, based on the result from joint PP & PS inversion for sets of five angle stacks by using the algorithm of Aki & Richards.

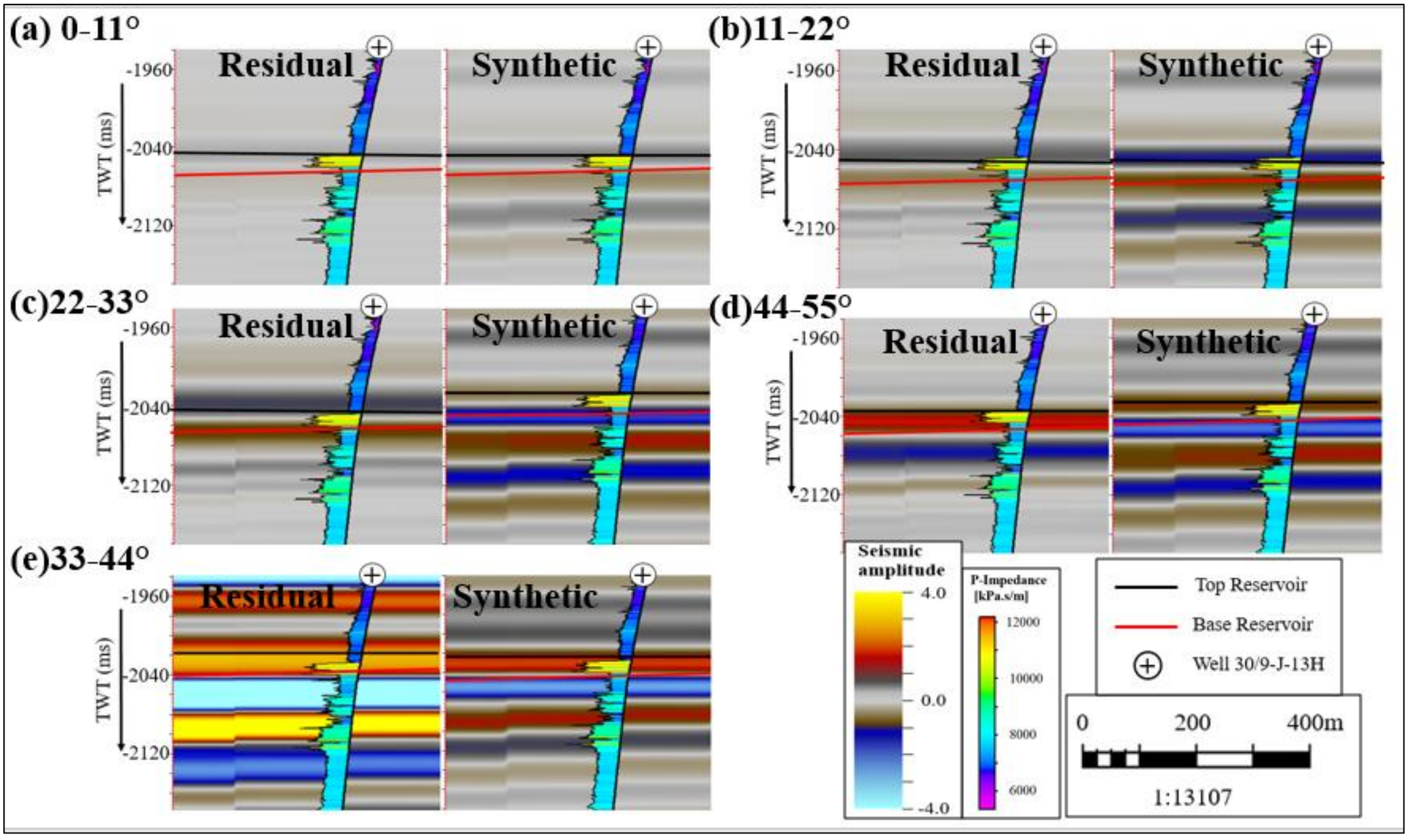

Figure 96: The residual and synthetic PS angle stacks, based on the result from joint PP & PS inversion for sets of five angle stacks by using the algorithm of Aki & Richards.

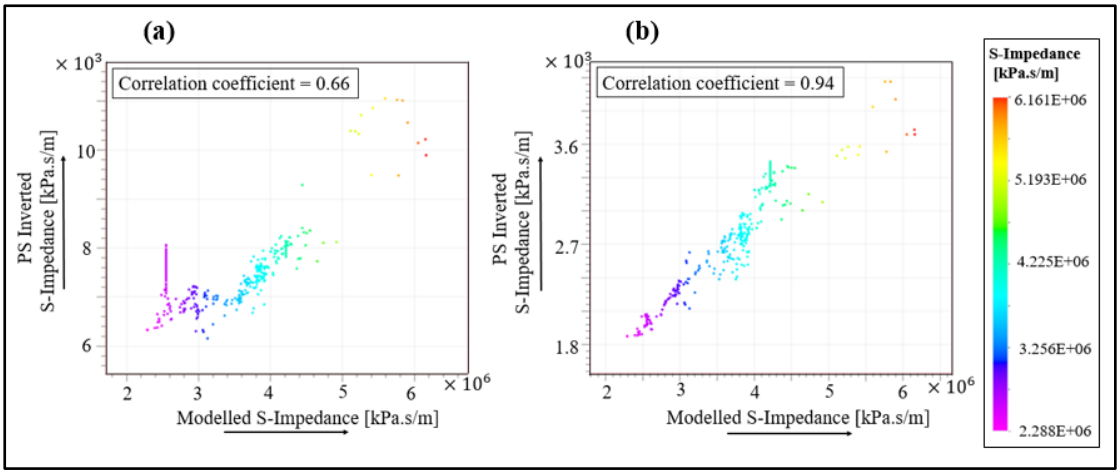

Figure 97: QC Cross plots AVO PP & PS inversion results. (a) Cross plot between modelled and joint inverted S-impedance for three angle stacks of set shows a correlation coefficient of 0.66. (b) Is a cross plot for the same parameters for five angle stacks set. This shows a correlation coefficient of 0.94. This indicates joint PP & PS inversion is delivering a more reliable S-impedance result.

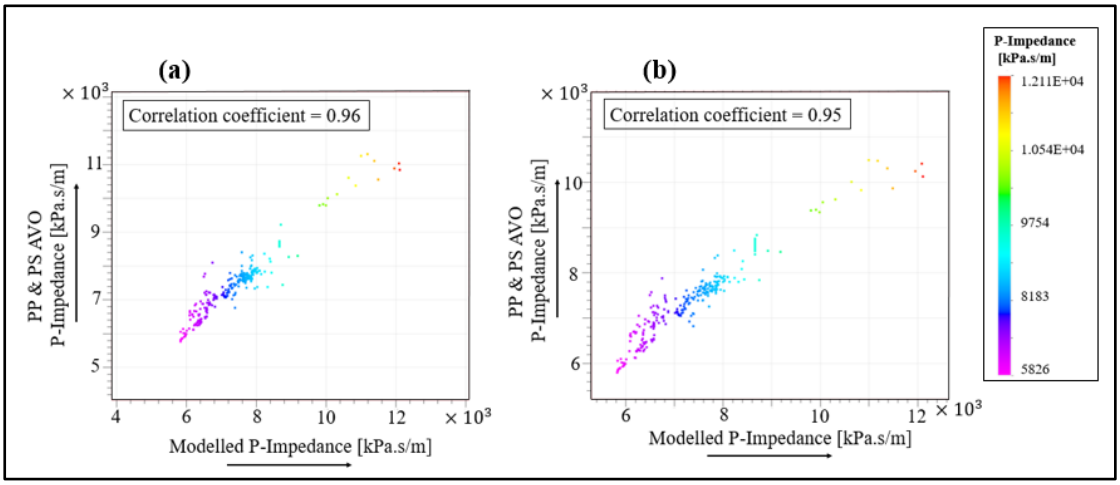

Figure 98: QC Cross plots AVO PP & PS inversion results. (a) Cross plot between modelled and joint inverted P-impedance for three angle stacks of set shows a correlation coefficient of 0.96. (b) Is a cross plot for the same parameters for five angle stacks set. This shows a correlation coefficient of 0.95. There is no large difference between both angle stacks results.

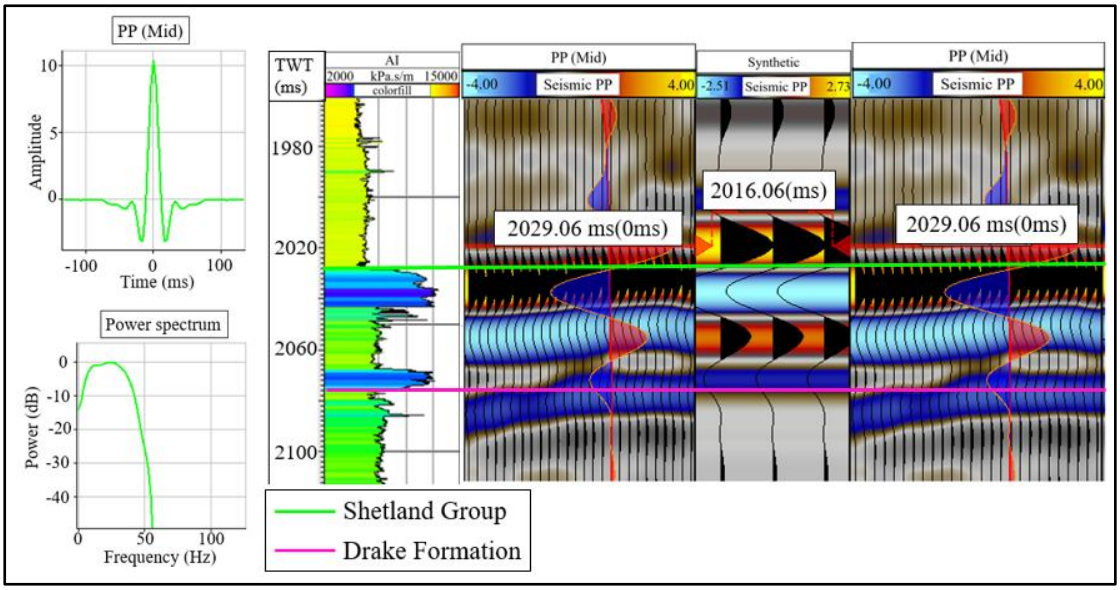

Figure 99: Well tie for the PP (mid) seismic section for the well 30/9-5S. On the left side, the PP ISIS wavelet and power spectrum are shown. Next to it, the acoustic impedance log is shown. The seismic data is clearly not matching the well.

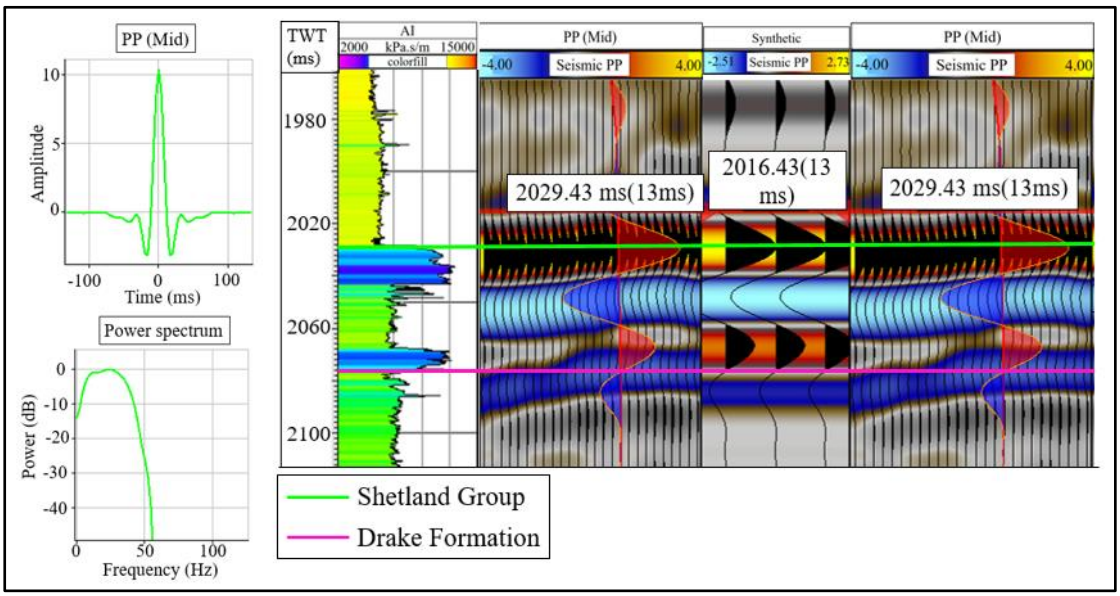

Figure 100: Well tie section of the PP (mid) with well 30/9-5S after applying the bulk shift of 13 ms. On the left side, the PP ISIS wavelet and power spectrum are shown. Next to it, the acoustic impedance log is shown. The well data is matching to seismic section after applying the bulk shift.

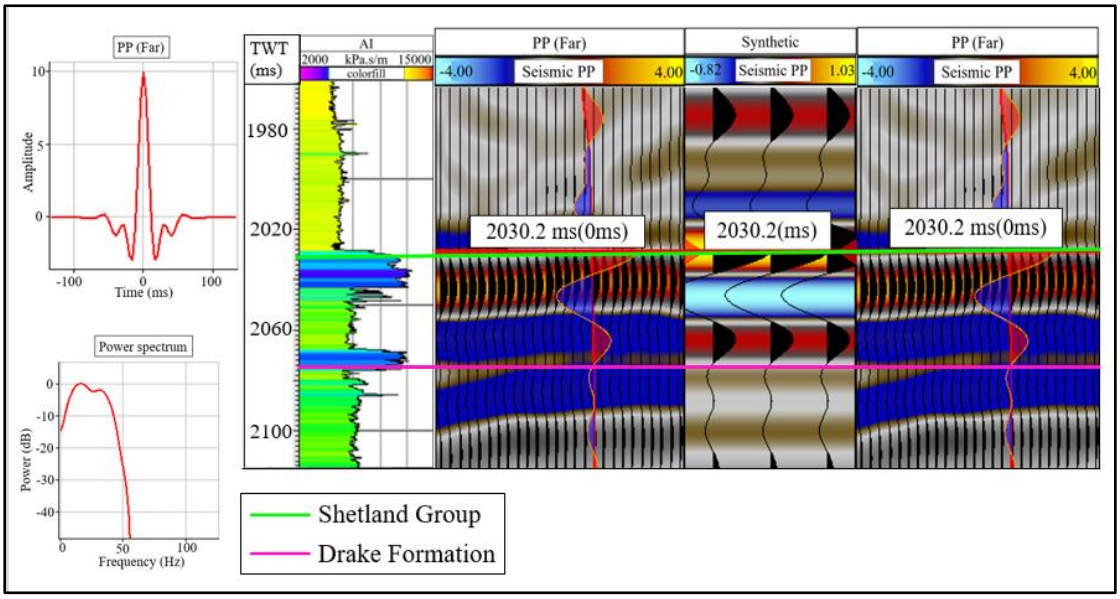

Figure 101: Well tie for the PP (Near) seismic section for the well 30/9-5S. On the left side, the PP ISIS wavelet and power spectrum are shown. Next to it, the acoustic impedance log is shown. The seismic data is clearly not matching the well.

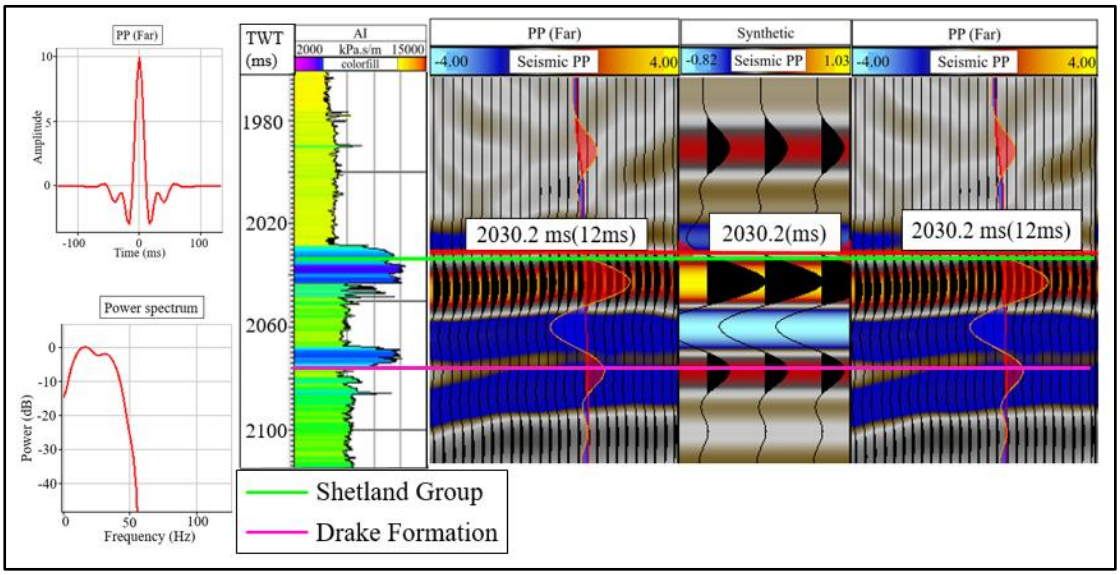

Figure 102: Well tie section of the PP (far) with well 30/9-5S after applying the bulk shift of 12 ms. On the left side, the PP ISIS wavelet and power spectrum are shown. Next to it, the acoustic impedance log is shown. The well data is matching to seismic section after applying the bulk shift 13 ms.

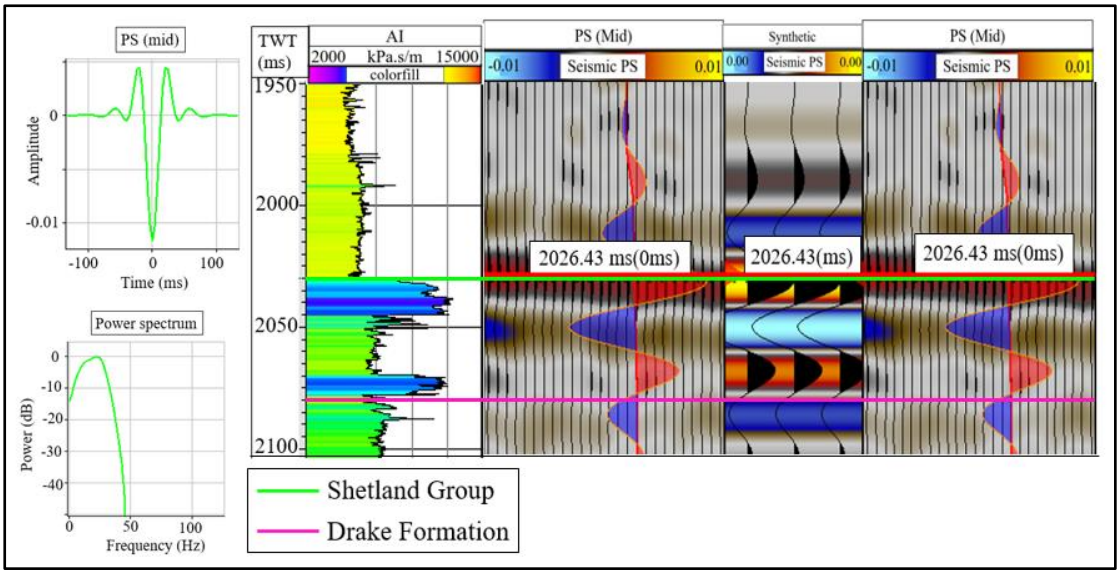

Figure 103: Well tie for the PS seismic section (mid) with well 30/9-5S. On the left side, the PS ISIS wavelet and power spectrum are shown. Next to it, the acoustic impedance log is shown. The seismic section is already fairly matching with the well data.

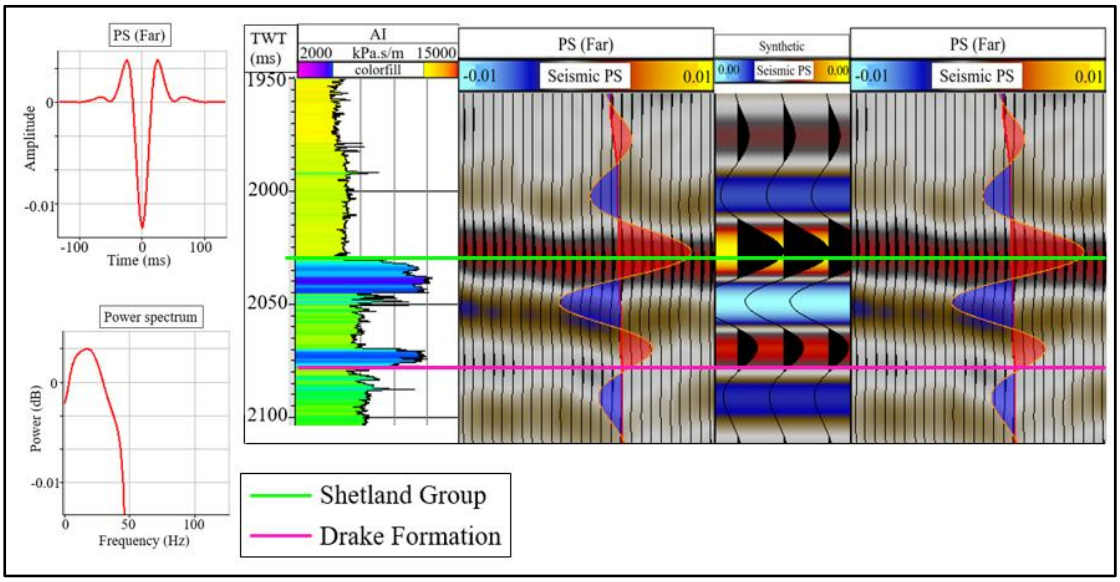

Figure 104: Well tie for the PS seismic section (far) with well 30/9-5S. On the left side, the PS ISIS wavelet and power spectrum are shown. Next to it, the acoustic impedance log is shown. The seismic section is already fairly matching with the well data.

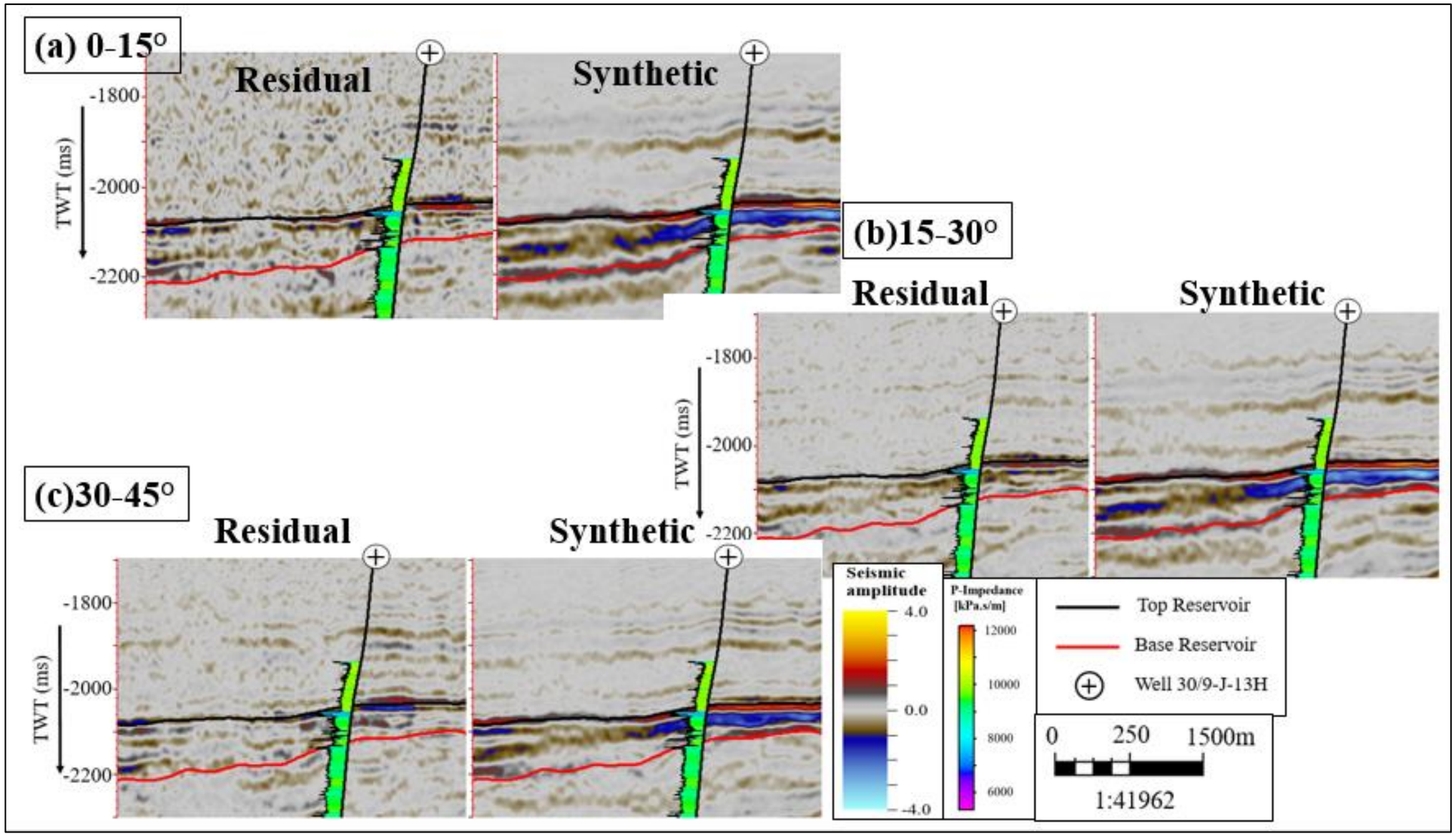

Figure 105: The residual and synthetic PP angle stacks from the Oseberg Field data, based on the result from joint PP & PS inversion by using the algorithm of Aki & Richards.

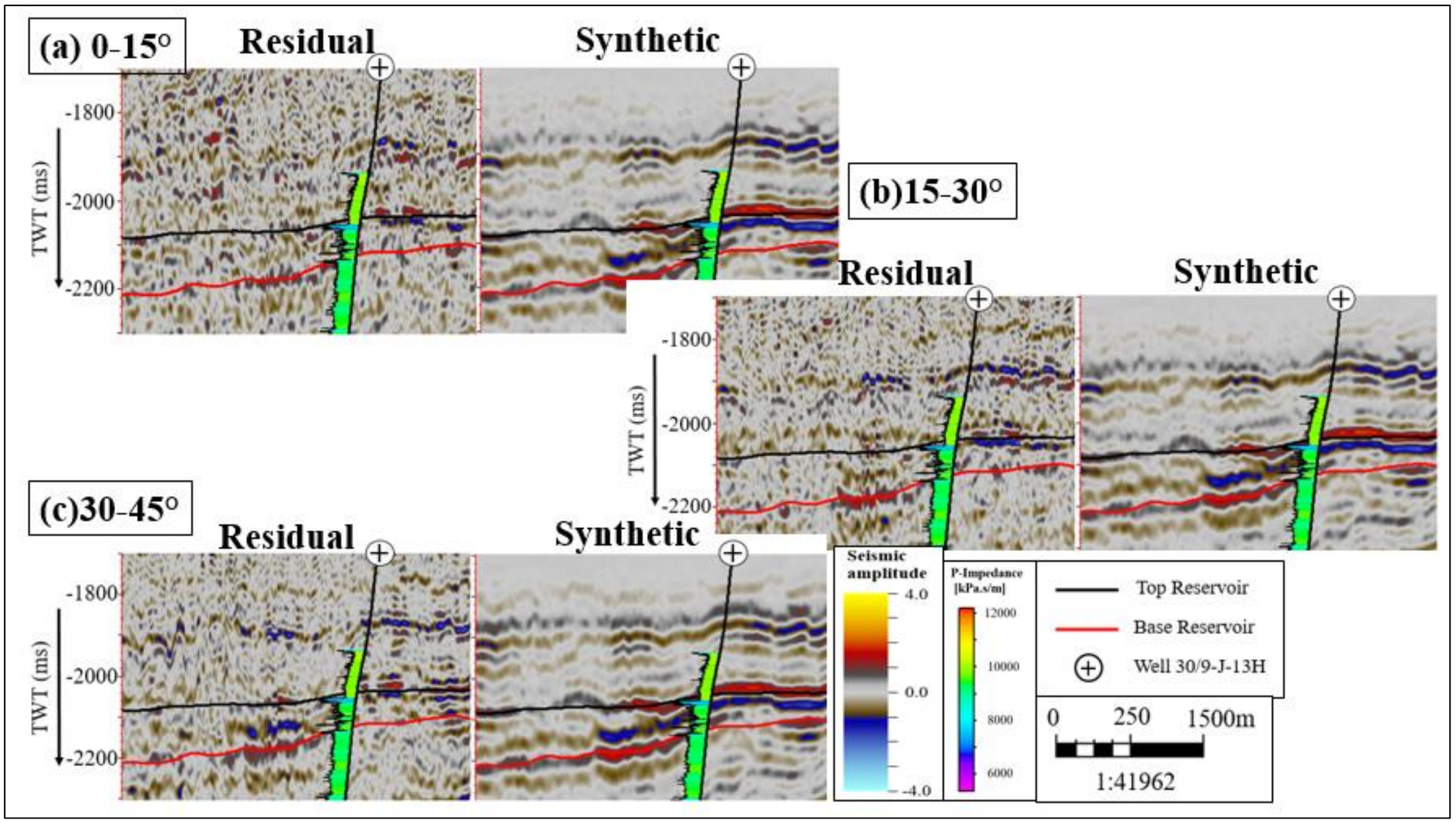

Figure 106: The residual and synthetic PS angle stacks from the Oseberg Field data, based on the result from joint PP & PS inversion by using the algorithm of Aki & Richards

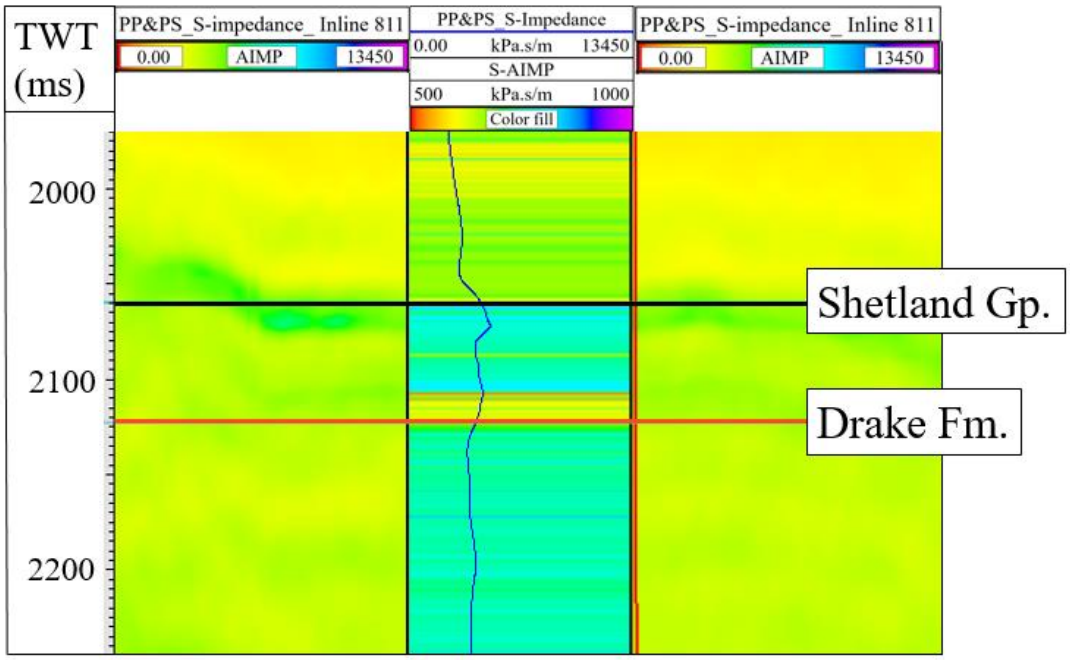

Figure 107: QC of S-impedance results from joint PP & PS inversion of well 30/9-15. The sections are showing the S-impedance based on inversion, while the middle track contains the shear impedance log with the inverted S-impedance.